

UNCLASSIFIED

| |
|---|
| |
| |
| |
| AD NUMBER |
| AD489749 |
| NEW LIMITATION CHANGE |
| TO Approved for public release, distribution unlimited |
| FROM Distribution authorized to U.S. Gov't. agencies and their contractors; Administrative/Operational Use; Aug 1966. Other requests shall be referred to Rome Air Development Center, Attn: EMLI, Griffiss AFB, NY 13440. |
| AUTHORITY |
| RADC/AFSC ltr, 14 Oct 1971 |

THIS PAGE IS UNCLASSIFIED

AD489749

NOTES NOT FIXED ARE BLANK

IMPROVED SAMPLING TECHNIQUES

William G. Tank
William T. Kreiss
James J. Rowley
Thomas Y. Palmer

The Boeing Company

This document is subject to special
export controls and each transmittal
to foreign governments or foreign
nationals may be made only with
prior approval of RADC (ENLI),
GAFB, N.Y. 13440.


FOREWORD


This final report was prepared by William G. Tank, William T. Kreiss, James J. Rowley, and Thomas Y. Palmer of Boeing Company, Seattle, Washington, under Contract AF30(602)-3715, project no. 5579, task no. 557902. RADC project engineer was Donald S. Luczak (EMASA).

This report is not releasable to the general public because it is identifiable with items on the strategic embargo lists that are excluded from export or re-export under U.S. Export Control Acts as implemented by AFR 400-10.

This report has been reviewed and is approved.

Approved: 
DONALD S. LUCZAK
Contract Engineer

Approved: 
THOMAS S. BOND, JR.
Colonel, USAF
Ch, Surveillance and
Control Division

FOR THE COMMANDER: 
IRVING J. GABELMAN
Chief, Advanced Studies Group

ABSTRACT

Line-integrated refractivity is isolated as the basic atmospheric parameter to be determined for corrections to radar ranging data. A basis for the determination of integrated refractivity from measurements of the absorption of infrared and of microwave radiation by atmospheric oxygen and water vapor is then established. Three absorption-measuring systems are next described, and engineering-model design specifications are presented. Each of the specifications offers particular advantages to particular ranging operations. It is estimated that incorporation of such devices into ranging systems will permit real-time measurements of slant range and elevation angle to accuracies five to ten times those currently achieved.

CONTENTS

| | <u>Page</u> |
|--|-------------|
| FOREWORD | ii |
| ABSTRACT | iii |
| SYMBOLS | xiii |
| INTRODUCTION | xviii |
| SECTION I — MEASUREMENT PRINCIPLES | 1 |
| 1. Background | 1 |
| 2. Atmospheric Contributions to Range Parameters | 4 |
| A. Target position | 4 |
| B. Target velocity | 12 |
| C. Summary | 18 |
| 3. \bar{N} -Measurement Technique Survey | 19 |
| A. Background | 19 |
| B. Point-measurement technique | 20 |
| C. Normal dispersion technique | 24 |
| D. Anomalous dispersion technique | 25 |
| E. Summary | 27 |
| 4. Radiation Absorption and the Parameters of Line-Integrated Refractivity | 27 |
| A. Equation of radiative transfer | 28 |
| B. Specification of the absorption coefficient | 29 |
| C. Specification of line-integrated refractivity | 33 |
| D. Summary | 36 |
| 5. Active and Passive Radiometric Systems | 37 |
| A. Active \bar{N} -measurement system | 38 |
| B. Passive \bar{N} -measurement system | 51 |
| C. Summary | 75 |
| 6. Error Analysis | 76 |
| A. Basic \bar{N} -error equation | 76 |
| B. Variance in \bar{N} established by equation uncertainties | 77 |
| C. Variance in \bar{N} established by radiometric measurement errors | 79 |
| D. Residual errors in slant range and elevation angle | 101 |
| E. Summary | 113 |
| SECTION II — INSTRUMENTATION | 116 |
| 1. Background | 116 |
| 2. Infrared Active System | 116 |
| A. Boeing system | 116 |
| B. Range operations system | 121 |
| C. Expected performance | 121 |

CONTENTS (Cont)

| | <u>Page</u> |
|--|-------------|
| 3. Microwave Active Systems | 122 |
| A. Dual-frequency beacons | 123 |
| B. Dual-frequency receivers | 125 |
| C. Expected performance | 125 |
| 4. Passive Systems | 127 |
| A. Oxygen system | 127 |
| B. Water-vapor system | 133 |
| C. Additional comments | 133 |
| D. Expected performance | 133 |
| 5. Summary | 135 |
| SECTION III -- CONCLUSIONS AND RECOMMENDATIONS | 136 |
| 1. Conclusions | 136 |
| A. Range-data correction | 136 |
| B. Solution | 136 |
| C. Expected results | 137 |
| D. Instrumentation | 138 |
| 2. Recommendations | 138 |
| A. Engineering-model calibration | 138 |
| B. Engineering-model evaluation | 142 |
| REFERENCES | 143 |
| APPENDIX I -- A LONG-PATH ABSORPTION REFRACTOMETER | 148 |

ILLUSTRATIONS

| <u>Figure</u> | | <u>Page</u> |
|---------------|---|-------------|
| 1 | Ray Refraction and Retardation Effects on Range Parameters | 3 |
| 2 | Slant Range (S) and Geometric Range (R) | 5 |
| 3 | Interferometer Tracking Geometry | 8 |
| 4 | Two-Station Tracking Geometry | 11 |
| 5 | Definition of Target Velocity Components | 13 |
| 6 | Doppler Velocity Component in Relation to the Radial and Angular Components | 16 |
| 7 | The Near-Infrared Solar Absorption Spectrum | 42 |
| 8 | Theoretical Values of Atmospheric Attenuation by Oxygen and Uncondensed Water Vapor at Sea Level for a Temperature of 20°C. The Solid Curve Gives the Attenuation by Water in an Atmosphere Containing 1 Percent Water Molecules ($p = 7.5 \text{ g/m}^3$). The Dashed Curve is the Attenuation by Oxygen (Reference 24). | 48 |
| 9 | Brightness Temperature versus Frequency for a Vertical Antenna — After Westwater, 1965 | 53 |
| 10 | Brightness Temperature as a Function of Frequency in the 22-GHz Water-Vapor Band | 54 |
| 11 | RMS Error in Kinetic Temperature in the Layer 0-10 km as Related to RMS Measurement Errors in Brightness Temperature | 59 |
| 12 | Deviation of Calculated Temperature Profile from True Profile for Various Alternating Errors in Brightness Temperature | 61 |
| 13 | Radiative Transfer Model | 65 |
| 14 | Absorption Function versus Mean Temperature | 67 |
| 15 | Absorption Function versus Mean Temperature | 68 |
| 16 | Absorption Function versus Mean Temperature | 69 |
| 17 | Water-Vapor and Oxygen Absorption in a Saturated Atmosphere at Standard Surface Temperature and Pressure | 73 |
| 18 | Water-Vapor and Oxygen Absorption in a Saturated Atmosphere at 300 mb (Standard Temperature) | 74 |
| 19 | The Ratio of Relative Integrated Density to Relative Transmittance Errors as a Function of Transmittance | 80 |

ILLUSTRATIONS (Cont)

| <u>Figure</u> | | <u>Page</u> |
|---------------|--|-------------|
| 20 | The Infrared Continuum Extinction Coefficient as a Function of Wavelength | 89 |
| 21 | Computed Extinction Curves for Cloud and Precipitation as a Function of the Wavelength (After Deirmendjian, 1963) | 91 |
| 22 | Scattering by Refractive Index Inhomogeneities as the Cause of Scintillation in the Idealized Line-of-Sight Problem of a Source Viewed Upward Through a Turbulent Medium | 95 |
| 23 | Air Mass as a Function of Elevation Angle | 105 |
| 24 | The Geometry Relating to Specification of Air Mass as a Function of Target Altitude | 106 |
| 25 | Root-Mean-Square Residual Slant-Range Error Nomogram | 107 |
| 26 | Root-Mean-Square Residual Slant-Range Errors as Functions of Slant-Range and Elevation Angle | 109 |
| 27 | Root-Mean-Square Residual Slant-Range Errors in Parts Per Million as Functions of Slant Range and Elevation Angle | 111 |
| 28 | Residual Elevation Angle Errors as Functions of Slant Range and Elevation Angle When $S_1 = S_2 = S$ | 114 |
| 29 | Simultaneous Recordings of Dry-Bulb Temperature (Left-Hand Trace) and Line-Integrated Oxygen Density (Right-Hand Trace) | 118 |
| 30 | Simultaneous Recordings of Dry-Bulb Temperature (Left-Hand Trace), Line-Integrated Oxygen Density (Right-Hand Trace), and Wind Speed and Direction (Center Traces, Respectively) | 119 |
| 31 | Simultaneous Recordings of Dry-Bulb Temperature (Left-Hand Trace) and Line-Integrated Water Vapor Density (Right-Hand Trace) | 120 |
| 32 | Block Diagram of the 17-GHz or 44-GHz Active-System Beacon | 124 |
| 33 | Block Diagram of the 17-GHz or 44-GHz Active-System Receiver | 126 |
| 34 | Block Diagram of the 53-GHz Profiling Radiometer | 128 |
| 35 | 53-GHz Single-Side Band Operation Technique | 130 |
| 36 | Prototype Postdetection Low-Frequency Amplifier | 131 |
| 37 | Postdetector Amplifier-Gain Bandwidth Response for Maximum Integration Times | 132 |

ILLUSTRATIONS (Cont)

| <u>Figure</u> | | <u>Page</u> |
|---------------|---|-------------|
| 38 | Block Diagram of the 20-GHz Profiling Radiometer | 134 |
| 39 | Comparison of Integrated Oxygen Density and Dry-Bulb Temperature Data | 140 |

TABLES

| <u>Table</u> | <u>Page</u> |
|--|-------------|
| 1. Cloud Particle Sizes and Number Densities | 45 |
| 2. Scattering Coefficients of Clouds | 46 |
| 3. Cloud Thicknesses Required for Transmittances Equal to 0.01 | 46 |
| 4. Resonant Oxygen-Transition Frequencies | 57 |
| 5. Errors in Profile Parameters Versus Polynomial Degree | 59 |
| 6. Values of the Constants, a, b, c, and d, and of the Error Components A_1 , A_2 , A_3 , and w_{O_2} in the \bar{N} rms Error Equation, Through One Standard Air Mass | 78 |
| 7. Contributions of the Error Components to the Total Variance in \bar{N} | 78 |
| 8. Relative Errors in $\bar{\rho}$ and $(\bar{\rho}/T)$ Specifications per Unit Standard Air Mass Ascribable to Atmospheric Effects on Different Radiometric System Configurations | 102 |
| 9. \bar{N} -Specification Errors (per Unit Standard Air Mass) Ascribable to Atmospheric Effects on Different Radiometric System Configurations | 103 |

SYMBOLS

NOTE: Paragraph numbers refer to Section I only.

| | |
|-------------|--|
| A_ν | Absorptance at frequency ν |
| B | Interferometer system baseline length |
| c | Speed of light in the atmosphere |
| c_0 | Speed of light in a vacuum |
| $c(s)$ | Turbulent fluctuation correlation function |
| d | Mean spacing between spectral lines |
| D(n) | Mean deviation of refractive index fluctuations |
| e | Partial pressure of water vapor |
| E | Total molecular energy state |
| E_e | Electronic energy state |
| E_v | Vibrational energy state |
| E_r | Rotational energy state |
| E_t | Translational energy state |
| h | <div style="display: flex; align-items: center;"> <div style="font-size: 2em; margin-right: 5px;">{</div> <div> Plank's constant (Paragraph 4. B. (1)) Altitude (Paragraph 5. B. (2) (B)) </div> </div> |
| I_ν | Radiant intensity at frequency ν |
| I_{ν_0} | Intrinsic source radiant intensity at frequency ν |
| J_ν | Emission source function at frequency ν |
| k | <div style="display: flex; align-items: center;"> <div style="font-size: 2em; margin-right: 5px;">{</div> <div> Boltzmann's constant (Paragraph 4. B. (1)) Turbulent-eddy wavenumber (Paragraph 6. C. (4) (D)) </div> </div> |
| l | <div style="display: flex; align-items: center;"> <div style="font-size: 2em; margin-right: 5px;">{</div> <div> x-direction cosine (Paragraph 2. A. (2)) Linear dimension of turbulent eddies (Paragraph 6. C. (4) (D)) </div> </div> |
| l_0 | Integral scale of turbulence |

| | |
|--------------------------|--|
| L | Atmospheric path through turbulence |
| m | $\left\{ \begin{array}{l} \text{y-direction cosine (Paragraph 2.A. (2))} \\ \text{air mass (Paragraphs 6.C. (4)(A) and (2)(A))} \end{array} \right.$ |
| M_a | Molecular weight of atmospheric specie a |
| n | $\left\{ \begin{array}{l} \text{Refractive index} \\ \text{z-direction cosine (Paragraph 2.a. (2))} \end{array} \right.$ |
| n_a | Number density of atmospheric specie a |
| N | $\left\{ \begin{array}{l} \text{Refractivity} \\ \text{Avogadro's number (Paragraph 4.B. (3))} \end{array} \right.$ |
| N_∞ | Optical refractivity |
| \bar{N} | Line-integrated refractivity |
| p | Total atmospheric pressure |
| p_d | Partial pressure of dry air |
| r | Radius of the Earth |
| R | $\left\{ \begin{array}{l} \text{Geometric range (Paragraph 2.A. (1))} \\ \text{Gas constant for dry air (Paragraph 4.C.)} \end{array} \right.$ |
| R' | Gas constant for water vapor |
| R^* | Universal gas constant |
| α_ν | Volume absorption coefficient at frequency ν |
| β_s | Scattering extinction coefficient |
| γ_ν | Molecular absorption coefficient at frequency ν |
| ϵ | True elevation angle |
| ϵ_a | Apparent elevation angle |
| $\Delta\epsilon$ | Elevation-angle error |
| $\Delta(\Delta\epsilon)$ | Residual elevation-angle error |

| | |
|-------------------------|---|
| η | Turbulence scattering parameter |
| I | Absorption line intensity |
| λ | Radiation wavelength |
| ν | Radiation frequency |
| ν_0 | Resonant frequency |
| $\Delta\nu$ | Absorption line width |
| ρ | Atmospheric density |
| ρ_a | Partial density of atmospheric specie a |
| ρ_{O_2} | Partial density of oxygen |
| ρ_w | Partial density of water vapor |
| $\overline{\rho_{O_2}}$ | Line-integrated oxygen density |
| $\overline{\rho_w}$ | Line-integrated water-vapor density |
| τ_ν | Transmittance at frequency ν |
| R_{ij} | Dipole moment matrix element |
| ΔR_g | Geometric range error |
| S | Slant range |
| S_e | Electrical range |
| S_D | Interferometer slant range difference |
| $S(k)$ | Spectrum of atmospheric turbulence |
| ΔS | Slant-range error |
| $\Delta(\Delta S)$ | Residual slant-range error |
| Δt | Radar delay time |
| T | Temperature |
| T_{B_ν} | Brightness temperature at frequency ν |


| | |
|----------------------|--|
| $\langle T \rangle$ | Mean temperature taken with respect to the logarithm of pressure |
| \vec{v} | Target velocity vector |
| V_S | Target radial velocity component |
| V_ϵ | Target angular velocity component |
| V_r | Target Doppler velocity component |
| ΔV_r | Doppler velocity error |
| x, y, z | Cartesian coordinates |
| τ_{O_2} | Transmittance in an oxygen-absorption band |
| τ_w | Transmittance in a water-vapor absorption band |
| τ_c | Continuum transmittance |
| ϕ | Interferometer angle |
| $\Delta(\Delta\phi)$ | Residual interferometer-angle error |
| ψ | Target azimuth angle |
| ω_{O_2} | Oxygen-mixing ratio |

EVALUATION - CONTRACT AF30(602)-3715

1. To apply corrections for refractive errors encountered by radar systems, an accurate account of the atmosphere is essential. Present day measuring techniques, such as radiosondes and refractometers, provide only the long term vertical refractive structure of the atmosphere; thus a need exists for a real time sampling technique capable of measuring the short term fluctuations of the refractive index along a ray path. These fluctuations can produce large refraction errors, especially at low elevation angles.

2. This contract was awarded to the Boeing Company to study techniques that will provide a real time measurement of the integrated refractivity along a ray path. The conclusions of this study showed that the most accurate technique for measuring the refractivity along a radar path would be a radiation transfer measurement technique (measurement of absorbed radiation intensity) performed in the oxygen and water vapor absorption bands at the near infrared and millimeter frequencies. Also from this study, two basic measurement systems have been envisioned to take into account cooperative and uncooperative targets.

3. Future work will be to develop and implement an instrument package as dictated by the results of this study. The instrumentation will then be used to collect data under different climatic conditions and correlated with the meteorological conditions of the environment for evaluation as a real time refraction correction system.


DONALD S. LUCZAK
Contract Engineer

INTRODUCTION

When using radio waves in long-range target detection and tracking, the limiting factor of system performance and capability is largely dependent on the medium (or atmosphere) through which the waves are propagated. In the atmosphere, the homosphere and the ionosphere are the regions that greatly influence and affect radio-wave propagation. The homosphere is defined as that region of the atmosphere that exhibits substantially uniform composition (i.e., constant mean molecular weight) from the surface of the Earth upwards. It includes both the tropospheric and stratospheric regions of the atmosphere. The ionosphere is defined as the region of the atmosphere characterized by electron densities sufficiently large to affect radio communication. This report is concerned only with effects on radar system performance ascribable to the molecular composition of the atmosphere, and thus relates only to the homospheric effects. Ionospheric effects are left to future study.

Section I

MEASUREMENT PRINCIPLES

1. BACKGROUND

In a nonrefractive environment, single-station radar ranging and tracking data admit to very simple interpretations. Target slant range is determined simply as the product of the speed of light, in vacuo, by the target-to-receiver ray transit or delay time. Target bearing is determined by the angle of arrival of the incoming ranging rays.

Even in a refractive medium, such as the atmosphere, the above concepts are used to provide first-order approximations to target range and bearing. However, two effects cause errors in both the above mentioned range parameters. First, the presence of the material medium results in a slowing down or retardation of the ranging rays; i.e., the ranging signals travel at speeds somewhat less than the speed of light in vacuo. The product $c_0 \Delta t$ (where c_0 is the vacuum velocity of light, and Δt is the measured delay time) results in an overestimate of slant range. Second, because refractive index decreases with altitude in the atmosphere, a ray bending associated with the refractive index gradient occurs, with the result that the ray angles of arrival are not those of the straight-ray path. The result is that the target is "seen" in the wrong direction; viz., in the direction of the tangent (at the radar receiver) to the refracted ray. The effects of both ray retardation and ray bending or refraction on the radar measurement of range parameters are illustrated in Figure 1. In the figure, S_0 — the electrical range — is the first-order slant-range estimate given by the previously defined product $c_0 \cdot \Delta t$. The true slant range, S , is closely approximated* by the product $c \cdot \Delta t$, where c denotes the actual ray propagation speed in the medium. The slant-range error, ΔS , is

* The approximation neglects the purely geometric effect on Δt attributable to the finite differences in curved versus straight-ray path lengths. For elevation angles $\epsilon > 5^\circ$, such effects are negligible.

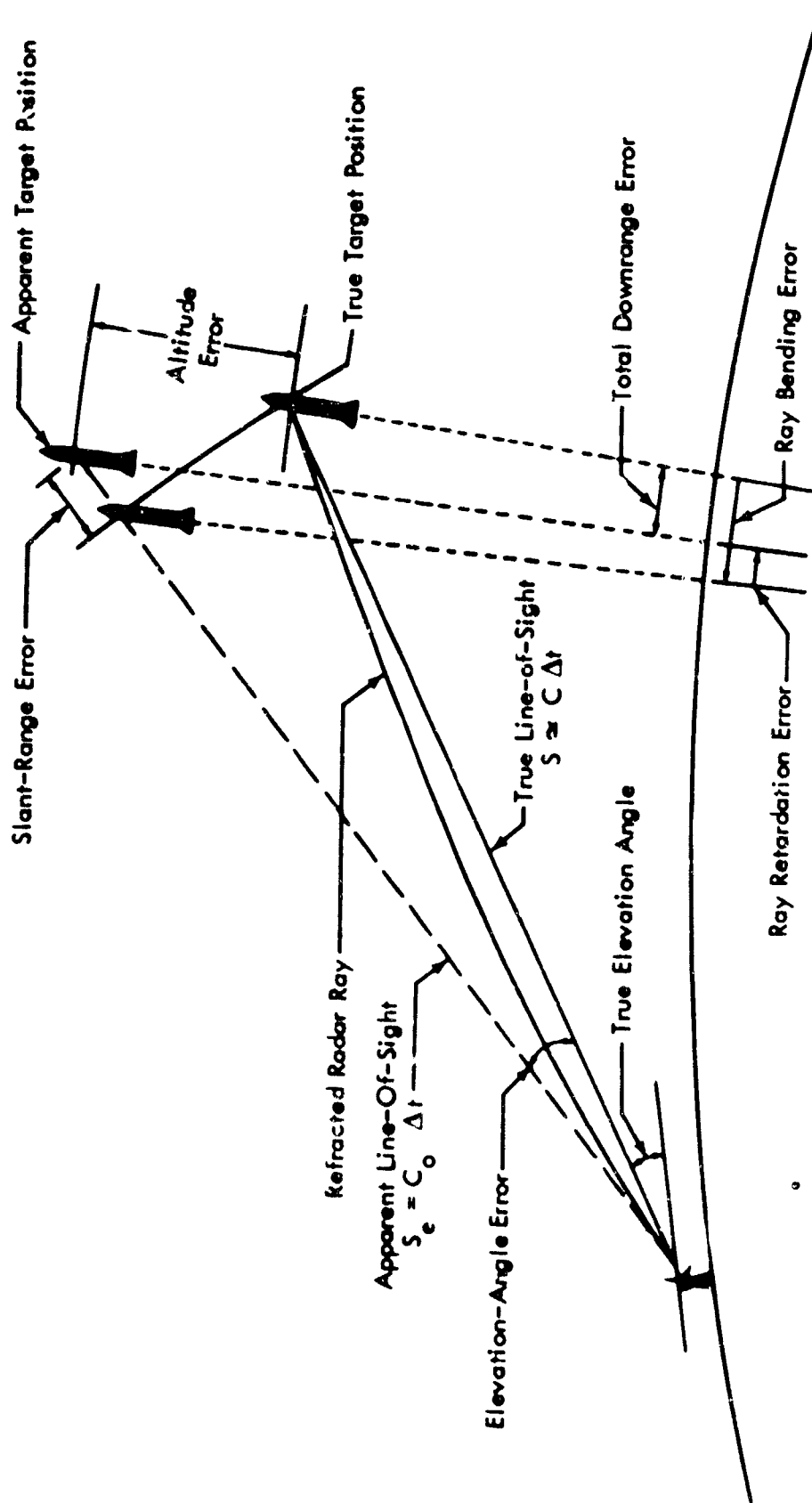


Figure 1: RAY REFRACTION AND RETARDATION EFFECTS ON RANGE PARAMETERS

thus definable as the difference between the electrical and true slant ranges; the elevation angle error, $\Delta\epsilon$ is definable as the difference between the straight-ray direction, ϵ , and that of the apparent ray, ϵ_a . That is,

$$\Delta S = S_e - S, \quad (1)$$

$$\Delta\epsilon = \epsilon_a - \epsilon. \quad (2)$$

Methods of estimating the magnitudes of the error increments defined by Equations 1 and 2 are needed. Historically, the refractive bending problem has received the greatest amount of attention for the longest period of time. Past work by various researchers (for example, those cited in References 1, 2, 3, and 4) has shown that it is possible to estimate the atmospheric refraction of radio waves to a respectable precision. The technique is to apply Snell's law of refraction to effect a ray tracing through an atmosphere assumed homogeneous in spherical shells surrounding the Earth, and in which refractive index decreases more or less monotonically (and very nearly exponentially) with height. Only since the advent of increasingly sophisticated techniques for measuring delay times to higher degrees of precision have ray-retardation effects assumed proportions significant enough to warrant a similar amount of attention. Concurrently with the increased precision of time-delay data, however, has come a need for matching increases in specifying bearing-angle data to higher degrees of accuracy. The point has been reached in this latter demand where, even disregarding for the moment refractive bending elevation errors, troublesome errors in the measure of elevation angles arise simply because of feed-horn droop or dish distortion in radars such as the AN/FPQ-6 pulse systems (Reference 5). These purely mechanical problems are compounded in the tracking operation when target velocity determinations must depend on mechanical changes in antenna azimuth and elevation. The result of this enigma has been the evolution of ranging techniques wherein the direct measure of target bearing angle is eliminated, which is accomplished by trilateration solutions that permit the expression of bearing angle in terms of range and range difference data obtained

from two or more stations. The trilateration mode of operation with pulse radar systems is epitomized at the Atlantic Missile Range by the GLOTRAC pulse-system tracking network (Reference 5). Equivalent results are obtained more directly and more simply with c-w interferometer systems such as AZUSA and MISTRAM (Reference 5), where target range is measured at a "mother" station by comparing the phase of the signal received from a beacon transponder with an internal phase reference. Range differences are obtained directly by comparing phases of received signals at the mother and at "slave" stations. These range differences define receiver-to-target direction cosines. These data, in conjunction with range data, are sufficient to determine target position.

The point to be emphasized is the elimination of the direct measure of target bearing angles in precision ranging operations, and the consequent emergence of the ray-retardation effect as the prime atmospheric source of error in range data. That is, improved techniques for estimating the retardation effect will serve not only to increase the accuracy of slant-range measurement but will also result in the acquisition of improved bearing-angle data as well.

2. ATMOSPHERIC CONTRIBUTIONS TO RANGE PARAMETERS

A. Target position

(1) Slant range

From the mathematical statement of Fermat's principle of least time, the time taken by a radio ray in traveling from a target at a point, P, of its trajectory, T, along the refracted path, R, to an observation point, O (Figure 2), is given by (Reference 6):

$$\Delta t = \int_0^P \frac{d\sigma}{c}, \quad (3)$$

where $d\sigma$ is an element of the curved path, and c is the speed of propagation in the medium. Introducing the refractive index,

$$n = \frac{c_0}{c}, \quad (4)$$

Equation 3 is written

$$c_0 \Delta t = \int_0^P n(x, y, z) d\sigma. \quad (5)$$

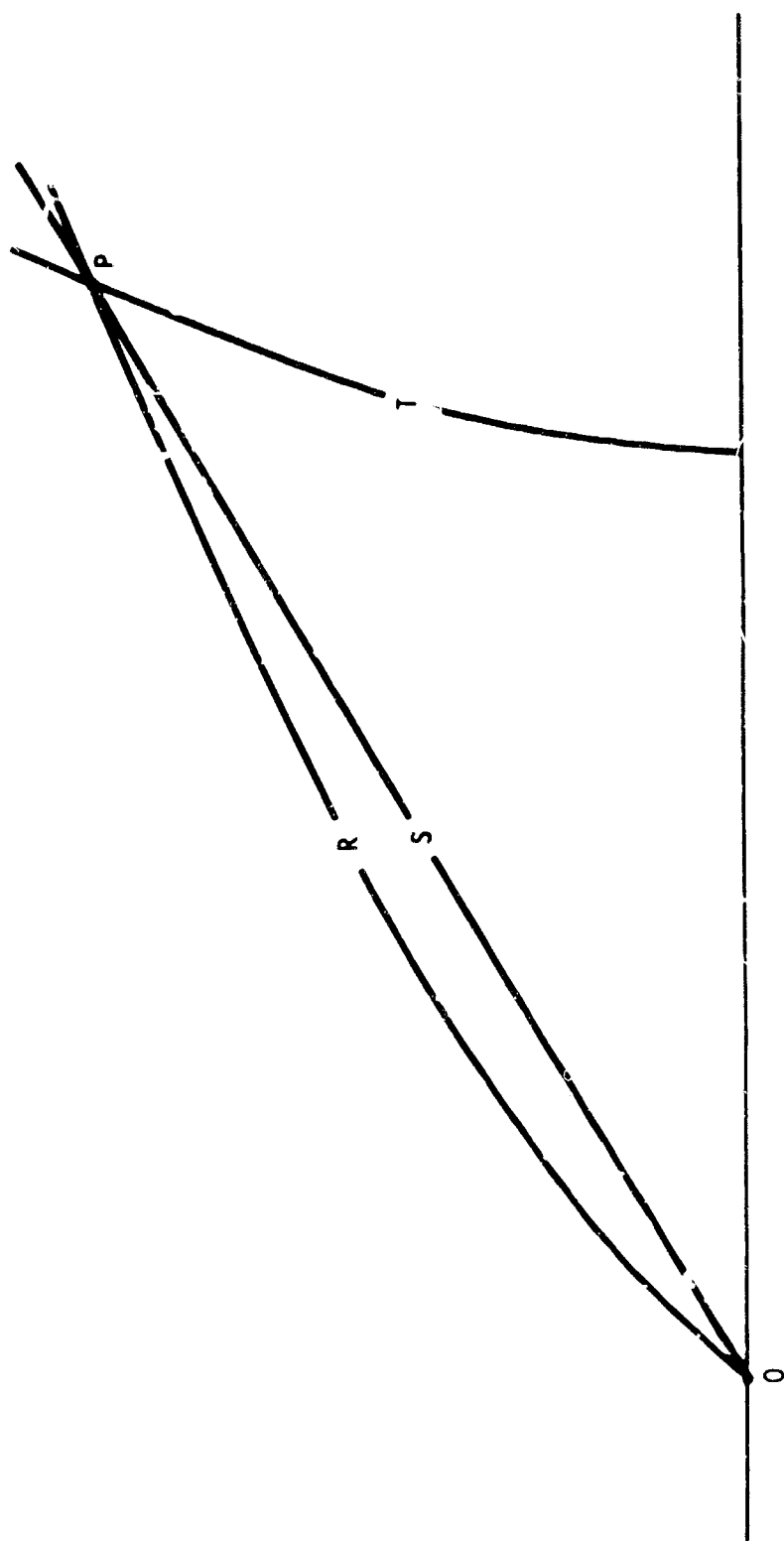


Figure 2: SLANT RANGE (S) AND GEOMETRIC RANGE (R)

Refractivity, defined as the excess of refractive index over unity in parts per million, is given by

$$N = (n - 1) 10^6 \quad (6)$$

Therefore,

$$c_0 \Delta t = \int_0^P ds + 10^{-6} \int_0^P N(x, y, z) d\sigma. \quad (7)$$

Equation 7 expresses the electrical range ($c_0 \Delta t$ as previously defined) as the sum of two terms. The first term on the right-hand side of Equation 7 is simply the length of the refracted ray path, or geometric range, R ; the second term is the contribution to S_e ascribable to an atmospheric propagation speed not equal to that in vacuo. The last term describes the retardation of the ranging signal in its passage through the material medium. By the definition contained in Equation 1, the slant-range error is determined by

$$\Delta S = 10^{-6} \int_0^P N(x, y, z) d\sigma + \int_0^P ds - S. \quad (8)$$

Bean and Thayer (Reference 3) define the difference between the last two terms on the right-hand side of Equation 8 as the "geometric range error," ΔR_g , and show that it does not represent a significant portion of the total range error except at very small target elevation angles (between zero and about 3 degrees). Even then the effect is so small (ΔR_g is about 6 percent of ΔS when $\epsilon \approx 1$ degree) that the simplest of ray curvature correction techniques -- for example, curvature estimates based simply on surface refractivity values (Reference 3) suffice to reduce it to negligible proportions. By virtue of these two facts, the difference ($R-S$) may be reasonably considered to be zero, and the integration along the curved path replaced by integration over the direct path. Under these conditions, Equation 8 reduces to the following expression for the atmospheric contribution of slant-range error:

$$\Delta S \approx 10^{-6} \int_0^P N(s) ds. \quad (9)$$

Therefore, from Equation 1,

$$S = S_e - 10^{-6} \int_0^P N(s) ds. \quad (10)$$

The above expression indicates that to determine the slant range between target and observation point, it is necessary to measure the ray transit time, then multiply this by the vacuum speed of light, and diminish the result by a quantity that represents the integrated effect of the slowing of the ray by the intervening material atmosphere.

(2) Elevation angle — interferometric measurement

Target elevation in radar interferometry is determined as shown in Figure 3. From the law of cosines,

$$\cos \phi_1 = \frac{1}{B_1} \left[S_{D_1} + \frac{B_1^2 - S_{D_1}^2}{2 S_0} \right], \quad (11)$$

where $S_{D_1} = S_0 - S_1$, and

$$\cos \phi_2 = \frac{1}{B_2} \left[S_{D_2} + \frac{B_2^2 - S_{D_2}^2}{2 S_0} \right], \quad (12)$$

where $S_{D_2} = S_0 - S_2$.

In the above expressions, S_0 is the measurement performed by the mother station at Point 0 through internal phase reference, and the range differences $S_{D_1} = (S_0 - S_1)$ and $S_{D_2} = (S_0 - S_2)$ are measured by the comparison of the phases of the signals received at the mother and at the slave stations located at Points 1 and 2.

A further relationship to be noted from the geometry of Figure 3 is that the projections of S_0 onto the baselines B_1 and B_2 are

$$S_{B_1} = S_0 \cos \phi_1, \quad (13)$$

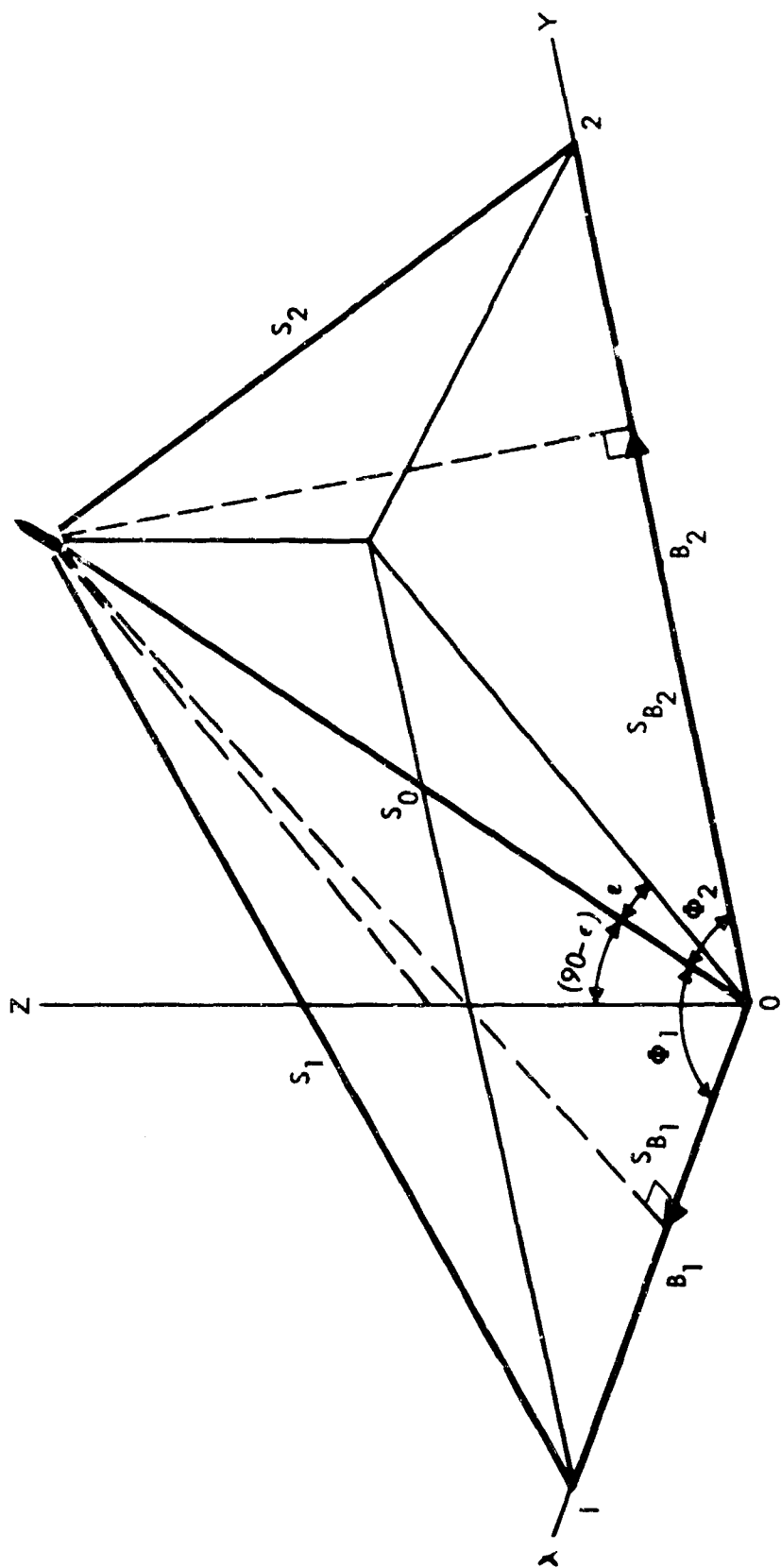


Figure 3: INTERFEROMETER TRACKING GEOMETRY

and

$$S_{B_2} = S_0 \cos \phi_2, \quad (14)$$

respectively. If, without loss of generality, B_1 and B_2 are considered orthogonal and as defining the x-y axes, respectively, of the Cartesian coordinate system, then the cosine functions define simply the x and y direction cosines of the slant range, S_0 ; that is,

$$\cos \phi_1 = \frac{S_{B_1}}{S_0} \equiv l \quad a) \quad (15)$$

$$\cos \phi_2 = \frac{S_{B_2}}{S_0} \equiv m \quad b)$$

Recognizing that the sum of the squares of the three-dimensional direction cosines is equal to unity;

$$l^2 + m^2 + n^2 = 1,$$

then, from Equation 15,

$$n^2 = 1 - (\cos^2 \phi_1 + \cos^2 \phi_2), \quad (16)$$

where n now defines the direction cosine to the z-axis (the target zenith angle),

$$n^2 = \cos^2(\epsilon) = \sin^2 \epsilon = 1 - (\cos^2 \phi_1 + \cos^2 \phi_2). \quad (17)$$

Therefore,

$$\epsilon = \arcsin \left[1 - (\cos^2 \phi_1 + \cos^2 \phi_2) \right]^{1/2} \quad (18)$$

Equation 18 thus defines target elevation angle in terms of the measured interferometer angles ϕ_1 and ϕ_2 . The slant ranges that determine ϕ_1 and ϕ_2 (Equations 11 and 12) are as given by Equation 10. Line-integrated refractivity emerges again as the basic atmospheric parameter to be acquired to effect corrections to elevation-angle measurements. Also, consider that the range differences $(S_0 - S_1)$ and $(S_0 - S_2)$ may be written, in line with Equations 9 and 10, as

$$S_0 - S_1 = (S_e - \Delta S_0) - (S_e - \Delta S_1)$$

$$\text{or } S_{D_1} = S_{eD_1} - (\Delta S_0 - \Delta S_1) \quad (19)$$

$$\text{and } S_0 - S_2 = (S_{0e} - \Delta S_0) - (S_{2e} - \Delta S_2)$$

$$\text{or } S_{D_2} = S_{eD_2} - (\Delta S_0 - \Delta S_2) \quad (20)$$

That is, the desired range differences are determined by the differences in electrical ranges, diminished by the differences in the atmospheric slant range contributions. The need for line-integrated refractivity measurement at each of the interferometer stations is immediately apparent.

(3) Elevation angle — trilateration

A three-station trilateration mode of operation to determine target elevation is simply a special case of the interferometric operational mode. That is, referring again to Figure 3, the parameter requirements — the slant range S_0 and range differences $(S_0 - S_1)$ and $(S_0 - S_2)$ — are the same, and the data is interpreted according to the dictates of Equation 18. This will vary only in that range difference is no longer measured directly through mother-to-slave base comparisons, but is obtained by separately measuring slant range from each of the three stations; again, therefore, there is the requirement for line-integrated refractivity to be measured at all three ranging stations.

Similarly, target elevation can be precisely measured from just two ranging stations (Figure 4). Such an approach requires measuring the target azimuth angle, ψ_0 and ψ_1 , from each of the two stations. But because the atmosphere exhibits more homogeneity in the horizontal than in the vertical, the precision of measurement of azimuth as compared to elevation angles is correspondingly greater. The work of Martin and Wright (Reference 7) shows that (1) the ratio of horizontal to vertical ray bending is on the order of 10^{-4} , and (2) even for very low elevation angles ($\epsilon < 1^\circ$) a ray cannot be bent significantly out of its initial vertical plane even though the ray azimuth differs from any horizontal refractivity gradient. Accordingly, the law of cosines applied to the geometry of Figure 4 permits the statement that

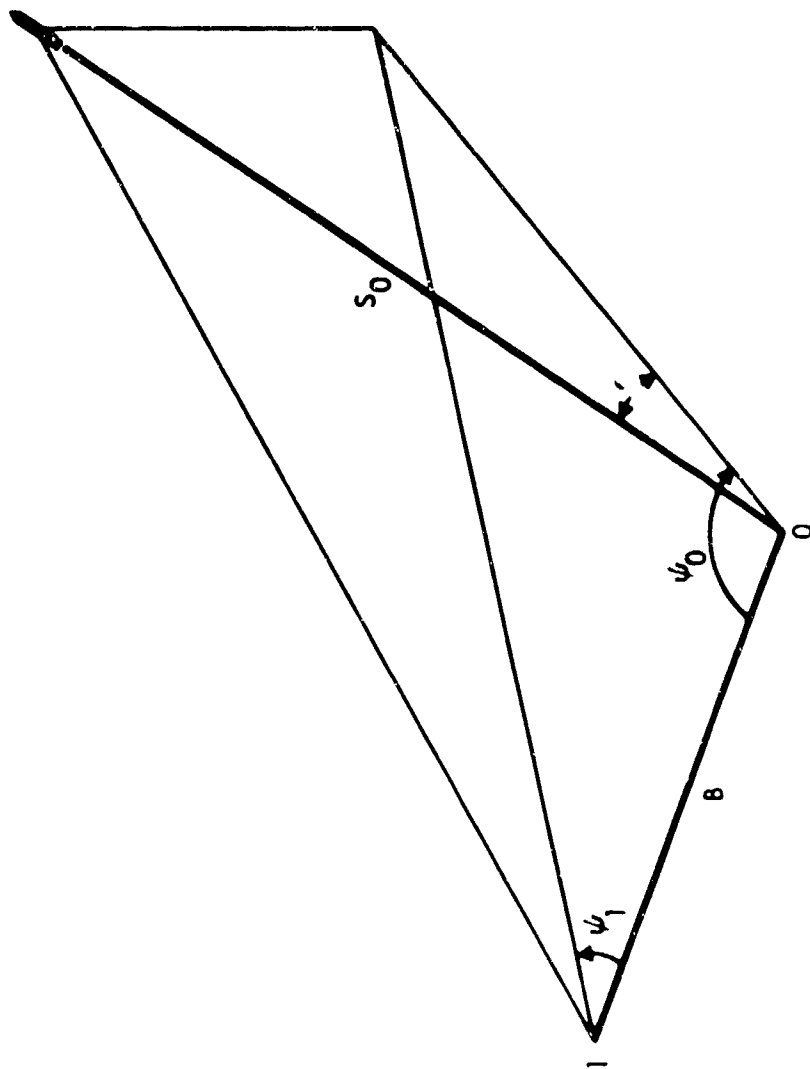


Figure 4: TWO-STATION TRACKING GEOMETRY

$$\cos \epsilon = \frac{B \sin \psi_0}{S_0 \sin(\psi_0 + \psi_1)} . \quad (21)$$

With atmospheric contributions to errors in measurement of ψ_0 and ψ_1 considered negligible, the precision to which the slant range, S , is specified determines again the precision of ϵ .

B. Target velocity

Target location and velocity are the primary concerns in tracking operations. As shown in Figure 5, target velocity is obtained by resolving the target velocity vector, \vec{V} , into its radial, V_S and angular, V_ϵ , components. The problem, then, is to obtain the measures of V_S and V_ϵ .

(1) Radial velocity

The radial component of target velocity is given simply by the time rate-of-change of slant range; i. e.,

$$V_S = \frac{dS}{dt} . \quad (22)$$

Acting on Equation 10 in accordance with Equation 22,

$$V_S = \frac{dS}{dt} = \frac{dS_e}{dt} - 10^{-6} \frac{d}{dt} \left[\int_0^S N(s) ds \right] . \quad (23)$$

Or, changing symbolism,

$$V_S = \dot{S} = \dot{S}_e - 10^{-6} \dot{\bar{N}} \quad (24)$$

where the dot represents the time derivative, and the overbar the integrated refractivity value. Equation 24 states that radial velocity is given by the "electrical velocity" diminished by the time rate-of-change of line-integrated refractivity.

(2) Angular velocity

The angular component of the target velocity vector is simply the product of slant range by angular velocity; that is,

$$V_\epsilon = S \dot{\epsilon} , \quad (25)$$

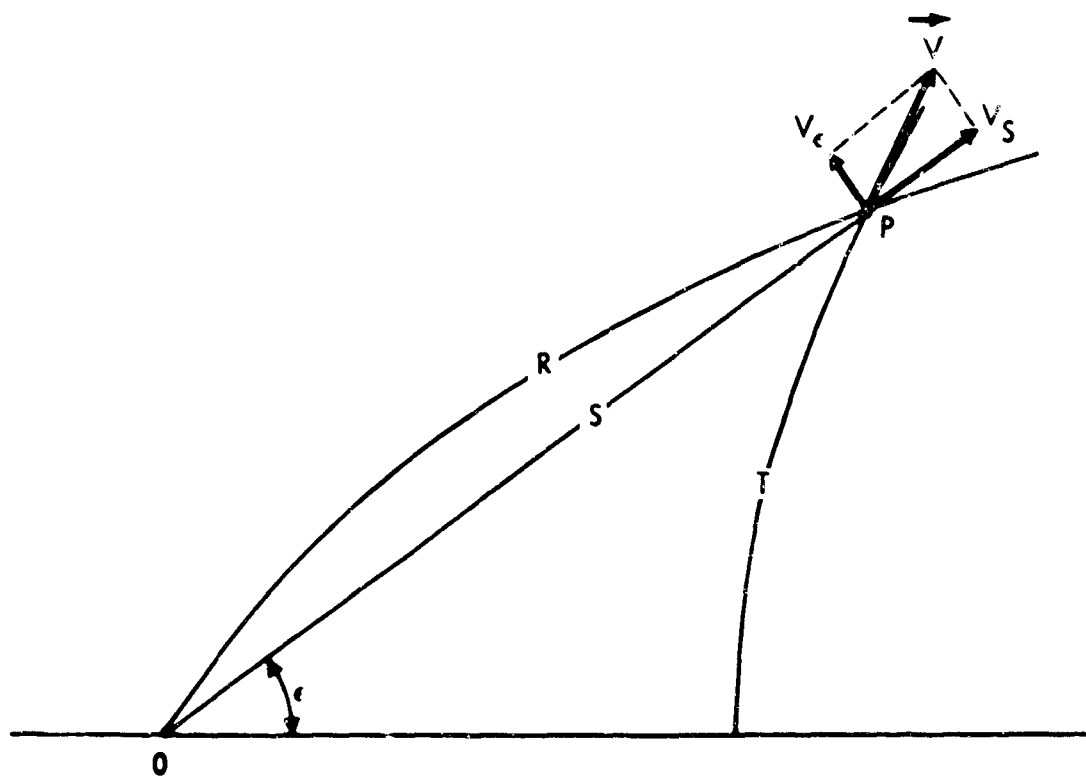


Figure 5: DEFINITION OF TARGET VELOCITY COMPONENTS

Differentiating Equation 18 by time, Equation 25 (for the interferometric or three-station trilateration measurement of ϵ) can be expressed as

$$\dot{V}_\epsilon = \frac{S_0}{\sin \epsilon \cos \epsilon} (\cos \phi_1 \sin \phi_1 \dot{\phi}_1 + \cos \phi_2 \sin \phi_2 \dot{\phi}_2) \quad (26)$$

where, from Equation 9 and Equations 11 and 19,

$$\dot{\phi}_1 = \frac{1}{-B_1 \sin \phi_1} \left\{ \left[1 - \frac{S_{D1}}{S_0} \right] \left[\dot{S}_{eD1} - 10^{-6} (\dot{N}_0 - \dot{N}_1) \right] \right. \quad (27)$$

Similarly, from Equations 12 and 20

$$\begin{aligned} \dot{\phi}_2 = \frac{1}{-B_2 \sin \phi_2} \left\{ \left[1 - \frac{S_{D2}}{S_0} \right] \left[\dot{S}_{eD2} - 10^{-6} (\dot{N}_0 - \dot{N}_2) \right] \right. \\ \left. + \frac{1}{2S_0^2} [S_{D2}^2 - B_2^2] \left[\dot{S}_{e0} - 10^{-6} \dot{N}_0 \right] \right\} \quad (28) \end{aligned}$$

Equations 27 and 28 thus call for the measurements of the time rates of change of the electrical range measured from the mother stations, of the slave-to-mother station electrical-range differences, and of the line-integrated refractivity as measured at each of the three stations, in order to evaluate $\dot{\epsilon}$.

For the two-station mode of trilateration, differentiation of Equation 21 yields

$$\begin{aligned} \dot{V}_\epsilon = \epsilon \cos \epsilon \left\{ \left[\dot{S}_{e0} - 10^{-6} \dot{N} \right] + S_0 \cot \epsilon (\psi_0 + \psi_1) \dot{\psi}_1 \right. \\ \left. - S_0 \left[\cot \psi_0 - \cot (\psi_0 + \psi_1) \right] \dot{\psi}_0 \right\} \quad (29) \end{aligned}$$

Here, the evaluation of \dot{V}_ϵ calls for measurements of the time rates of change of electrical range, of the azimuth angles, and again of the line-integrated refractivity.

(3) Doppler corrections

The alternate approach to the measurement of V_s is based on the Doppler effect, the general concept of which is that the reflection of a radio wave from a moving object results in a signal being returned to a fixed transmitting-

receiving system whose frequency differs from the transmitted frequency.

Analytically, this phenomenon is written as

$$f_d = \frac{2V_r f}{c_p} \quad (30)$$

where f_d is the difference between the received and the emitted frequency, f , c_p the speed of light at the target position, P, and V_r is the component of target velocity in the direction of the refracted ray. Figure 6 illustrates the geometry involved. According to Figure 6, the following velocity components may be defined:

$$\begin{aligned} V_s &= |\vec{V}| \cos \theta & a) \\ V_r &= |\vec{V}| \cos (\theta + \xi) & b) \\ V_a &= V_s \cos \epsilon & c) \end{aligned} \quad (31)$$

where V_s is as defined previously, V_r is the component of \vec{V} in the ray direction, and V_a the component in the direction of the apparent path (P' is the apparent target position).

Doppler frequency-shift measurements provide measures of V_r . What is desired is V_s . Therefore, the Doppler measurement error may be defined by

$$\Delta V_r = V_s - V_r \quad (32)$$

Substituting appropriately from Equation 30

$$\Delta V_r = |\vec{V}| \cos \theta - |\vec{V}| \cos (\theta + \xi) \quad (33)$$

Expanding the second cosine term,

$$\Delta V_r = |\vec{V}| \cos \theta - |\vec{V}| (\cos \theta \cos \xi - \sin \theta \sin \xi) \quad (34a)$$

or

$$\Delta V_r = |\vec{V}| \cos \theta (1 - \cos \xi) + |\vec{V}| \sin \theta \sin \xi \quad (34b)$$



ξ is a very small angle. Therefore, to good approximations,

$$\begin{aligned}\cos \xi &\approx 1 \\ \sin \xi &\approx \xi\end{aligned}\tag{35}$$

and Equation 34b transforms to

$$\Delta V_r = \xi |\vec{V}| \sin \theta\tag{36}$$

From Figure 6, it is noted that

$$\sin \theta = \cos(90 - \theta) = \frac{V_e}{|\vec{V}|}\tag{37}$$

Therefore, Equation 36 may be written

$$\Delta V_r = \xi V_e\tag{38}$$

Equation 38 illustrates that the Doppler velocity error in the radial direction attributable to refraction is composed only of the angular component of target velocity, and is therefore a maximum when the velocity vector is perpendicular to the direction of the direct path, and a minimum when the target is moving along the direct line-of-sight path. Further, notice that (1) unlike the range measurement error, the Doppler error is not cumulative (it is only the localized error at a specific target position in the medium), and (2) the magnitude of the pointing error angle, ϵ , is not significant.

Substituting from Equations 24, 30, and 38 appropriately into 32

$$\xi V_e = \dot{S}_e - 10^{-6} \frac{\dot{N}}{N} - \frac{c_F}{2} \frac{f_d}{f}\tag{39}$$

Introducing, now, Equation 4

$$\xi V_e = \dot{S}_e - 10^{-6} \frac{\dot{N}}{N} - \frac{c_0}{2} \frac{1}{n} \frac{f_d}{f}\tag{40}$$

and the above, through application of Equation 6 and to first order in $(n-1)$ is written

$$\xi V_e = \dot{S}_e - 10^{-6} \dot{N} - \frac{c_0}{2} (1 - 10^{-6} N_p) \frac{f_d}{f} \quad (41)$$

or

$$\xi V_{\beta_0} = \dot{S}_e - 10^{-6} \dot{N} - \frac{c_0}{2} \frac{f_d}{f} + 10^{-6} N_p \frac{c_0}{2} \frac{f_d}{f} \quad (42)$$

The term $c_0 f_d / 2f$ in the above equation is simply the target velocity that would be measured by a Doppler system in vacuo. This quantity is thus equivalent to the \dot{S}_e previously defined. Therefore, Equation 42 simplifies to

$$\Delta V_r = \xi V_e = 10^{-6} N_p \dot{S}_e - 10^{-6} \dot{N} \quad (43)$$

Hence, in terms of the Doppler velocity, the radial velocity is

$$V_S = V_r + 10^{-6} N_p \dot{S}_e - 10^{-6} \dot{N} \quad (44)$$

The Doppler measurement correction is that required for the radial velocity measurements plus the N_p term that accounts for refractivity conditions at the target position. For ranges long enough and elevation angles great enough, the latter term rapidly loses its significance because of the rapid decrease of N with height. In fact, after the target leaves the atmosphere, $N_p = 0$, and the Doppler correction is exactly that required for radial correction.

C. Summary

Two atmospheric effects act to cause errors in radar ranging and tracking data: (1) the material atmosphere retards ranging signals so that ray propagation speeds are less in the atmosphere than in vacuo, and (2) gradients (especially in the vertical) in the refractivity structure of the atmosphere cause a ray bending or refraction. The first effect results in errors in slant-range measurements; the second effect results in errors in elevation-angle determinations.

In the interferometric or triangulation mode of ranging operations, the direct measure of target elevation is eliminated; i. e., target position is com-

pletely specified from knowledge of receiver-to-target slant ranges relative to multiple ranging stations in a prescribed geometric configuration. Moreover, because of the purely mechanical problems of maintaining dish orientation in radars that measure elevation angle directly, it is likely that accuracies in elevation-angle specifications commensurate with the potential accuracies of slant-range determinations are attainable only with the multiple-station approach.

Improvement in the accuracy of ranging data for both position and velocity demands improvement in the measurement of slant range. The dominant need is for techniques only for estimating the ray-retardation effect, which is a function simply of the integral of refractivity over the ranging path. The difficult problem of performing the measure in real time of the refractive index gradients required for the corrections of elevation angles directly measured is thus eliminated.

3. N-MEASUREMENT TECHNIQUE SURVEY

A. Background

The description of n given by Equation 4 is purely phenomenological. It is the consideration of the actual effects of an impressed electric field upon the dielectric constants of both polar and nonpolar molecules that establishes the physical basis of a nonzero refractivity, and that relates refractivity to atmospheric composition. By such consideration has come a refractivity equation of the form (Reference 8)

$$N = A \left(\frac{p_d}{T} + B_1 \frac{e}{T} + B_2 \frac{e}{T^2} \right) \quad (45)$$

where

A , B_1 , and B_2 in the above expression are semiempirically determined constants; T is the temperature, p_d is the partial pressure of dry air, and that of water vapor. The total atmospheric pressure is thus

$$p = p_d + e \quad (46)$$

The peculiarities of Equation 45 are that at optical wavelengths, B_1 and B_2 are effectively zero, and N is therefore largely independent of the atmospheric water-vapor content; the constant A , however, is a function of wavelength. Conversely, at radio wavelengths, refractivity is not wavelength-dependent (A independent of wavelength) but is strongly affected by water vapor (Reference 9). Therefore, it is convenient and customary to present two equations for refractivity: one for optical wavelengths and the other for radio wavelengths; that is,

$$N_{\infty} = \left(K_1 + \frac{c}{\lambda^2} \right) \frac{p_d}{T} \quad (47)$$

where N_{∞} denotes the refractivity at the optical wavelengths ($\ll 20$ microns), and

$$N = K_1 \frac{p_d}{T} + K_2 \frac{e}{T} + K_3 \frac{e}{T^2} \quad (48)$$

for radio wavelengths. Regarding the radio wavelength refractivity equation: of special significance (to be emphasized later) is the difference in form of the first two terms on the right-hand side as compared to the third term. This difference arises because the first two terms express the effects on refractivity of the distortions of electronic charges of dry-gas and water-vapor molecules under the influence of an applied electromagnetic field, whereas the third term describes the effect of molecular dipole orientation. Of all the constituents of the atmosphere, only water vapor exhibits a strong dipole moment; therefore, only water vapor contributes a dipole-orientation term to the refractivity equation. Also note that the first term in the optical and radio refractivity equations are identical.

B. Point-measurement technique

Using Equations 4 and 48, radio refractivity may be measured in two ways. That is, N may be obtained directly through a measure of the ratio c_0/c , or else by calculation (using Equation 48) from measures of the atmospheric parameters p_d , T , and e .

(1) Direct measurement of N

A number of devices are capable of directly measuring radio refractivity. Although many modifications have been attempted, most such refractometers fall into three basic categories that reflect the essential principles of the original units. The three types — resonant cavities, coaxial cavities, and condensers — all involve comparisons between a sample and a reference quantity and constitute a point measurement. The most noted of the resonant frequency-type refractometers are those of Crain (Reference 10) and Birnbaum (Reference 11). The former measures the variation in frequency difference between two stabilized oscillators; the difference is proportional to the change in refractivity. The Birnbaum instrument uses passive cavities instead of the active ones employed by Crain, and it measures the time delay in response to a peak signal passing through the reference and sensing cavities. This time lag represents the frequency difference and is a measure of the refractivity. Cavity-resonating instruments typically operate near 10,000 MHz, and both the Birnbaum and Crain instruments have a number of selective scales that permit measurements over a total range of some 400 N units. For the most part, the many modifications of the Birnbaum unit result from various techniques used to determine the time delay of maximum response. System noise is approximately 0.1 N unit.

The coaxial cavity refractometer, best represented by the instrument developed by Deam (Reference 12), uses a half-wave resonant sampling cavity operating at a frequency of 400 MHz. The basic instrument is a modified Crain unit that has been designed especially for lightweight balloon or drop-sonde applications, since the sampling cavity might be located as far as 20 miles from the reference receiver.

A somewhat different approach was taken by Hay (Reference 13) in applying condensers in a resonant circuit, wherein the capacitance varies according to the changes in dielectric constant of the gas sampled between the plates. The original instrument, operating at 10 MHz, used six plates spaced about 0.25 inches apart on each side of the instrument. The primary advantage of this unit was that it could be operated remotely from its reference unit, and because it

was lighter than cavity resonators it was ideally suited to balloon operations. Handicaps occurred, however, from problems of temperature calibration and frequency response.

As early as 1951, Tolbert and Straiton (Reference 14) introduced a design significantly different from existing instruments; it was an early effort toward developing integrated refractivity devices. Microwave transmissions were sent over a 1-meter-long measuring and reference path, and a comparison of the phase shift of the received signal was interpreted in terms proportional to the mean refractive index over the path. It was determined that results obtained with this system could be made extremely sensitive to small changes in refractivity, although disadvantages appeared in attempts to thermally balance the system and in instability of the amplifier components.

(2) Calculation of N from meteorological data

The constants K_1 , K_2 , and K_3 in Equation 48 are of the values (Reference 15):

$$\begin{aligned} K_1 &= 77.607 \pm 0.013 \quad ^\circ\text{K mb}^{-1}, \\ K_2 &= 71.6 \pm 8.5 \quad ^\circ\text{K mb}^{-1}, \\ K_3 &= (3.747 \pm 0.051) 10^5 \quad ^\circ\text{K mb}^{-1}. \end{aligned} \quad (49)$$

The K values contained in Equation 49 were evaluated by Bean from a survey of determinations of the dielectric constants of both dry air and water vapor conducted by various researchers. The final results represent the weighted means of the various determinations, the weights being taken inversely proportional to the square of the probable errors. In rounding the K values to three figures where significant, and assuming the total air pressure to equal the sum of the dry-air and water-vapor pressures, the following simplified refractivity equation obtains:

$$N = 77.6 \frac{p_d}{T} + 72 \frac{e}{T} + (3.75 \times 10^5) \frac{e}{T^2}. \quad (50)$$

The K values specified in Equation 50 are those suggested by Smith and Weintraub (Reference 16), and are stated as being good to 0.5 percent in N for the normal ranges of temperatures, pressures, and humidities encountered in the atmosphere. In recognition of their work, Equation 50 is usually called the Smith-Weintraub equation. The basic uncertainty of the refractivity equation is compounded by errors of measurement of p, T, and e. With errors common in radiosonde measurements, the residual error in N would, in fact, be closer to something like 1.5 percent (or on the order of a few N units). The advantage of the direct over the indirect measure of N is obvious.

(3) Integrated refractivity value

By far the greatest amount of effort toward supplying the integrated refractivity demanded in ranging operations has been expended in searching for techniques to interpret point-measured refractivity in terms of the integrated value. In a perfectly homogeneous, quiescent atmosphere, any of the point-measurement techniques listed above could be used to determine such integrated data, the value simply being the measurement obtained at one point of a given propagation path multiplied by path length. Tacit here, is the assumption that the single-point measurement provides an accurate estimate of the average refractivity value all along the path. But usually the atmosphere is not quiescent, and refractivity is a function of position. The requirement for the true integral value of N permits the interpretation that, even though errorless determination of N at each of, say, k sampling points was made, the average N computed from such data would still be subject to a finite sampling error to the extent that

$$\frac{1}{k} (N_1 + N_2 + \dots + N_k) \neq \frac{1}{S} \int_0^S N(s) ds \quad (51)$$

The above inequality defines the sampling error, and is the basic reason that even though statistical accuracies of from 1 to 3 percent in the estimation of atmospheric effects on range data are attainable from radiosonde or refractometer profiles (Reference 17), in real time a residual error more like three times that amount is the more realistic figure (Reference 18).

C. Normal dispersion technique

Taking advantage of the normal and completely predictable monotonic decrease of the index of refraction with increasing wavelength (i.e., dispersion) in the optical portion of the spectrum (Equation 47)), Owens and Bender (Reference 19) have developed a technique for the direct measure of the optical line-integrated refractivity. Assume that time-delay (interferometric) determinations are made at two wavelengths, λ_1 and λ_2 , in the optical portion of the spectrum. Take λ_1 as the shorter wavelength. Then the difference between the range contributions at the two wavelengths will be, according to Equation 8,

$$S_{\lambda_1} - S_{\lambda_2} = 10^{-6} A \int N_{\lambda_2}(s) ds \quad (52)$$

where

$$A = \frac{n_{\lambda_1} - n_{\lambda_2}}{n_{\lambda_2} - 1} \quad (53)$$

The integrated value of refractivity at wavelength λ_2 is thus directly obtained from range measurements at two wavelengths in the portion of the electromagnetic spectrum exhibiting normal dispersion.

The instrumentation consists of sources of modulated (in the UHF or microwave range) red and blue light (the 6328-angstrom helium-neon laser line and the 3660-angstrom mercury line, respectively). Both colors are propagated over the ranging path and then reflected back to a receiver, where amplitude or polarization modulation techniques are used to provide the measure of $S_{\lambda_1} - S_{\lambda_2}$. With such a system, accuracies in the direct measurement of \bar{N} of better than 1 percent are deemed feasible. Such accuracy in \bar{N} measurement would result in about an order-of-magnitude improvement in the accuracy of slant-range measurement over that now achievable through electrical-range corrections based on \bar{N} estimates from point-measurement data. However, the technique cannot be applied directly to the case of radar ranging, because, in effect, only the first term of the integrated radio refractivity equation is so determined. The technique provides no means whereby the second and third terms may be

measured. Strictly speaking, the technique is applicable only to optical ranging devices such as the geodimeter (Reference 20). Another disadvantage is that cooperative targets on which the required reflector could be mounted are mandatory for operation of the system in conjunction with ranging operations.

D. Anomalous dispersion technique

In the radio region of the spectrum, refractive index is largely independent of wavelength. Therefore, the normal dispersion technique of measuring line-integrated refractivity is not applicable. In the neighborhood of atmospheric constituent absorption bands, however, an anomalous dispersion is associated with the molecular resonances of the particular absorbing constituents. Specifically, on the long wavelength sides of such bands the refractivities fall to abnormally low values, whereas on the short wavelength sides such values are abnormally high. Moreover, the magnitude of the dispersion is proportional to the general level of refractivity about the band. This magnitude, in turn, can be determined from the difference in ray-propagation transit times associated with the dispersion across the band. Specifically, if Δt_1 and Δt_2 denote ray transit times — one above and the other below a given absorption band — then

$$\Delta t_1 - \Delta t_2 = K \int N(s) ds \quad (54)$$

where, as an example, if the transit time difference is determined across a water-vapor absorption band, the integral represents the integrated water-vapor refractivity. Because total refractivity is the sum of a dry-air term and a water-vapor term; i.e.,

$$N_{\text{Total}} = AN_0 + BN_W \quad (55)$$

then a similar measurement across an absorption band of one of the dry-air constituents will suffice to determine total line-integrated refractivity. This is the technique of \bar{N} measurement currently being investigated by Sullivan and Richardson of the Mitre Corporation (Reference 21).

An instrument capable of measuring the differential transit time due to water vapor has been developed and field tested. It consists of a source composed of two phase-coherent waves at 15.6 and 32.2 GHz transmitted to free space through a Cassegrainian parabolic antenna. The transmitted energy is detected by a system using a similar antenna in the receiver. A local oscillator is incorporated to provide two IF carrier frequencies; one at 250 kHz to carry the phase information of the lower transmitted frequency, and one at 500 kHz to carry the information on the higher frequency. The 250-kHz signal is doubled, and the phases of the two are then compared by a null-detecting digital phase shifter. The amount of phase shift to achieve the null is the measure of the differential transit time.

Theoretically, accuracies in \bar{N} measurement comparable to those achievable with the normal dispersion system can be anticipated with the Mitre system. However, field test with the water-vapor system have shown that the data obtained by the system consist of an average level and a widely variable fluctuating component about the average level (Reference 22). The average level is determined by the integrated humidity in the path, whereas the majority of the noise component is due to random phase scintillation effects associated with the propagation of electromagnetic energy through a turbulent atmosphere. Consequently, prohibitively long averaging times (with the attendant loss of real-time capabilities) are required to recover meaningful data.

Further, the transit time differentials that are ascribable to the anomalous dispersion, and which must be measured, are on the order of picoseconds (10^{-12} seconds). A capability for such measurement severely taxes the state of the art of microwave electronics. Although the Mitre system represents a significant achievement, and although the experimental system has proven itself, there might be problems in maintaining the stability and reliability of such a system in routine ranging operations.

The final drawback is that, again, cooperative targets would be required when applying the system to ranging operations.

E. Summary

The need to measure line-integrated refractivity in ranging operations has resulted in extensive research into techniques for estimating \bar{N} from point-measurement refractivity data. The limit of such techniques has just about been reached; still, uncertainties of from 5 to 10 times the magnitude desired remain in the real-time specification of \bar{N} . The problem is the inadequacy of the representation of an integrated function as a finite sum. Moreover, the sheer problem of logistics in providing an adequate number of point measurements in real time to attain the desired degree of precision in the estimated integrated value practically precludes the use of point-measurement techniques in ranging operations.

Two approaches to the direct measure of the true integrated function have been suggested. Both are based essentially on the concept that dispersion (wavelength-dependent refractivity) results in finite ray transit time differences at different radiation wavelengths. Measures of the magnitudes of such differences therefore provide the measure of integrated refractivity. The normal dispersion at optical wavelengths is used to provide information regarding the optical refractivity; the anomalous dispersion around atmospheric constituent absorption bands can be used similarly to determine the radio refractivity. Accuracies in \bar{N} measurement theoretically attainable with each system would more than satisfy the requirements of ranging operations. However, the normal dispersion technique suffers because (1) it provides \bar{N} data applicable only to optical wavelengths, and (2) cooperative targets would be needed if the approach were applied to ranging operations. The anomalous dispersion technique suffers because (1) a capability for measuring short-term \bar{N} fluctuations is lacking, (2) the system is borderline technically, and (3) cooperative targets again would be needed for its application to ranging operations.

4. RADIATION ABSORPTION AND THE PARAMETERS OF LINE-INTEGRATED REFRACTIVITY

As a basis for an alternate approach to the measurement of line-integrated refractivity, consider the following. Basically, refraction effects constitute a phenomenological record of the influence of the atmosphere on the phase of

propagated electromagnetic signals. But the atmosphere acts not only on wave phase, but also, at certain precisely defined frequencies, on wave amplitude. This latter action gives rise to the familiar phenomenon of energy absorption. The net result is that not only is the energy propagation speed altered, but so is the actual spectral content of that energy (within specified frequency intervals). Although these two phenomena may have widely different physical manifestations, it is important to recognize the common origin of both — the interaction, at the molecular level, of the atmosphere with an applied electromagnetic field. It is not too surprising that, in spite of the differences mentioned, a phenomenological description of one effect can be interpreted in terms of a description of the other.

A. Equation of radiative transfer

Regarding the absorption process mentioned above: The totality of molecular interactions between radiation and matter can be classed as either absorption or emission. The two processes are distinguished by the sign of the change of radiant intensity as a result of the interaction. If the intensity decreases, then absorption occurs; intensity increases are ascribed to emission.

The fundamental law of absorption is that of Bouguer. It states that for monochromatic radiation the absorption process is linear independently of the intensity of the radiation and in the amount of matter, provided that the physical state is held constant. The mathematical statement of Bouguer's law is as follows: if the space rate of diminution of radiant intensity along the direction of propagation is defined, then the change in intensity in traversing an infinitesimal element of this path is

$$dI_{\nu}(\text{absorption}) = -I_{\nu_0} \alpha_{\nu} ds \quad (56)$$

where I_{ν_0} is an intrinsic source intensity, ds is the infinitesimal path element, and α_{ν} is the previously defined space rate of intensity diminution. This latter quantity is usually called the "volume absorption coefficient."

The argument that the absorption process is linear in the amount of matter also applies with equal force to the emission process. As a formal statement,

$$dI_{\nu}(\text{emission}) = + \alpha_{\nu} J_{\nu} ds \quad (57)$$

where J_{ν} is defined as the source function of the emitting media.

The earlier statement that all interactions can be classed as absorption or emission can now be summed up in the statement that any change in intensity resulting from the interaction of matter and radiation must be the sum of Equations 56 and 57; i.e.,

$$dI_{\nu}(\text{Total}) = dI_{\nu}(\text{absorption}) + dI_{\nu}(\text{emission}) \quad (58)$$

Using the definitions provided by Equations 56 and 57, the solution to Equation 58 is (Reference 23)

$$I_{\nu} = I_{\nu 0} e^{-\int_0^s \alpha_{\nu}(s') ds'} + \int_0^s \alpha_{\nu}(s') J_{\nu} e^{-\int_0^{s'} \alpha_{\nu}(s'') ds''} ds' \quad (59)$$

where again the first term on the right-hand side of Equation 59 describes the absorption (as governed by the term's exponential attenuation factor) of the intrinsic source energy, the second term describes the self-emission process. The exponential factor also appears in the second term, expressing the fact that any energy emitted at any point along the propagation path suffers the same absorption in its subsequent travel as does the intrinsic source energy. While Equation 58 and its solution (Equation 59) sets the pattern of the formalism used in radiation transfer problems, its physical content is very slight. The physics is mainly contained in the definition of α_{ν} .

B. Specification of the absorption coefficient

So far, the absorption coefficient has been given only a phenomenological description. The actual physics of the absorption process lies in the interactions between the incident radiation and the energy modes of the individual molecules. Specifically, radiation is absorbed when it is of the proper frequency (as determined by the Bohr frequency relation) to cause a molecule to be raised from one molecular state to another of higher energy.

In a general way, the energy of a molecular state may be written as the sum of four terms:

$$E = E_e + E_v + E_r + E_t \quad (60)$$

where E_e , E_v , E_r , and E_t are the electronic, vibrational, rotational, and translational energies, respectively. It is further found that $E_e \gg E_v \gg E_r \gg E_t$; consequently, the frequencies of the radiation required to effect transitions in the energy levels associated with each of the four terms vary in the same manner. That is, E_e transitions, caused by the highest frequency radiation, produce band spectra that lie in the ultraviolet and visible regions of the electromagnetic spectrum. Pure vibration, vibration-rotational, and pure-rotation spectra occur, progressively, in the near through far infrared. Translational spectra are restricted to the radio regions.

(1) General quantum-mechanical, molecular absorption coefficient

Electric or magnetic dipole or quadrupole moments are involved in the interactions between matter and incident electromagnetic fields that result in energy absorption. Electric dipole interactions are stronger by a factor on the order of 10^5 than magnetic dipole interactions; electric dipole interactions are on the order of 10^8 times stronger than electric quadrupole interactions. Electric dipole transitions are, therefore, responsible for the strongest spectral lines, and are called "permitted" transitions. Other transitions are loosely named "forbidden." For a single spectral line, the absorption coefficient is related to the intensity of the permitted dipole transition, according to (Reference 24).

$$\gamma_{ij} = \frac{8\pi^3 \nu_{ij} n_a}{3hc} \frac{\left\{ \sum_j \sum_j |R_{ij}|^2 + (\nu_{ij}, \nu) \right\} e^{-\frac{E_i}{kT}}}{\sum_j e^{-\frac{E_j}{kT}}} \quad (61)$$

where R_{ij} is the matrix element of the dipole moment connecting two stationary states, i, j , of energy E_i, E_j , respectively; ν_{ij} is the frequency of the corresponding spectral line, given by the Bohr frequency condition $h\nu_{ij} = E_i - E_j$;

n_a is the number density of the absorbing molecular specie, T is the temperature, h is the Planck constant, k is the Boltzmann constant, and c is the speed of light. The frequency of the incident radiation is denoted by ν . The exponential is termed the Boltzmann factor, and the factor $f(\nu_{ij}, \nu)$ is the so-called "structure function" that determined the shape of the absorption line. For the Lorentz pressure-broadened line shape,* the expression for $f(\nu_{ij}, \nu)$ is (Reference 24):

$$f(\nu_{ij}, \nu) = \frac{\nu}{\pi \nu_{ij}} \left[\frac{\Delta \nu}{(\nu_{ij} - \nu)^2 + \Delta \nu^2} + \frac{\Delta \nu}{(\nu_{ij} + \nu)^2 + \Delta \nu^2} \right] \quad (62)$$

where $\Delta \nu$ is the line width; i.e., the half-width of the line at half intensity.

Near resonance, Equation 62, can be written as

$$f(\nu_{ij}, \nu) \propto \frac{1}{\pi} \left[\frac{\Delta \nu}{(\nu_{ij} - \nu)^2 + \Delta \nu^2} \right] \quad (63)$$

Equation 63 is a valid representation of the structure function at optical and near-through middle-infrared wavelengths. Microwave absorption line structures, however, must be described in terms of Equation 62.

(2) ϵ_ν as a function of frequency

Equation 61 is the general quantum-mechanical expression for the molecular absorption coefficient. As $h\nu_{ij} = E_i - E_j = -h\nu_{ji}$ it follows that $f(\nu_{ij}, \nu) = -f(\nu_{ji}, \nu)$. To any given term i, j in the double sum called for in

* Atmospheric pressures in the portion of the atmosphere where there is any significant absorption allow the Lorentzian line shape to be assumed. Doppler line-broadening effects are significant only in the high-altitude rarefied atmosphere that contributes little to absorption, and, hence, refractivity.

Equation 61, there is also a corresponding term $-j, i$ — whose contribution is of the opposite sign, and which differs from the i, j term only to the extent of the difference in the Boltzmann factor for the j - as opposed to the i -state. If, in fact, $h\nu_{ij} \ll kT$, a condition characteristic of microwave wave frequencies, the effects of the i, j and j, i terms very nearly cancel each other. This difficulty of nearly compensating terms in the microwave region of the absorption spectrum is avoided with the following approximation:

$$n_{ij} e^{-\frac{E_i}{kT}} + n_{ji} e^{-\frac{E_j}{kT}} = \frac{1}{2} \frac{h\nu_{ij}^2}{kT} \left(e^{-\frac{E_i}{kT}} + e^{-\frac{E_j}{kT}} \right) \quad (64)$$

Use of the above simplification in Equation 61 defines now, the microwave absorption coefficient as

$$\gamma_{\mu\text{-wave}} = \frac{8\pi^3 n_a}{6ckT} \frac{\left[\sum_i \sum_j IR^2 n_{ij} f(\nu_{ij}, \nu) e^{-\frac{E_i}{kT}} \right]}{\sum_j e^{-\frac{E_j}{kT}}} \quad (65)$$

By performing the indicated summations over the contributing energy states exhibiting appreciable population at the temperatures encountered in the atmosphere, the molecular absorption coefficients for water vapor and for oxygen may be written (Reference 24)

$$\gamma_{\mu\text{-wave}}^{\text{H}_2\text{O}} = c_1 \frac{n_{\text{H}_2\text{O}}}{T} \nu^2 \Delta\nu \left[\frac{1}{(\nu - \nu_0)^2 + (\Delta\nu)^2} + \frac{1}{(\nu + \nu_0)^2 + (\Delta\nu)^2} \right] \quad (a) \quad (66)$$

$$\gamma_{\mu\text{-wave}}^{\text{O}_2} = c_2 \frac{n_{\text{O}_2}}{T} \nu^2 \Delta\nu \left[\frac{1}{(\nu - \nu_0)^2 + (\Delta\nu)^2} + \frac{1}{(\nu + \nu_0)^2 + (\Delta\nu)^2} + \frac{1}{\nu^2 + (\Delta\nu)^2} \right] \quad (b)$$

at microwave regions, and (Reference 25)

$$\begin{aligned}\gamma_{IR}^w &= B_1 n_w \left[\frac{\Delta \nu}{(\nu - \nu_0)^2} \right] \\ \gamma_{IR}^{o_2} &= B_2 n_{o_2} \left[\frac{\Delta \nu}{(\nu - \nu_0)^2} \right]\end{aligned}\tag{67}$$

at infrared regions. In the above equations, ν_0 denotes the resonant frequency of the appropriate absorption lines. The units of the C's and B's that appear in the equations are determined by the units of radiation transfer measurements.

(3) Volume absorption coefficients

Recognizing now, the relationship that exists between number density and mass density; i. e.,

$$\rho_a = \frac{M_a}{N} n_a,\tag{68}$$

where M_a is the molecular weight of constituent a, and N is Avogadro's number, a significant fact emerges from comparison of Equations 66 and 67; viz., in terms of the volume absorption coefficient, absorption at microwave frequencies proceeds in proportion to the ratio of absorbing constituent density to temperature, whereas at infrared frequencies the proportion is according to density alone.

That is,

$$\alpha_{microwave}^a = C' \frac{\rho_a}{T} f_a(\nu, \Delta \nu)\tag{69}$$

and

$$\alpha_{IR}^a = B' \rho_a f_a(\nu, \nu_a)\tag{70}$$

where the constants are adjusted according to Equation 68.

C. Specification of line-integrated refractivity

Consider now, the modification of Equation 48 according to the equation of state for dry air,

$$\frac{p_d}{T} = R \rho_a\tag{71}$$

and for water vapor

$$\frac{e}{T} = R' \rho_w\tag{72}$$

where R and R' are the gas constants for dry air and for water vapor, respectively; ρ_a denotes the partial density of dry air, ρ_w that of water vapor, or absolute humidity. Applying Equations 71 and 72 to Equation 48, the expression for N becomes

$$N = K_1 R \rho_d + K_2 R' \rho_w + K_3 R' \frac{\rho_w}{T} \quad (73)$$

With the R and ρ values expressed in units of $\text{in}^2 \text{sec}^{-2} \text{K}^{-1}$ and gm m^{-3} , respectively, the K values of Equation 47 are redefined to a new set according to

$$\begin{aligned} K_1 &= KR = (222.728 \pm 0.037) 10^{-3} \text{ m}^3 \text{ gm}^{-1} \\ K_2 &= K_2 R' = (330.4 \pm 39.2) 10^{-3} \text{ m}^3 \text{ gm}^{-1} \\ K_3 &= K_3 R' = (17.242 \pm 0.143) 10^{-2} \text{ K m}^3 \text{ gm}^{-1} \end{aligned} \quad (74)$$

Equation 48 can thus be written as

$$N = k_1 \rho_d + k_2 \rho_w + k_3 \frac{\rho_w}{T} \quad (75)$$

Equation 75 can be further simplified when it is recognized that the dry-air constituents exist very nearly in constant proportion to one another. Therefore, the partial dry-air density can be expressed in terms of the partial density of oxygen according to

$$\rho_d = \frac{\rho_{O_2}}{\omega_{O_2}} \quad (76)$$

where ρ_{O_2} denotes now the partial density of oxygen, and ω_{O_2} denotes the oxygen mixing ratio (i.e., percent by weight of oxygen to the total dry-air mass per unit volume). The numerical value of ω_{O_2} is

$$\omega_{O_2} = 0.2314 \pm 5 \times 10^{-5} \text{ gm/gm} \quad (77)$$

The uncertainty indicated in the above equation arises from the variations in atmospheric carbon dioxide content established by the release of CO_2 to the atmosphere by combustion processes and by biological exchanges of CO_2 with soil and vegetation. Equation (76) at any rate, permits Equation 75 to be written

$$N = \frac{k_1}{\omega_{02}} \rho_{O_2} + k_2 \rho_w + \frac{k_3}{T} \rho_w \quad (78)$$

The integrated refractivity is thus

$$\bar{N} = \frac{k_1}{\omega_{02}} \int \rho_{O_2} ds + k_2 \int \rho_w ds + k_3 \int \frac{\rho_w}{T} ds \quad (79)$$

The full impact of Equations 69 and 70 can be appreciated now, when a comparison is made between these equations the radiative-transfer equation (59) and the \bar{N} equation (79). Because of the appearance of the integrals of the absorption coefficient in the exponential radiation attenuation factors of the radiation transfer equation, the physics of radiative transfer defines, in effect, measurable quantities, I_ν 's, which, depending on the frequency of radiation considered, are functions of precisely the quantities required for an evaluation of line-integrated refractivity as specified by Equation 79. That is,

$$I_{\nu_{IR}}^a = g_{IR} \left(\int_0^s \rho_a ds \right) \quad (80)$$

$$I_{\nu_{\mu\text{-wave}}}^a = g_{\mu\text{-wave}} \left(\int_0^s \frac{\rho_a}{T} ds \right)$$

Inversions of Equations 80 therefore yield

$$\int_0^s \rho_a ds = G_{IR} (I_{\nu}^a) \quad (a) \quad (81)$$

$$\int_0^s \frac{\rho_a}{T} ds = G_{\mu\text{-wave}} (I_{\nu}^a) \quad (b)$$

which are the atmospheric input parameters demanded by Equation 79. Therefore, Equation 79 may be written

$$\bar{N} = k_1' \cdot G_{IR}(l_2^{\omega}) + k_2 \cdot G_{IR}(l_2^{\omega}) + k_3 \cdot G_{\mu\text{-wave}}(l_2^{\omega}) \quad (82)$$

where k_1' is defined as k_1/ω_2 . Transmission measurements performed at infrared frequencies in an oxygen and in a water-vapor absorption band, respectively, therefore determine the first two terms of the line-integrated refractivity equation, and similar measurements performed in a water-vapor band at microwave frequencies provides the measure of the last term. This fact provides the basis for the development of a radiometric line-integral refractometer.

D. Summary

There is a close relationship between absorption and refraction of electromagnetic energy because both phenomena originate in the molecular interaction of the atmospheric gases with an impressed electromagnetic field. That is, both absorption and refraction proceed in proportion to atmospheric composition. Also, the relationships are such that at optical frequencies (wavelengths less than 20 microns), the form of the atmospheric input parameter to absorption calculations is precisely that of the electronic-charge distortion terms of line-integrated refractivity; at microwave frequencies the absorption parameter form matches that of the \bar{N} dipole orientation term. This fact, plus the fact that the dry-air constituents exist in remarkably constant proportion (so that knowledge of the density of one such constituent constitutes such knowledge of all the rest) provides the basis for the development of a radiometric line-integral refractometer. For if radiation transfer measurements (measures of absorbed radiation intensity) are performed in oxygen and in water-vapor absorption bands at near-infrared frequencies, and in a water-vapor band at microwave frequencies, the data so acquired may be interpreted to determine precisely all three terms of the line-integrated refractivity equation.

5. ACTIVE AND PASSIVE RADIOMETRIC SYSTEMS

In the approach to the measurement of line-integrated refractivity just outlined, two operating modes can be considered. First, assume that an intrinsic source of monochromatic energy was available and that its apparent intensity could be continuously monitored. Then, considering for this case that $J_\nu = 0^*$, Equation 59 reduces to

$$I_\nu = I_0 e^{-\int_0^S \alpha_\nu(s') ds'} \quad (83)$$

Equation 83 is readily inverted to yield

$$\int_0^S \alpha_\nu(s') ds' = -\ln \frac{I_\nu}{I_0} \quad (84)$$

Thus, the integral of the absorption coefficient is simply given as the negative, natural logarithm of the ratio of the received-to-emitted-source energy intensity. This is termed the active system mode of operation. The instrument to determine the desired ratio would be termed a "transmissometer."

For the second case, suppose an intrinsic source was not available for monitoring. Then measurements of I_ν would depend solely on measurements of atmospheric thermal radiation. In this case Equation 59 reduces to

$$I_\nu = \int_0^S \alpha_\nu(s) J_\nu e^{-\int_0^s \alpha_\nu(s') ds'} \quad (85)$$

An explicit inversion of Equation 85 is not possible, so a solution for the integral of the absorption coefficient must be obtained by numerical techniques. This is the passive-system mode of operation, with the instrument termed a radiometer.

* This condition can be realized in one of two ways: (1) specify a frequency at which the thermal emission of the atmosphere is negligible, or (2) modulate the source and employ a background rejection mode of operation.

In tracking operations, what is desired is the measure of refractivity integrated precisely over the path from target to receiver. With a cooperative target, such a measure may be obtained by mounting a radiation beacon or beacon transponder on the target itself and monitoring continuously the apparent beacon intensity as the target is tracked. This mode of operation will provide the greatest precision in \bar{N} -measurement and, hence, in range parameter measurement. The active-system approach is the desired approach, and it is applicable to operation at missile test ranges.

Suppose, however, noncooperative targets are to be tracked. Here, the passive-system mode of operation is mandatory. While such targets are beyond the atmosphere, such a system provides an accurate \bar{N} -measurement because the passive system will sense the emitted radiation contributed by the entire depth of the atmosphere. However, for targets imbedded within the atmosphere, the accuracy is degraded because only the contribution between target and receiver is the governing parameter for the range corrections. A variable frequency radiometer could, after the method of Westwater (Reference 26), provide a capability for a degree of profiling, however, so this error-source could be somewhat minimized. Residual \bar{N} errors (hence, residual range-errors) would still be greater than those characteristic of the active system.

So the set of circumstances is as follows: A desire for the greatest accuracy demands an active system, but expediency may require the passive system. Therefore, the ideal radiometric line-integral refractometer ought to be one that is operable in either the active or passive mode — the active mode for the most precise measurements with cooperative targets, the passive mode such that the measurement capability may be extended to the case of noncooperative targets.

A. Active \bar{N} -measurement system

Regarding the active-system mode of operation, the measure of I_ν required for the determination of line-integrated refractivity is usually expressed in terms of the transmittance, which is defined simply as the ratio of the received-to-emitted energy:

$$\tau_\nu = \frac{I_\nu}{I_{\nu_0}} \quad (86)$$

The complement of transmittance is termed absorptance:

$$A_\nu = 1 - \tau_\nu \quad (87)$$

Both transmittance and absorptance are dimensionless quantities and are of magnitudes that can vary between zero and unity.

The absorption process is not the only process that acts to attenuate a beam of radiant energy that traverses the atmospheric medium. Further attenuation can come about as a result of a redirection of a portion of that energy, which is due to deformation of energy wave fronts through encounters with atmospheric suspensoids. This mechanism of radiation attenuation is termed scattering attenuation. Generally, it also is a frequency-dependent process, but in contrast to the absorption process, the dependence is much weaker and is monotonic in frequency. The picture that emerges then is that the band spectrum attributable to the absorption process, and which provides the basis for the radiometric measure of line-integrated refractivity, is superimposed upon a continuum spectrum that is largely attributable to the scattering process but which also contains a contribution representing the effect of summation of the wings of thousands of absorption lines occurring in the "selective" absorption. Obviously, some account must be taken of this continuum attenuation if the measure of transmittance is to be interpreted in terms of the integrals of the atmospheric-constituent partial densities required to define line-integrated refractivity.

(1) Need for a reference band

The basis for an accounting for the continuum attenuation is provided by the fact that the processes of absorption and scattering are linear. At any radiation frequency then, the total attenuation, or extinction, can be written as the sum of the separate absorption and scattering attenuations (Reference 23):

$$\text{Extinction} = \text{Absorption} + \text{Scattering} \quad (88)$$

As a consequence of the above, transmittance demonstrates a multiplication property such that total transmittance represents the product of the component transmittances. That is,

$$\tau_{\nu_T} = \tau_{\nu_1} \cdot \tau_{\nu_2} \quad (89)$$

where the subscripts T, a, and s demark the total, absorption, and scattering transmittances, respectively.

Assume that radiation intensity measurements were performed not only in the required absorption band but also in an adjacent band lying in an atmospheric "window." From Equations 86 and 89 it can be seen that the absorption band intensity would be related to the intrinsic source energy according to

$$\begin{aligned} I_{\nu_{sens}} &= I_{\nu_{0,sens}} \cdot T_T \\ &= I_{\nu_{0,sens}} \cdot T_a \cdot T_s \end{aligned} \quad (90)$$

where the subscript "sens" denotes the absorption-band, or sensing-band, energy. The window, or reference-band, energy intensity would suffer attenuation due only to the scattering process. Therefore,

$$I_{\nu_{ref}} = I_{\nu_{0,ref}} \cdot T_s \quad (91)$$

The ratio of the sensing-to-reference-band energy intensities would then be

$$\frac{I_{\nu_{sens}}}{I_{\nu_{ref}}} = \frac{I_{\nu_{0,sens}} \cdot T_a \cdot T_s}{I_{\nu_{0,ref}} \cdot T_s} \quad (92)$$

If the scattering transmittances at the sensing and reference bands can be assumed equal, then Equation 92 reduces to

$$\frac{I_{\nu_{sens}}}{I_{\nu_{ref}}} = \frac{I_{\nu_{0,sens}}}{I_{\nu_{0,ref}}} \cdot T_a \quad (93)$$

Therefore,

$$T_a = K \cdot \frac{I_{\nu_{sens}}}{I_{\nu_{ref}}} \quad (94)$$

where K, the ratio of the intrinsic reference-band energy to the intrinsic sensing-band energy can be treated as a constant parameter of the measurement system.

The residual of the received sensing-to-reference-band energy ratio is thus a function basically of the desired absorption transmittance. The technique of performing the above-defined band energy-ratio measurement not only results in the acquisition of the direct measure of the absorption transmittance, but also eliminates the need for a highly calibrated intrinsic source. The only source requirement is stability.

(2) Selection of sensing- and reference-band frequencies — clear-weather system

The entire electromagnetic spectrum — from the ultraviolet through the radio regions — is rich in atmospheric absorption bands that are potentially useful for the development of a spectrographic, differential-absorption, line-integral refractometer. The problem of which particular bands to use as the basis for instrument development immediately presents itself. And arbitrary as the selection might at first seem, several considerations will narrow the choice. First, there is the criterion for selection provided by Equation 81. That is, for the most precise measurement of line-integrated refractivity, the first two terms in the \bar{N} equation should be determined from spectrographic measurements in the "optical" portion of the electromagnetic spectrum, the third term should be determined from similar measurements performed in the millimeter region.

(A) "Optical" absorption bands

The frequency dependence of scattering attenuation is extremely complex and will be thoroughly discussed in later sections. At present, a general rule will suffice: For given particle size distributions, the higher the frequency the more efficient the scatter. The lower-frequency (longer wavelength) "optical" radiation thus has the greater ability to penetrate the atmospheric aerosol, thereby increasing the effective range of any measurement system. Accordingly, the chosen absorption bands should be on the low-frequency end of the optical spectrum. Consider, therefore, the solar absorption spectrum normalized to peak transmission that has been presented by Gates and is shown in Figure 7. The spectrum in Figure 7 is characterized by four strong-overtone bands of the vibration-rotation water-vapor spectrum, two weak-overtone bands of the carbon dioxide spectrum,

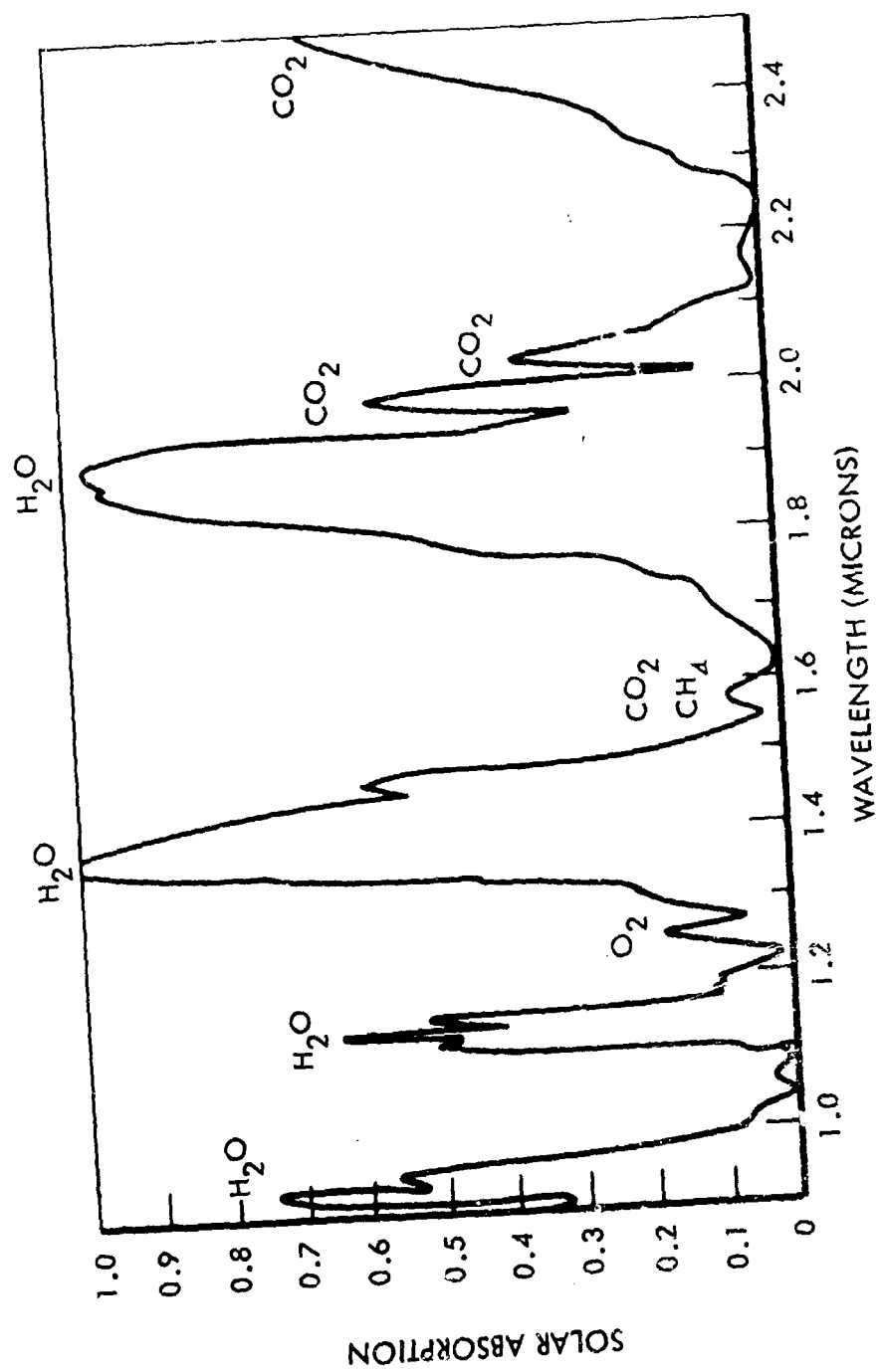


Figure 7: THE NEAR-INFRARED SOLAR ABSORPTION SPECTRUM

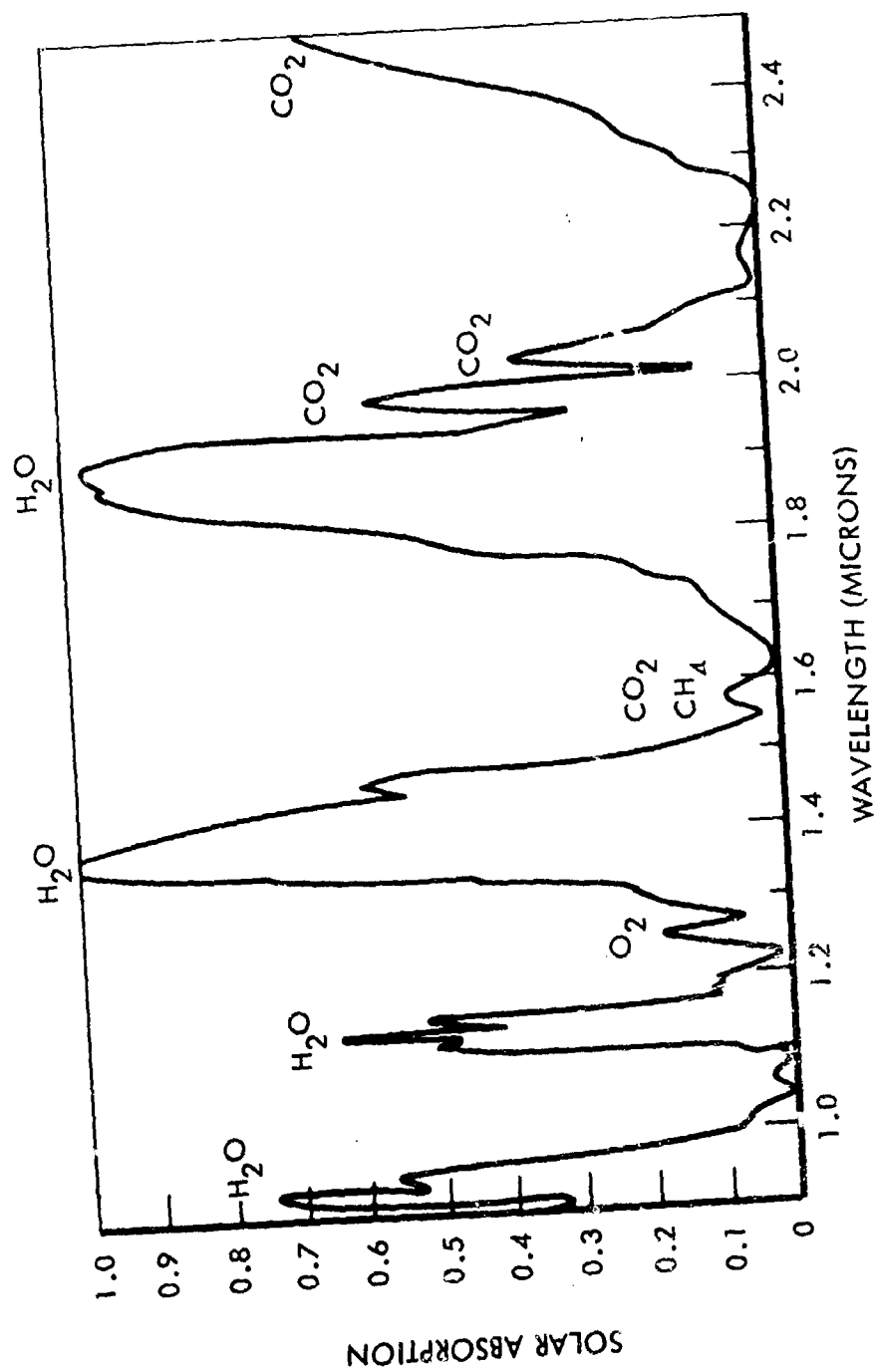


Figure 7: THE NEAR-INFRARED SOLAR ABSORPTION SPECTRUM

and one weak band of the 0-0 rotational oxygen spectrum. Also indicated are four window regions. Radiation in any of the windows could be monitored to supply the reference signal that in any of the water-vapor bands is the sensor water-vapor signal.

Accordingly, three narrow-wavelength bands satisfying the requirements for recovery of the first two terms of the \bar{N} equation could be centered at wavelengths of 1.22 μ , 1.32 μ , and 1.264 μ for the reference, water-vapor, and oxygen or dry-air density sampling bands, respectively. The water-vapor sampling band is displaced from the center to the wing of the strong 1.37 absorption band because, over any sort of range at all, virtually all the 1.37 radiation would be absorbed from an infrared beam and would leave no signal to effect the desired water-vapor measurement.

(B) Microwave absorption bands

In the microwave absorption spectrum (Figure 8) both oxygen and water vapor are evident absorbers. Water-vapor absorption is due to a pure rotational transition at 22.2 GHz (1.35 cm) and the nonresonant contribution of other rotational lines starting at around 180 GHz (0.166 cm) and extending well into the infrared (Reference 28). Oxygen absorption is due to a band of rotational transitions that start at about 53 GHz (0.57 cm) and extend to about 66 GHz (0.45 cm) (Reference 29). The dominance of the oxygen over the water-vapor absorption occurs because of the large density ratio of oxygen to water vapor, since the mass absorption coefficients of the two gases are of the same order of magnitude. If, however, the 20-GHz water-vapor band is selected as the sensing band for the third term in the \bar{N} -equation, the oxygen-absorption contribution to the received signal may be largely negated by referencing the 20GHz signal to a reference signal in the water-vapor window at 10 GHz. Note that oxygen absorption at these two frequencies differs in magnitude only slightly.

(3) Selection of sensing- and reference-band frequencies — cloudy-weather system

(A) Degradation of IR measurements in clouds

The hybrid system just described — the combination infrared and microwave active system — will provide the greatest accuracy in \bar{N}

measurement. For missile test range operations (characterized by (1) the availability of cooperative targets, and (2) conformance of test schedules to ideal weather conditions), this is the best approach to real-time measurement of \bar{N} .

The greatest drawback to the system is the inability of the specified infrared wavelengths to penetrate appreciable cloud depths. The scattering process is the dominant mechanism of extinction of infrared energy in clouds. Moreover, the radii of the drops that dominate the scattering and extinction characteristics of clouds are in the range of 5 to 20 μ (Reference 30). This means that the Mie scattering-area ratio appropriate to cloud drops can be approximated by its asymptotic value $K(a/\lambda) = \text{constant} = 2$ (Reference 30). The scattering coefficient for clouds can, therefore, be expressed as

$$\beta_{s_{\text{clouds}}} = 2 \pi a^2 n \quad (95)$$

where a is the median droplet radius, n the droplet-number concentration. The nonselective scattering coefficient implied by Equation 95, when applied to the scattering process in clouds, is confirmed by the fact that light extinction in clouds is shown experimentally to be virtually constant throughout the ultraviolet, visual, and near-infrared regions of the electromagnetic spectrum (Reference 30).

The two basic parameters required for estimating the extinction coefficients of clouds, cloud-droplet concentration and median droplet size, are functions both of cloud type and of cloud origin (Reference 31). In general, layer clouds (clouds of the genus "stratus") tend to have lower droplet concentrations than do the fair-weather convective-type (cumulus) clouds. The same relationship is true for clouds of maritime versus continental origin. This latter effect alone may result in a difference in droplet concentration by a factor of five in clouds of the same genera (Page 112 of Reference 31). A further generalization is that clouds with large droplet concentrations usually consist of small droplets, whereas those with small concentrations contain large drops. Thus, layer clouds contain droplets larger than those of the more active convective clouds, and droplets of the maritime clouds are larger than those of the continental clouds. This generalization is borne out by measurements (Reference 31).

High-altitude clouds, the cirrus clouds, and the tops of some cumulus clouds are composed of ice crystals. Natural ice crystals assume a variety of shapes (Reference 32). The predominant crystal form in high-altitude clouds is the hexagonal column, which is typically 500μ long with a length-to-breadth ratio varying from one to five. Although such ice crystals can hardly be considered spheres, scattering from long, circular cylinders (which should be similar to cloud ice crystal scattering) has been shown to be remarkably similar to that from spheres (Reference 30). The radius of the cylindrical cross section is the important dimension of the cylinders as far as scattering is concerned. Thus, within the limits of knowledge of the physics of ice clouds, Equation 95 may be applied to estimate the scattering coefficient of ice clouds as well as water clouds, if "a" is taken as the radius of the ice columns. The average value of the parameters required for the specification of cloud-scattering attenuation coefficients of various cloud types and for fog is summarized in Table 1.

Table 1: Cloud Particle Sizes and Number Densities

| <u>Cloud Type</u> | <u>Median Particle Concentration (cm^{-3})</u> | <u>Median Particle Radius (microns)</u> |
|----------------------|--|---|
| Fair-Weather Cumulus | 200 | 6 |
| Cumulus Congestus | 70 | 15 |
| Stratus | 80 | 9 |
| Cirrus | 5 | 30 |
| Fog | 10 | 25 |

According to Equation 95, the scattering attenuation coefficients applicable to the various cloud types, as specified by the parameter values given in Table 1, are as summarized in Table 2.

Table 2: Scattering Coefficients of Clouds

| <u>Cloud Type</u> | β_s <u>(km⁻¹ of cloud depth)</u> |
|----------------------|--|
| Fair-Weather Cumulus | 22.5 |
| Cumulus Congestus | 99.0 |
| Stratus | 40.5 |
| Cirrus | 28.2 |
| Fog | 42.4 |

The β_s -values summarized in Table 2 agree well with measured values obtained by Zabrodsii and Morachevskii (Reference 33). It must be remarked, however, that the β_s -values shown represent more or less "average" conditions; i.e., variations of plus or minus a factor of 10 from cloud to cloud on a day-to-day basis are the rule rather than the exception.

Defining an opaque cloud as one in which the transmittance is 0.01 or less, as suggested by Gates and Shaw (Reference 34), thicknesses of the above cloud types required to reduce transmittances to this point are shown in Table 3.

Table 3: Cloud Thicknesses Required For Transmittances Equal To 0.01

| <u>Cloud Type</u> | <u>Cloud Thickness (meters)</u> |
|----------------------|-------------------------------------|
| Fair-Weather Cumulus | 200 |
| Cumulus Congestus | 45 |
| Stratus | 115 |
| Cirrus | 165 |
| Fog | 110 |

The cloud thicknesses tabulated above represent nominal thicknesses. Cloud droplet size distributions and concentrations vary widely from day to day and from location to location, and so do the cloud thicknesses required for opacity. But despite this variation, it is still safe to say that any cloud will be likely to negate the performance of the infrared transmittance measurements of the hybrid, active system.

(3) Use of microwave frequencies in clouds

To extend the active-system capability to operation under cloudy conditions, microwave techniques must also be applied to the determination of the first two terms in the \bar{N} equation. The previously specified 22-GHz water-vapor band will suffice to determine the second term, and the first term may be recovered from transmittance measurements in the 60-GHz oxygen band (Figure 8). The 36-GHz window may be used as the reference for this latter measurement. However, in both these measurements ($\tau_{22\text{GHz}}$ for the f_{ω} term, $\tau_{60\text{GHz}}$ for the f_{ω_2} term) an uncertainty is introduced into the final estimate because the absorption coefficients at 22 and 60 GHz no longer exhibit the proper forms. That is, what is desired is the integrals of the oxygen and water-vapor partial densities alone, and not the integrals of the densities-to-temperature ratios.

But consider the integral

$$\int \frac{p_a}{T} ds$$

The equation of state relates partial density to pressure and temperature according to

$$p_a = \frac{M_a}{R^*} \cdot \frac{p}{T} \quad (96)$$

where M_a is the molecular weight of the absorbing specie, R^* is the universal gas constant. The hydrostatic equation further states that

$$\begin{aligned} dp &= -\rho g dz \\ &= -\frac{p_a}{\omega_a} g dz, \end{aligned} \quad (97)$$

where g is the acceleration of gravity, ω_a is the mixing ratio of the absorbing gas of partial density p_a . Finally, the differential path length element is related to the vertical element according to

$$ds = -f'(\epsilon) dz \quad (98)$$

where, for elevation angles, ϵ , greater than about 10 degrees, $f'(\epsilon)$ is very nearly equal to $\sec \epsilon$. At lower elevation angles, $f'(\epsilon)$ takes on a greater

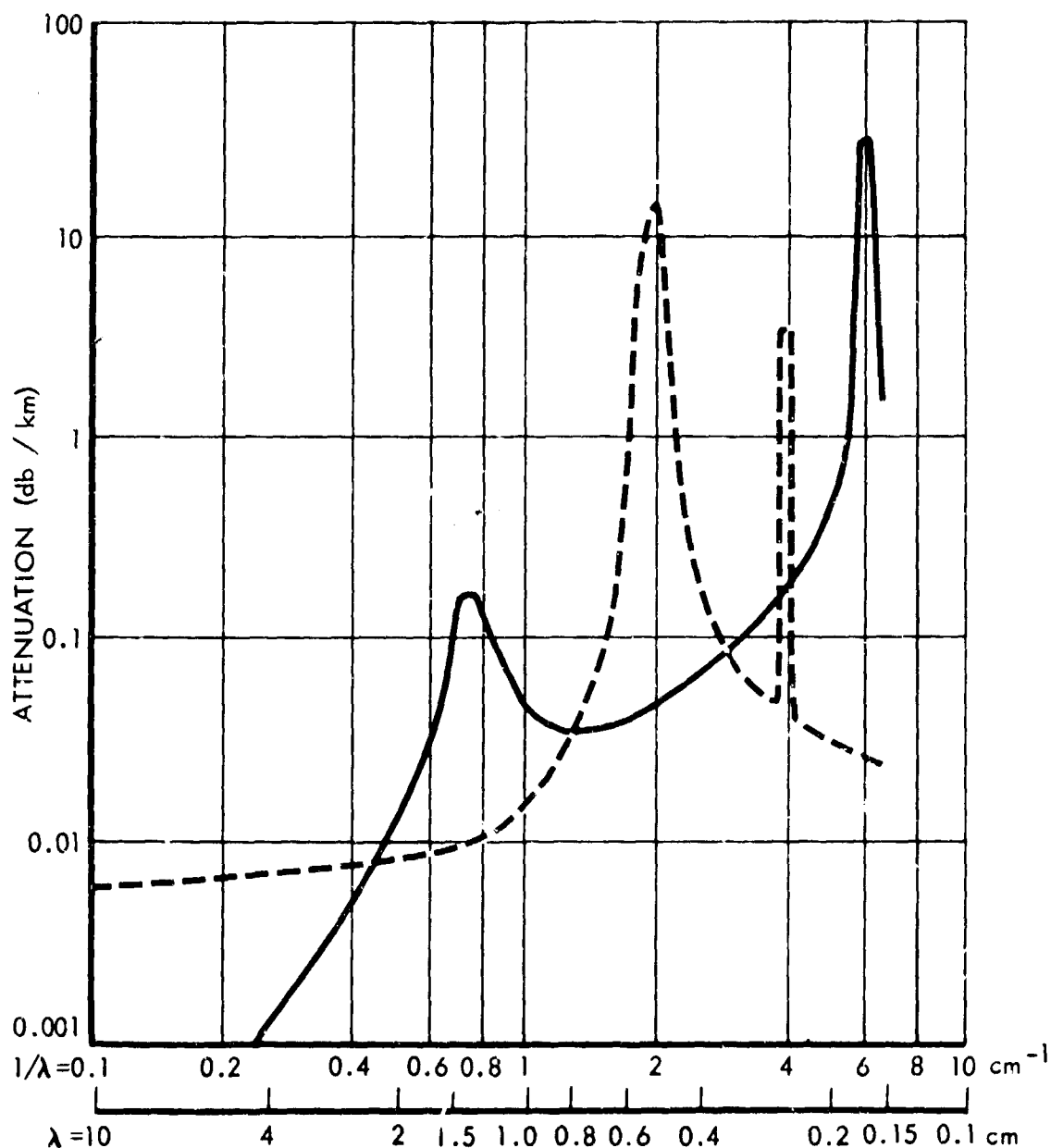


Figure 8: THEORETICAL VALUES OF ATMOSPHERIC ATTENUATION BY OXYGEN AND UNCONDENSED WATER VAPOR AT SEA LEVEL FOR A TEMPERATURE OF 20°C. THE SOLID CURVE GIVES THE ATTENUATION BY WATER IN AN ATMOSPHERE CONTAINING 1-PERCENT WATER MOLECULES ($p=7.5 \text{ g/m}^3$). THE DASHED CURVE IS THE ATTENUATION BY OXYGEN (REFERENCE 24).

complexity due to the curvature of the Earth. Equation 98 into Equation 97 and division of both sides of the equation by T yields

$$\frac{\rho_a}{T} ds = - \frac{w_a f(\epsilon)}{g} \cdot \frac{dp}{T} \quad (99)$$

Integrating appropriately,

$$\int_0^S \frac{\rho_a}{T} ds = - \frac{w_a f(\epsilon)}{g} \int_{p_0}^{p_s} \frac{dp}{T} \quad (100)$$

The integrations are to be performed from the point $S = 0$ (where the pressure is p_0) to the point S (where the pressure is p_s).

If the reciprocal of temperature as defined by Equation 96 is now substituted into the right-hand side of Equation 100, then

$$- \frac{w_a f(\epsilon)}{g} \int_{p_0}^{p_s} \frac{dp}{T} = \frac{w_a f(\epsilon)}{g} \cdot \frac{R^*}{M_a} \int_{p_0}^{p_s} \rho_a d(\ln p) \quad (101)$$

The law of the mean states that

$$\begin{aligned} \langle \rho_a \rangle &= \frac{\int_{p_0}^{p_s} \rho_a d(\ln p)}{\int_{p_0}^{p_s} d(\ln p)} \\ &= \frac{\int_0^{z_s} \rho_a dz}{\int_0^{z_s} dz} \end{aligned} \quad (102)$$

where the brackets denote the average value. Therefore,

$$\int_{p_0}^{p_s} \rho_a d(\ln p) = \frac{\ln\left(\frac{p_s}{p_0}\right)}{(z_s - z_0)} \int_0^{z_s} \rho_a dz \quad (103)$$

The integral on the right-hand side of Equation 103 is that of the right-hand side

Equation 101:

$$\int_0^{z_s} \rho_a dz = - \frac{w_a}{g} \int_{p_0}^{p_s} dp \quad (104)$$

$$= \frac{w_a}{g} (p_0 - p_s)$$

The term $(z_s - z_c)$ in Equation 103 can be found by the method used in meteorology to find pressure altitude. This involves: (1) substitution for density from Equation 96 into Equation 97, and (2) assuming linearity in temperature so that the mean value can be moved through the integral. Thus,

$$\frac{dp}{\rho} = - \frac{g}{w_a} \frac{M_a}{R^*} \cdot \frac{1}{\langle T \rangle} \int_{z_c}^{z_s} dz \quad (105)$$

and, therefore,

$$(z_s - z_c) = \frac{w_a R^*}{g M_a} \cdot \langle T \rangle \ln \left(\frac{p_c}{p_s} \right) \quad (106)$$

Equation 106 into Equation 103 then yields

$$\int_{p_0}^{p_s} \rho_a d(\ln p) = \frac{g M_a \ln \left(\frac{p_s}{p_c} \right)}{w_a R^* \langle T \rangle \ln \left(\frac{p_s}{p_c} \right)} \int_0^{z_s} \rho_a dz$$

$$= \frac{M_a}{w_a R^*} \cdot \frac{g}{\langle T \rangle} \int_0^{z_s} \rho_a dz \quad (107)$$

From Equation 101, it therefore follows that

$$\frac{1}{\langle T \rangle} \int_{z_c}^{z_s} \rho_a dz = - \frac{w_a f(\epsilon)}{g} \int_{p_0}^{p_s} \frac{dp}{T} \quad (108)$$

The right-hand side of Equation 108 is precisely the right-hand side of Equation 100. Therefore,

$$\int_0^s \frac{\rho_a}{T} ds = \frac{1}{\langle T \rangle} \int_{z_c}^{z_s} \rho_a dz, \quad (109)$$

or, from Equation 93,

$$\int_0^S \frac{\rho_a}{T} ds = \frac{1}{\langle T \rangle f(\epsilon)} \int_0^S \rho_a ds \quad (110)$$

At first glance, the rather elaborate derivation just presented seems almost superfluous because the final result (Equation 110) seems almost obvious. However, the "mean" temperature must be carefully defined to permit its removal from the integral of the microwave absorption coefficient. Specifically, the mean must be taken with respect to the natural logarithm of pressure.

Nevertheless, on the basis of Equation 110, Equation 81 permits the statements that

$$\int_0^S \rho_{O_2} ds = \langle T \rangle \cdot G(I_{60 \text{ GHz}}) \quad (111)$$

and

$$\int_0^S \rho_w ds = \langle T \rangle G(I_{22 \text{ GHz}}) \quad (112)$$

where the angled brackets now denote the mean process. It is on the basis of the above equations that \bar{N} can be specified completely in terms of microwave transmittance measurements. The additional uncertainty (above that attainable from infrared measurements) enters because of the need to estimate the additional parameter $\langle T \rangle$. Auxiliary meteorological data (radiosondes) are thus required to complete the \bar{N} specification.

B. Passive \bar{N} -measurement system

Lacking cooperative targets, the requirement is for the passive \bar{N} -measurement system. The integral of the absorption coefficient is recovered from the inversion of the second term on the right-hand side of the radiative transfer equation (Equation 59). In this case, I_ν represents the intensity of the thermal radiation incident on a radiometer (a sensitive radiation thermometer) that originates in the atmosphere itself. Because the spectral radiance of such emitted energy is as dictated by Planck's black-or-gray-body radiation law, the temperatures typical of the atmosphere dictate that the greater contribution comes from

the lower frequency (longer wavelength) radiation. In fact, emitted energies are negligible at the active-system infrared wavelengths previously specified. Therefore, to ensure measurable signals and to provide the greatest degree of all-weather capability, consideration should be given to developing a passive \bar{N} -measurement system operating at the microwave frequencies in the absorption bands previously specified.

(1) Total absorption versus frequency

Because of the finite widths and pressure-broadened line shapes of atmospheric constituent absorption bands, the total (total throughout the depth of the atmosphere) integrated absorption changes rapidly with frequency as the frequency is scanned from regions outside the band to the resonant-band frequency. For example, for frequencies near the center of the 60-GHz oxygen band, the absorption is nearly complete. In the frequency region from 55 to 50 GHz, the absorption decreases as the frequency decreases and approaches the wings of the band. Because of the basic connection at any frequency between absorption and emissivity, this effect can be seen in the plot of brightness temperature versus frequency shown in Figure 9. Brightness temperature is related to I_ν according to

$$T_{B_\nu} = \frac{c^2}{2k\nu^2} I_\nu \quad (113)$$

Near the center of the band the atmosphere is essentially a blackbody radiating at a temperature nearly equal to that at the surface of the Earth. Over the relatively small frequency interval from 55 to 50 GHz, a brightness change of about 150°K takes place, and, in the steepest portion of the curve, the slope is about 60°K per GHz. The data contained in Figure 9 were calculated, according to Van Vleck's oxygen-absorption coefficient from actual radiosonde data obtained at Dakar, Senegal (Reference 27). Similar calculations based on Gutnick's mean midlatitude water-vapor profile (Reference 35) as applied to a standard atmosphere are shown in Figure 10. Note again, the rapid change in brightness temperature in the interval of 16 to 22 GHz. The slope at the steepest part of the curve is about 15°K per GHz. The difference in shapes of the curves shown in

the lower frequency (longer wavelength) radiation. In fact, emitted energies are negligible at the active-system infrared wavelengths previously specified. Therefore, to ensure measurable signals and to provide the greatest degree of all-weather capability, consideration should be given to developing a passive \bar{N} -measurement system operating at the microwave frequencies in the absorption bands previously specified.

(1) Total absorption versus frequency

Because of the finite widths and pressure-broadened line shapes of atmospheric constituent absorption bands, the total (total throughout the depth of the atmosphere) integrated absorption changes rapidly with frequency as the frequency is scanned from regions outside the band to the resonant-band frequency. For example, for frequencies near the center of the 60-GHz oxygen band, the absorption is nearly complete. In the frequency region from 55 to 50 GHz, the absorption decreases as the frequency decreases and approaches the wings of the band. Because of the basic connection at any frequency between absorption and emissivity, this effect can be seen in the plot of brightness temperature versus frequency shown in Figure 9. Brightness temperature is related to I_ν according to

$$T_{B_\nu} = \frac{c^2}{2k\nu^2} I_\nu \quad (113)$$

Near the center of the band the atmosphere is essentially a blackbody radiating at a temperature nearly equal to that at the surface of the Earth. Over the relatively small frequency interval from 55 to 50 GHz, a brightness change of about 150°K takes place, and, in the steepest portion of the curve, the slope is about 60°K per GHz. The data contained in Figure 9 were calculated, according to Van Vleck's oxygen-absorption coefficient from actual radiosonde data obtained at Dakar, Senegal (Reference 27). Similar calculations based on Gutnick's mean midlatitude water-vapor profile (Reference 35) as applied to a standard atmosphere are shown in Figure 10. Note again, the rapid change in brightness temperature in the interval of 16 to 22 GHz. The slope at the steepest part of the curve is about 15°K per GHz. The difference in shapes of the curves shown in

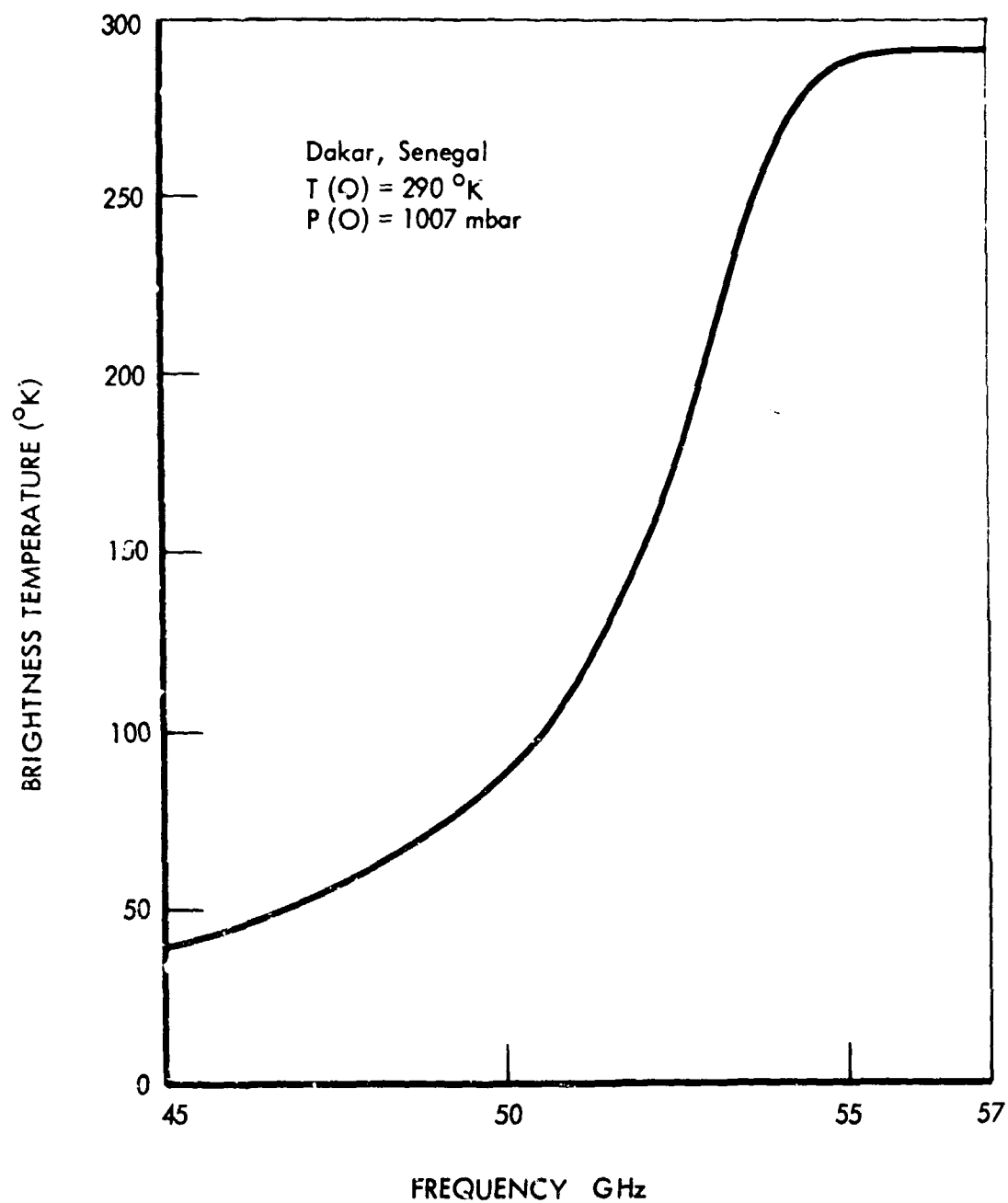


Figure 9: BRIGHTNESS TEMPERATURE VERSUS FREQUENCY
FOR A VERTICAL ANTENNA—After Westwater, 1965

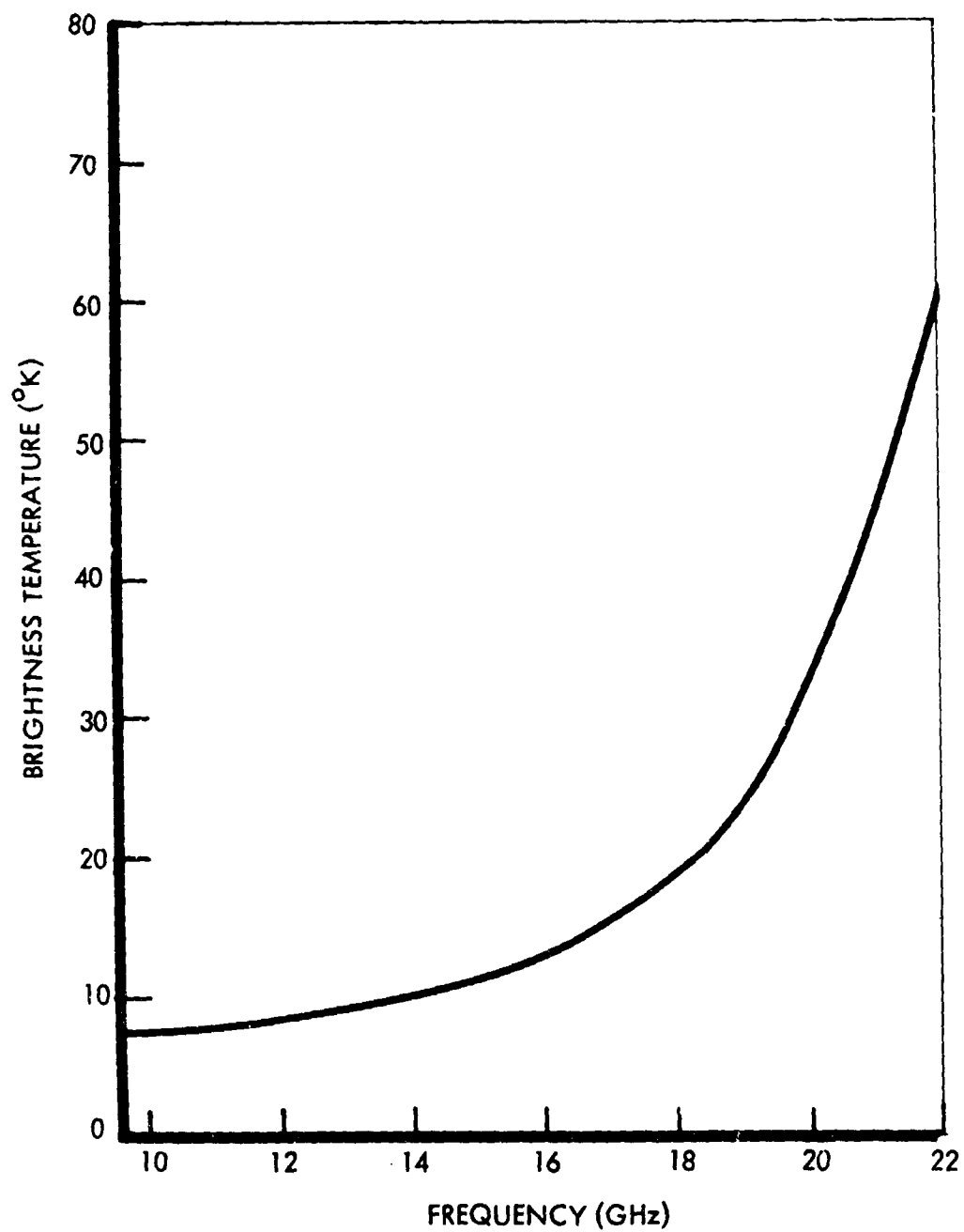


Figure 10: BRIGHTNESS TEMPERATURE AS A FUNCTION OF FREQUENCY
IN THE 22 GHz WATER-VAPOR BAND

Figures 9 and 10 are attributable to the different pressure broadening effects active at the different frequencies.

The suggestion is therefore immediate that these portions of the oxygen and water-vapor spectra may be useful for a ground-based passive probe of the lower atmosphere for these two constituents. This is so because the large changes in brightness temperature over the indicated frequency intervals satisfy the dominant requirement for ground-based remote probing systems; i.e., the changes in the T_B 's with frequency are large enough to permit a nondegenerate set of equations to be obtained for inverting the brightness-temperature-versus-frequency curve to determine the temperature-height and water-vapor-height profiles of the lower atmosphere.

(2) Inversion of the radiation-transfer equation

In terms of the brightness temperature observed when looking up into the atmosphere, the radiative-transfer equation (Equation 59) for the passive mode ($I_{\nu_0} = 0$) is (Reference 36)

$$T_{B\nu} = \int_0^\infty T(s) \alpha_\nu(s, T(s)) e^{-\int_0^s \alpha_\nu(s', T(s')) ds'} ds \quad (114)$$

where T_B is the brightness temperature, T the absolute temperature, and α_ν can be either the oxygen or water-vapor absorption coefficient. Equation 114 is nonlinear and difficult to solve because the absorption coefficient that occurs in the Kernel is a function of path through its dependence on temperature. At a single frequency, an infinite number of temperature profiles exist, $T(s)$, so that the same intensity of radiation is given at the top or bottom of the atmosphere. Thus, the recovery of a unique distribution will require a set of integral equations; as usual, the requirement is for n equations to define n variables in the atmospheric representation.

A description of the atmosphere under this requirement has been attempted in various ways. Because a set of equations like Equation 114 is mathematically unstable (Reference 37), other approaches must be tried. One such approach has been to represent $T(s)$ by some particular analytic function and then

to use techniques based on the technique of Lagrangian multipliers, such as a least-squares fit (Reference 38), in an iterative solution. Some examples of functions that have been used are: (1) truncated algebraic and trigonometric series (References 39 and 40), (2) exponential (Reference 41), and (3) Tschebyscheff polynomials (Reference 27). Thus, in an algebraic function, the series

$$T = A_0 + A_1 z + A_2 z^2 + A_3 z^3 + \dots \quad (115a)$$

would be substituted into Equation 114, and the coefficients $A_0, A_1, A_2, A_3, \dots$ would be determined. Similarly, for the trigonometric series:

$$T = A_0 + A_1 \sin z + A_2 \sin 2z + \dots \quad (115b)$$

for Tschebyscheff polynomials:

$$T = A_0 + A_1 T_{(1)}(z) + A_2 T_{(2)}(z) + \dots \quad (115c)$$

The accuracy of replication of the atmospheric temperature structure is limited by the number of terms in the series expansion and the complexity of the atmospheric structure. For example, a simple atmosphere with a constant lapse rate can easily be represented by the first two terms in Equation 115a:

$$T(z) = T_0 + A_1 z$$

Here, A_1 can be identified with the lapse rate of temperature, whereas T_0 is the ground temperature.

When the atmospheric structure is more complex, a larger number of terms must be used in the series. This leads to the requirements for a large number of measurements.

(A) Oxygen profile

From Equation 66b, the oxygen microwave absorption coefficient can be expressed as a function of pressure, temperature, and frequency as follows:

$$\alpha_{O_2}(z, p, T) = \frac{C_1 p z^2}{T^3} \sum_{\substack{N_{\alpha k}=1 \\ \nu_N \pm \text{Resonant}}}^{45} S_N \exp(-E_N / kT) \quad (116)$$

The terms can be defined as

$$c_j = 1.8573 \text{ db/km}$$

$$= .50641 \text{ nepers/km}$$

for concentrations of oxygen in the atmosphere. T is the absolute temperature in degrees Kelvin, p is pressure in millibars, and ν is the frequency in GHz. The summation is to be performed for the odd integers from 1 to 45. For each integer there are two associated resonant frequencies (Table 4).

Table 4: Resonant Oxygen-Transition Frequencies

| <u>N</u> | <u>N+, GHz</u> | <u>N-, GHz</u> |
|----------|----------------|----------------|
| 1 | 56.2648 | 118.7505 |
| 3 | 58.4466 | 62.4863 |
| 5 | 59.5910 | 60.3061 |
| 7 | 60.4348 | 59.1642 |
| 9 | 61.1506 | 58.3239 |
| 11 | 61.8002 | 57.6125 |
| 13 | 62.4112 | 56.9682 |
| 15 | 62.9980 | 56.3634 |
| 17 | 63.5685 | 55.7839 |
| 19 | 64.1272 | 55.2214 |
| 21 | 64.6779 | 54.6728 |
| 23 | 65.2240 | 54.1294 |
| 25 | 65.7626 | 53.5960 |
| 27 | 66.2978 | 53.0695 |
| 29 | 66.8313 | 52.5458 |
| 31 | 67.3627 | 52.0259 |
| 33 | 67.8923 | 51.5091 |
| 35 | 68.4205 | 50.9949 |
| 37 | 68.9478 | 50.4830 |
| 39 | 69.4741 | 49.9730 |
| 41 | 70.0000 | 49.4648 |
| 43 | 70.5249 | 48.9582 |
| 45 | 71.0497 | 48.4530 |

These resonant frequencies, first predicted by Van Vleck, were subsequently measured up to N = 25. At each integer quantum number, the resonant frequencies have been calculated up to N = 45 by Miller and Townes (Reference 42) and by Tsao and Curnutte, (Reference 43). Excellent agreement has been observed between the calculated and observed resonant frequencies. For example,

the standard deviation of the difference between the observed and calculated frequencies for Zumnerer and Mizushima's work is 1.35×10^{-3} GHz out of approximately 60 GHz (Reference 29).

The term S_N (consisting of terms involving $\Delta\nu$, the line width parameter, the magnetic dipole moment of the Nth transition, and the structure function shown in Equation 66b) is given by

$$S_N = F_{N+} \mu_{N+}^2 + F_{N-} \mu_{N-}^2 + F_0 \mu_{N0}^2 \quad a)$$

$$F_{N+} = \frac{\Delta\nu}{(\nu_{N+} - \nu)^2 + \Delta\nu^2} + \frac{\Delta\nu}{(\nu_{N+} + \nu)^2 + \Delta\nu^2} \quad b)$$

$$F_{N-} = \frac{\Delta\nu}{(\nu_{N-} - \nu)^2 + \Delta\nu^2} + \frac{\Delta\nu}{(\nu_{N-} + \nu)^2 + \Delta\nu^2} \quad c)$$

$$F_0 = \frac{\Delta\nu}{\nu^2 + \Delta\nu^2} \quad d)$$

$$\mu_{N+}^2 = \frac{N(2N+3)}{N+1} \quad e)$$

$$\mu_{N-}^2 = \frac{(N+1)(2N-1)}{N} \quad f)$$

$$\mu_{N0}^2 = \frac{2(N^2 + N + 1)(2N + 1)}{N(N+1)} \quad g)$$

The line-width factor, $\Delta\nu$, is generally assumed to be proportional to pressure and temperature. Meeks and Lilley (Reference 44) give an expression:

$$\Delta\nu(p, T) = a p [0.21 + 0.78b] \left(\frac{300}{T}\right)^{0.85} \quad (118)$$

where a and b are constants. The factors 0.21 and 0.78 will be recognized as the percents by volume of oxygen and nitrogen in the atmosphere. The constant a is approximately 1.4628 MHz per mb. The "constant" b apparently has two values: In the high-pressure range at pressures greater than 350 millibars, $b = 0.25$; at pressures less than 25 millibars, $b = 0.75$. Between these two pressures there is a region of uncertainty, which Meeks and Lilley have covered by letting

$$b = 0.25 + 0.50 \left(\frac{h - H_1}{H_2 - H_1} \right) \quad (119)$$

where h is the altitude of computation, H_1 is the pressure altitude of 350 millibars, and H_2 is the pressure altitude of 25 millibars. Other effects, such as Zeeman-splitting and Doppler-broadening, occur above 30 km (10mb).

Since the recovery of information about the atmospheric structure remotely depends on knowledge of $\Delta\nu$, its precise definition is a matter of some importance. The simplest method of accurately determining the a and b parameters would be with concurrent radiosonde-radiometer measurements.

Polynomial approximations to the atmosphere's vertical structure are limited in accuracy. Westwater and Abbott (Reference 41) have given some errors that can be associated with application of such function to the inversion of Equation 114. Five iterations were used in fitting varying-degree polynomials to T_B data obtained at 12 measuring frequencies. Profile errors associated with polynomial degree are given in Table 5.

Table 5: Errors in Profile Parameters
Versus Polynomial Degree

| Polynomial Degree | RMS Error (T , °K) | RMS Error (p , mb (fixed height)) |
|----------------------|--------------------------|---|
| 3 | 6 | 3.6 |
| 4 | 4.2 | 1.7 |
| 5 | 2.2 | -0.5 |

A further difficulty results when finite random-brightness-temperature-measurement errors are introduced. The presence of such errors: (1) limits the number of terms in the series of expansion, and (2) introduces inaccuracies in the derived temperature. Figure 11 is from Westwater and Abbott's error analysis, in which deviations of constant magnitude were added to the postulated measured T_B 's.

The actual deviation shown in Figure 12 for brightness-temperature errors of 0°K, $\pm 1.25^\circ\text{K}$, and $\pm 2.0^\circ\text{K}$ are more instructive as to the actual mathematical processes. In terms of pressure coordinates, the differential equation that generates Equation 114 can be expressed as

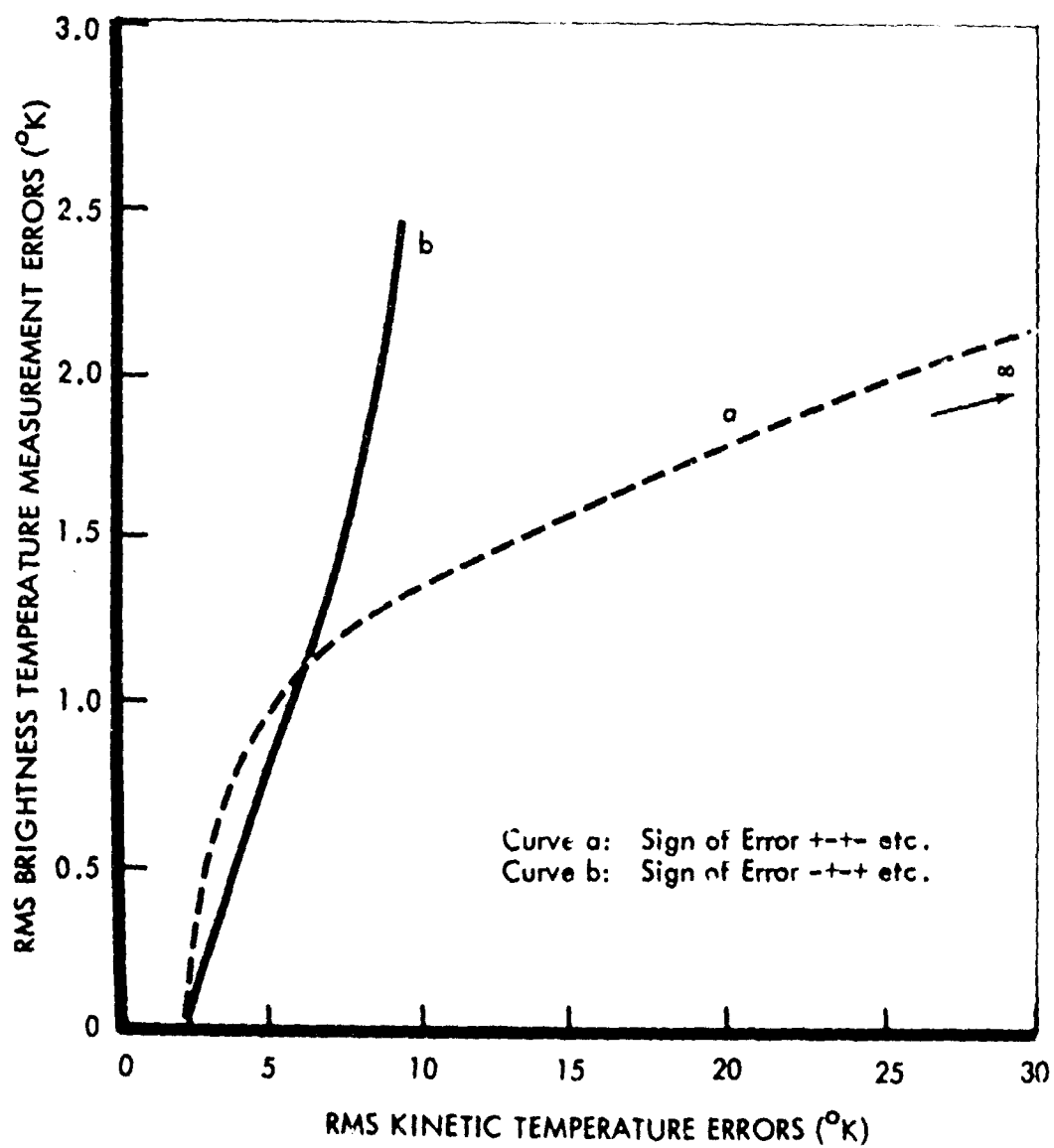


Figure 11: RMS ERROR IN KINETIC TEMPERATURE IN THE LAYER 0-10 km AS RELATED TO RMS MEASUREMENT ERRORS IN BRIGHTNESS TEMPERATURE

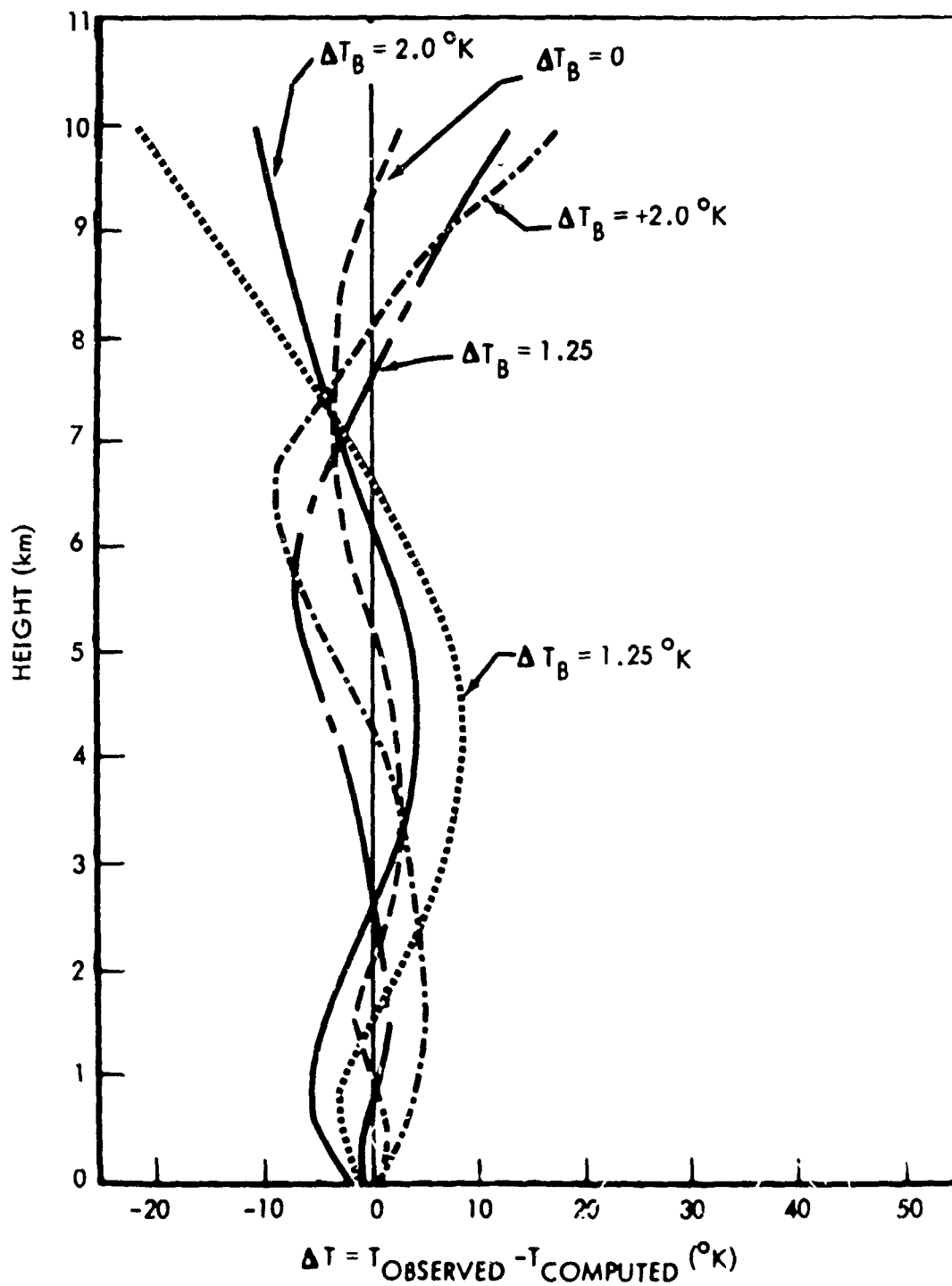


Figure 12: DEVIATION OF CALCULATED TEMPERATURE PROFILE FROM TRUE PROFILE FOR VARIOUS ALTERNATING ERRORS IN BRIGHTNESS TEMPERATURE

$$\frac{dT_B}{dp} - \frac{R\alpha(p, T, \nu)}{gP} T T_B = -\frac{R}{g} \frac{\alpha(p, T, \nu)}{P} T^2 \quad (120)$$

If it is assumed that T is some function of p , then Equation 120 is a Riccati differential equation (Reference 45), which is difficult to solve. Each Riccati-type differential equation generates a different class of functions as its solution. The most-studied Riccati equations are those that generate such functions as exponential, hyperbolic, circular, Legendrian, and Hermitian types as their solution.

Most of these functions are periodic or nearly periodic. It is likely that the quasiperiodic residual errors of Westwater and Abbott's results shown in Figure 12 are the result of remainder terms. These residuals are the difference between the 4th-degree polynomial approximation and the true function that was implicitly generated by assuming a functional relation between pressure and temperature of the form

$$T = k p^r$$

where k is a constant and r is a variable exponent.

To avoid the difficulties associated with a functional representation of the atmosphere, the model shown in Figure 13 was developed. This model postulates that the atmosphere can be divided into $(n-1)$ pressure layers that may vary in thickness, where n is an as yet undetermined number. Each layer is to be sufficiently small so that the "mean" thermodynamic temperature as defined in Equation 106 can be used in Equation 120 to give the brightness temperature at the bottom of the layer with arbitrary precision as compared to that computed from any meteorologically realizable temperature-pressure distribution.

Under this restriction, the temperature variable in Equation 120 becomes a constant. Terms can be rearranged and integrated for the layer bounded by pressures, (p_n, p_{n-1}) for which there are corresponding brightness temperatures $(T_{B,n}, T_{B,n-1})$

$$\int_{T_{B,n-1}}^{T_{B,n}} \frac{dT_B}{\langle T_{n,n-1} \rangle - T_B} = -\frac{RC_p \nu^2}{g \langle T_{n,n-1} \rangle^2} \int_{p_{n-1}}^{p_n} S_N \exp \frac{-E_N}{h \langle T_{n,n-1} \rangle} dp \quad (121)$$

The left-hand side of Equation 121 can be integrated immediately to give

$$\frac{\langle T_{n,n-1} \rangle - T_{B,n-1}}{\langle T_{n,n-1} \rangle - T_{B,n}} = \exp \left[\frac{RC_1 v^2}{j \langle T_{n,n-1} \rangle} \int_{F_{n-1}}^{F_n} \sum S_N \exp \left(\frac{-E_n}{k \langle T_{n,n-1} \rangle} \right) dp \right] \quad (122)$$

The integral equation (121) may also be expressed in closed form for pressures less than 350 millibars, where b is a constant (see Equation 119), since Δv given by Equation 118 can be expressed as an integrable function of pressure and the mean temperature. For example, consider the term F_{N+} (Equation 117b) that is one of the terms that make up S_N . For simplicity, let

$$\Delta v' = a (0.21 + 0.78b) \left(\frac{300}{\langle T_{n,n-1} \rangle} \right)^{0.85} \quad (123)$$

The integral can be evaluated directly to give

$$\int_{F_{n-1}}^{F_n} \frac{\Delta v' p}{(x_{N+} - x)^2 + (\Delta v' p)^2} + \frac{\Delta v' p}{(x_{N+} + x)^2 + (\Delta v' p)^2} dp = \frac{1}{2 \Delta v'} \ln \left\{ \frac{[(x_{N+} - x)^2 + (\Delta v' p_n)^2][x_{N+}^2 + (\Delta v' p_n)^2]}{[x_{N+} - x)^2 + (\Delta v' p_{n-1})^2][x_{N+}^2 + (\Delta v' p_{n-1})^2]} \right\} \quad (124)$$

$$= f_{N^+}(n, n-1) \quad (125a)$$

Similar integrations can be performed on the terms F_N (Equations 117c and 117d). Let them be

$$\int_{F_{n-1}}^{F_n} F_{N-} dp = f_{N^-}(n, n-1) \quad (125b)$$

$$\int_{F_{n-1}}^{F_n} F_0 dp = f_0(n, n-1) \quad (125c)$$

The bracketed term on the right-hand side of Equation 122 can then be expressed as the logarithm of a product that, since it is an exponential function, becomes just the product of the argument: i.e.,

$$\prod_{\substack{N_{\text{coll}}=1 \\ \text{valid Resonant}}}^{\infty} \left\{ f_{N_{(n,n-1)}} f_{N_{(n,n-1)}} f_{O_{(n,n-1)}} \right\}^{\frac{RC_{1,2}^2}{9\langle T_{n,n-1} \rangle^2} \exp \frac{-E_N}{h\langle T_{n,n-1} \rangle}} \quad (126)$$

$$= a_{n,n-1}$$

The expression for the brightness temperature on one side of a layer at a given frequency, in terms of the brightness temperature on the other side, and the absorption function $a_{n,n-1}$ at the mean temperature of the layer can be found by combining Equations 126 and 122 to give

$$\frac{\langle T_{n,n-1} \rangle - T_{B,n-1}}{\langle T_{n,n-1} \rangle - T_{B,n}} = a_{n,n-1} \quad (127a)$$

Note that $a_{n,n-1}$ in the above equation is "basically" the parameter desired for estimation of the contribution of oxygen to line-integrated refractivity. That is, $a_{n,n-1}$ represents the exponential of the integral of the oxygen absorption coefficient between levels n and $n-1$, where the pressures are p_n and p_{n-1} .

The nomenclature of Equation 127 may be illustrated from Figure 13, the radiative transfer model. For instance, if $n = 2$, then Equation 127 is

$$\frac{\langle T_{2,1} \rangle - T_{B,1}}{\langle T_{2,1} \rangle - T_{B,2}} = a_{2,1} \quad (127b)$$

The single subscript refers to a specified pressure; for instance, p_1 is the surface pressure and p_2 is the second pressure. Similarly $T_{B,1}$ and $T_{B,2}$ are the brightness temperatures at pressures p_1 and p_2 . The double subscript refers to the characteristics of a whole layer. For example, $T_{2,1}$ and $a_{2,1}$ are respectively the mean temperature and the absorption function bounded by pressures p_1 and p_2 .

The pressure interval ($p_n - p_{n-1}$) over which the integration is valid has been ascertained by using five meteorologically realistic atmospheres.

$$\prod_{N_{\text{odd}}=1}^{45} \left\{ f_{N^+_{(n,n-1)}} f_{N^-_{(n,n-1)}} f_{O_{(n,n-1)}} \right\}^{\frac{RC_{12}^2}{k \langle T_{n,n-1} \rangle^2} \exp \frac{-E_N}{k \langle T_{n,n-1} \rangle}} \quad (126)$$

$$= a_{n,n-1}$$

The expression for the brightness temperature on one side of a layer at a given frequency, in terms of the brightness temperature on the other side, and the absorption function $a_{n,n-1}$ at the mean temperature of the layer can be found by combining Equations 126 and 122 to give

$$\frac{\langle T_{n,n-1} \rangle - T_{B,n-1}}{\langle T_{n,n-1} \rangle - T_{B,n}} = a_{n,n-1} \quad (127a)$$

Note that $a_{n,n-1}$ in the above equation is "basically" the parameter desired for estimation of the contribution of oxygen to line-integrated refractivity. That is, $a_{n,n-1}$ represents the exponential of the integral of the oxygen absorption coefficient between levels n and $n-1$, where the pressures are p_n and p_{n-1} .

The nomenclature of Equation 127 may be illustrated from Figure 13, the radiative transfer model. For instance, if $n = 2$, then Equation 127 is

$$\frac{\langle T_{2,1} \rangle - T_{B,1}}{\langle T_{2,1} \rangle - T_{B,2}} = a_{2,1} \quad (127b)$$

The single subscript refers to a specified pressure; for instance, p_1 is the surface pressure and p_2 is the second pressure. Similarly $T_{B,1}$ and $T_{B,2}$ are the brightness temperatures at pressures p_1 and p_2 . The double subscript refers to the characteristics of a whole layer. For example, $T_{2,1}$ and $a_{2,1}$ are respectively the mean temperature and the absorption function bounded by pressures p_1 and p_2 .

The pressure interval ($p_n - p_{n-1}$) over which the integration is valid has been ascertained by using five meteorologically realistic atmospheres.

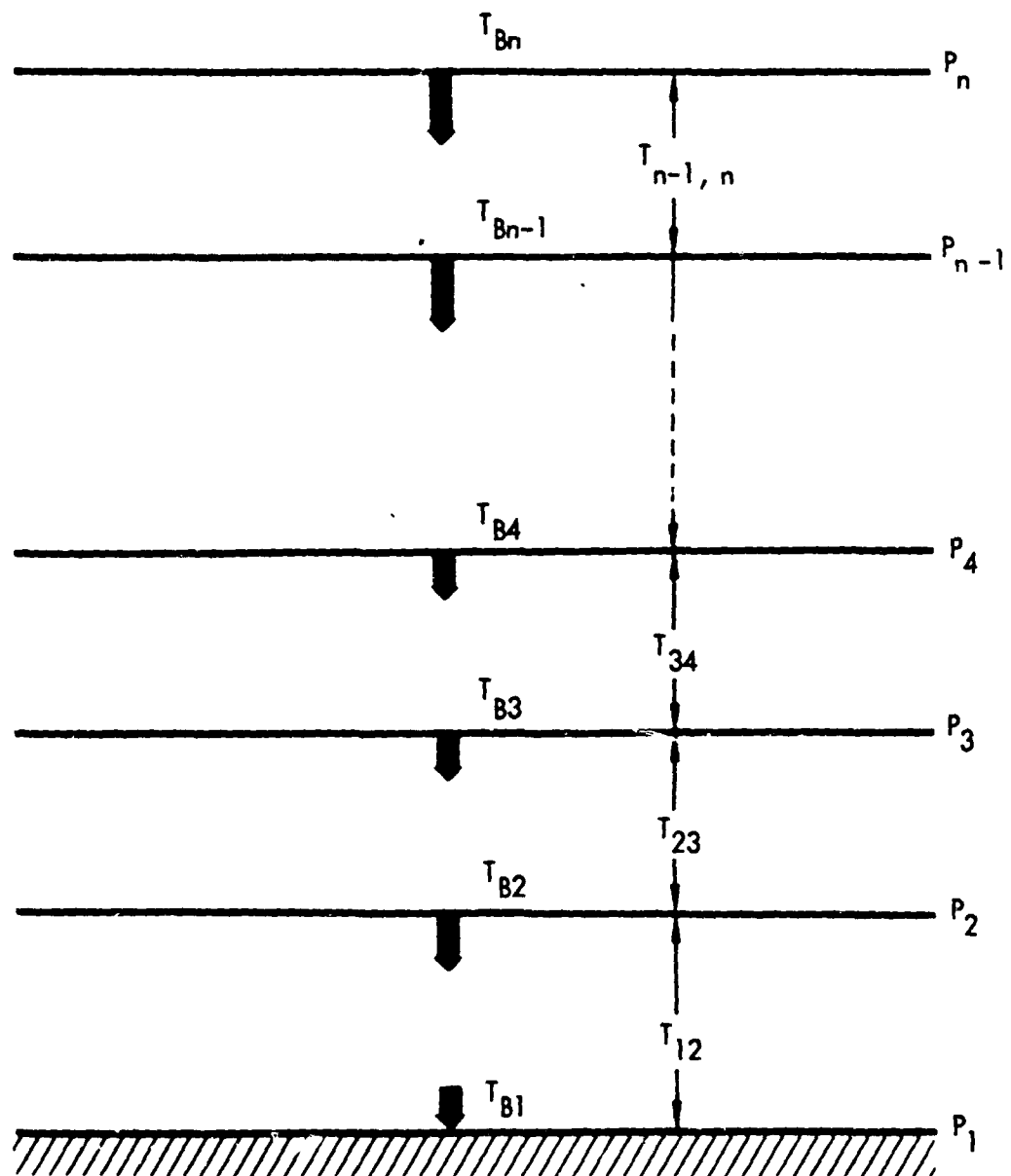


Figure 13: RADIATIVE-TRANSFER MODEL

The comparison was made by calculating the brightness temperatures from Equation 121 in a standard computer routine with those calculated from Equation 127. The calculations from Equation 121 were based on a Runge-Kutta variable step solution to the differential equation. The steps varied from 10^{-3} millibar to 1 millibar. It was found that the T_B could be calculated with an error less than 0.25°K for pressure increments of 300 millibars or less. These calculations were restricted to frequencies for which the absorption and emission above 300 millibars was negligible to eliminate the problem of the variable b (Equation 119). This problem could be obviated by stepwise integration of the integral equation (122) to compute the absorption functions directly. For purposes of later computations, however, the partial derivative of $a_{n, n-1}$ with respect to $T_{n, n-1}$ is required, and it was desirable to perform the integration. Further, profiling to 300 millibars was apparently as high as was feasible, because of the masking by the absorption in the atmosphere below 300 millibars of the radiation from levels above this pressure. This results in a great loss of sensitivity.

The absorption function for various mean temperatures is shown in Figures 14, 15 and 16. These data, in conjunction with measured brightness temperatures, permit recovery of integrated oxygen-absorption coefficients. The method is as follows (illustrated for a three-layer atmosphere; the number of layers is determined by the number of operating radiometer frequencies).

At a given frequency, the brightness temperature at the bottom of any layer can be expressed, from Equation 127 in terms of brightness temperature at the top of the layer, the mean temperature through the layer, and the absorption function through the layer. For a three-layer atmosphere, the three equations required to do so are

$$T_{B,3} = \langle T_{4,3} \rangle [1 - (a_{4,3})] + (a_{4,3}) T_{B,4} \quad a)$$

$$T_{B,2} = \langle T_{3,2} \rangle [1 - (a_{3,2})] + (a_{3,2}) T_{B,3} \quad b) \quad (128)$$

$$T_{B,1} = \langle T_{2,1} \rangle [1 - (a_{2,1})] + (a_{2,1}) T_{B,2} \quad c)$$

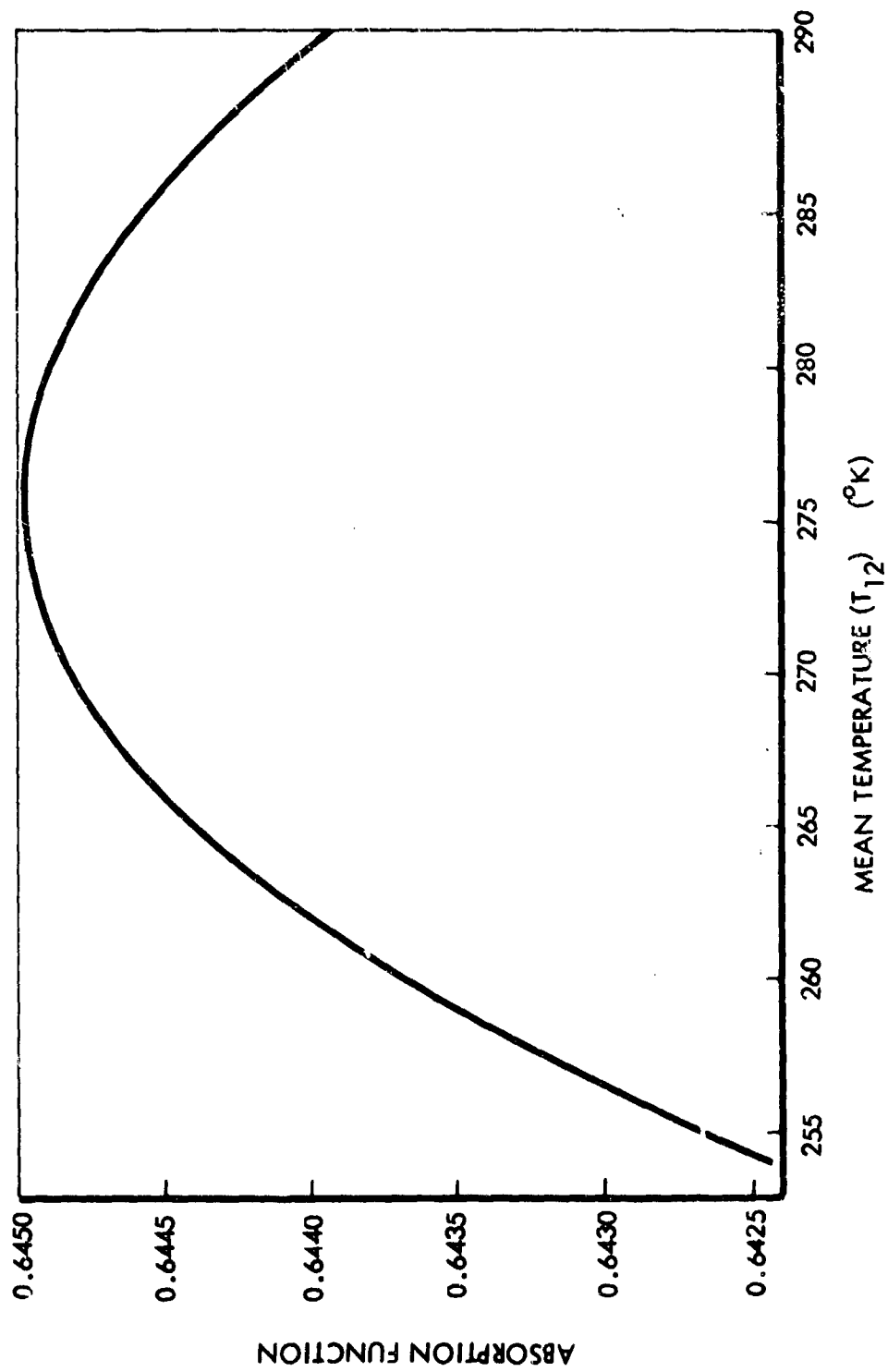


Figure 14: ABSORPTION FUNCTION VERSUS MEAN TEMPERATURE

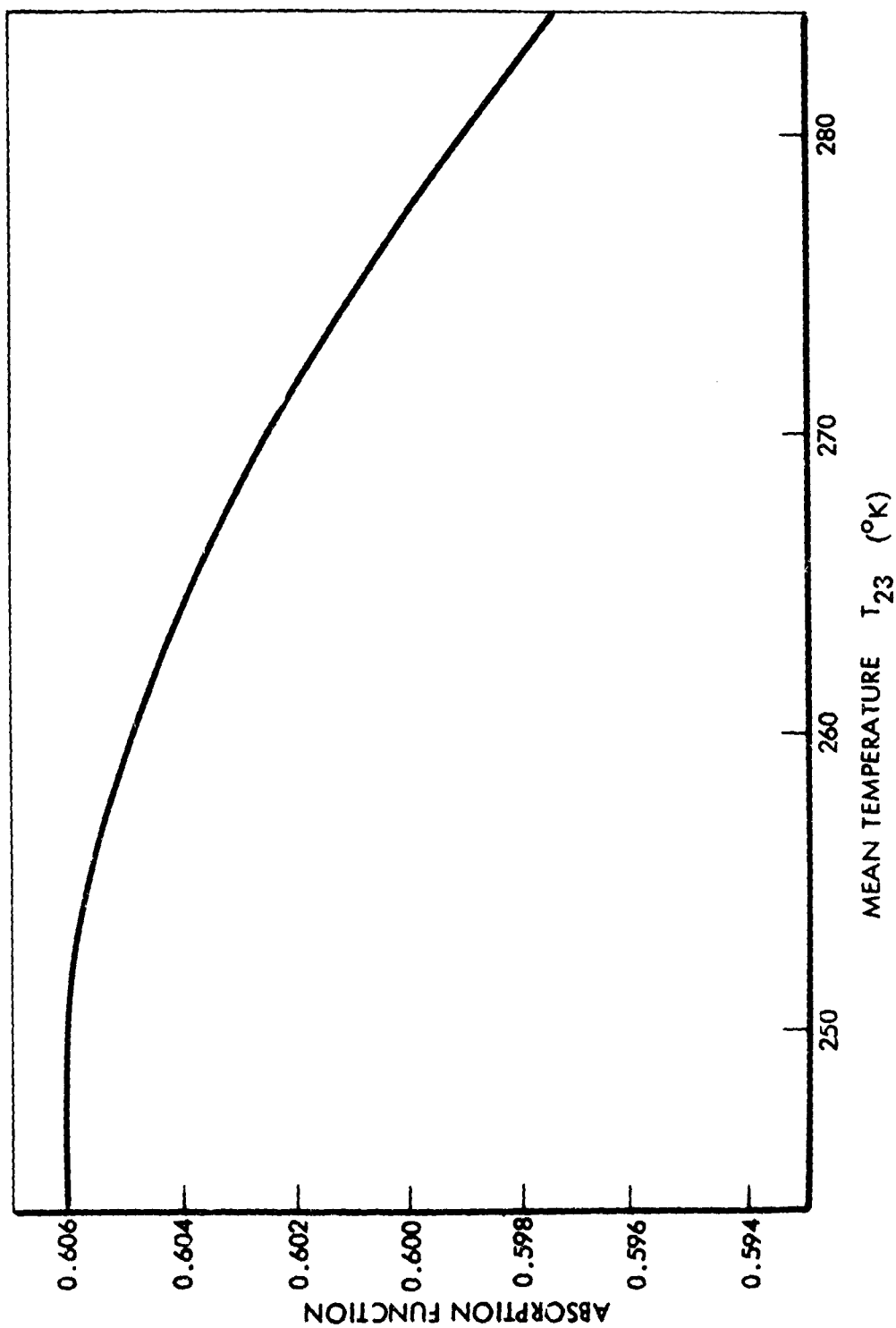


Figure 15: ABSORPTION FUNCTION VERSUS MEAN TEMPERATURE

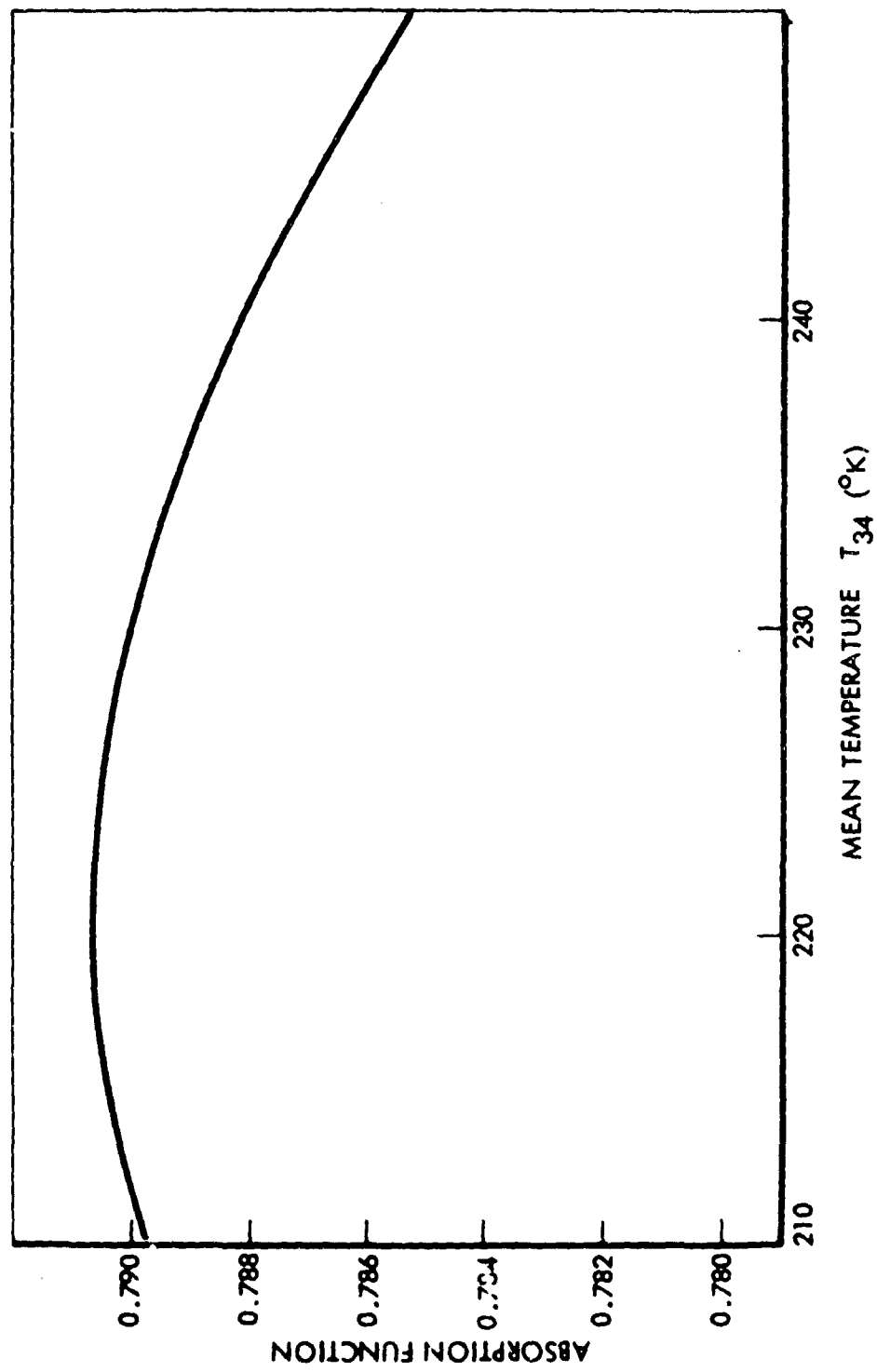


Figure 16: ABSORPTION FUNCTION VERSUS MEAN TEMPERATURE

$T_{B,2}$ and $T_{B,3}$ can be eliminated from the above simultaneous equations to give

$$T_{B,1} = (a_{2,1})(a_{3,2})(a_{4,3})T_{B,4} + (a_{3,2})(a_{2,1})[1-(a_{4,3})]\langle T_{4,3} \rangle \quad (129) \\ + (a_{2,1})[1-(a_{3,2})]\langle T_{3,2} \rangle + [1-(a_{2,1})]\langle T_{2,1} \rangle$$

This equation can be explained in physical terms. The factor $(a_{2,1})(a_{3,2})(a_{4,3})T_{B,4}$ is the brightness temperature at the bottom of the model $T_{B,1}$ contributed by the flux at the top of the model, which is attenuated by the three intervening layers. If there is no source (such as the Sun or Moon) in the antenna pattern, this brightness temperature would be on the order of 0° Kelvin. The term $[1-(a_{4,3})]\langle T_{4,3} \rangle$ is the self-emission (since 1 minus absorptivity is equal to the emissivity) of the topmost layer. When this is multiplied by $(a_{3,2})(a_{2,1})$, the attenuation due to the two layers below it gives the contribution to $T_{B,1}$ from the topmost layer. Similar attributes can be assigned to the other two terms in the equation.

With a three-frequency system, three equations like Equation 129 differ in the $\langle T_B \rangle$ coefficients to the extent the a's are frequency-dependent. These three equations form a unique set of transcendental equations that must be solved by numerical methods. An iterative approach must be used in which the $\langle T_B \rangle$'s for each layer are "guessed" in the first approximation. Based on these guesses $\langle T_B \rangle$'s the appropriate values of the a's are substituted into the set of equations. The process is repeated, narrowing the choice of $\langle T_B \rangle$'s until the matrix of the set of equations is solved. The $\langle T_B \rangle$'s so defined can then be used, in conjunction with the measured brightness temperatures, in the manner prescribed by Equation 127 to determine the integrals of the absorption coefficients for each layer.

Strictly, Equations 125a, b, and c should also be integrated with respect to frequency. This integration can be accomplished. However, the a's have been found to be smooth, almost linear functions with respect to frequency; thus the value at the center of the operating band can be used because it closely represents the mean value that would result from the integration. Also, this

integration has not been done because the manner in which the integration will have to be performed depends on the filter characteristics of the electronics. Further, the antenna beam pattern will have to be considered because this factor will somewhat weight the results.

The frequencies chosen for this study — 51.2, 52.3, 52.8, and 53.3 GHz — were chosen for their proximity because of bandwidth considerations in the radiometer design. They are centered between absorbing lines for maximum smoothness of the absorption functions. If more detailed profiling near the ground is desired, the mean temperatures obtained from the above frequencies could be used together with frequencies more strongly absorbed.

(B) Water-vapor profile

The approach to surveying the water-vapor profile from brightness-temperature measurements would be similar to that of the case of oxygen. That is inversion, in the manner just presented, of Equation 114 relative to the 22-GHz water-vapor absorption coefficient would permit generation of a new set of integrated absorption coefficients as functions of mean temperature. Measured brightness temperatures performed in the wing of the 22-GHz band would then establish the set of equations, represented by Equation 129, required to define the mean temperature in any atmospheric layer. The result would then define the integrated absorption coefficient for that layer.

In the case of absorption in the vicinity of 22 GHz, however, a complication arises because the wing of the 60-GHz oxygen band extends well into the 22-GHz frequency region. The result is that oxygen absorption can influence brightness temperatures in the 22-GHz vicinity. For large, total, water-vapor contents (i.e., large water-vapor absorption), such as would be realized in looking at the total depth of the atmosphere, such effects are negligible. This is the point emphasized by Menius, et al, in their discussion of the MARCOR water-vapor radiometer. However, if consideration is to be given to profiling the atmospheric water-vapor content is to be considered (and it must if passive radiometric techniques are to be applied to provide slant-range corrections for targets imbedded in the atmosphere), then in atmospheric layers of low

absolute humidity the oxygen absorption in the vicinity of 22 GHz can attain significant proportions. This fact is demonstrated by Figures 17 and 18, which show both the oxygen and water-vapor absorption (calculated according to Equation 69), assuming saturation at standard surface temperature and pressure (Figure 17) and saturation at standard 300-mb temperature and pressure (Figure 18). For example, notice that under surface conditions the 20-GHz water-vapor absorption is about an order of magnitude greater than the oxygen absorption; however, at 300 mb the water-vapor absorption is greater than that of oxygen by about a factor of only two.

Nevertheless, the problem seemingly presented here is readily solved when it is recognized that extinction effects are additive (Equation 88). The integrated layer absorption coefficients derived from 22-GHz brightness-temperature measurements can thus be corrected for the oxygen effects simply by subtracting the adjusted (for frequency) absorption coefficient data obtained with the 55-GHz profiling radiometer. Because of this need, it is safe to say that accurate water-vapor profiling cannot be accomplished unless corresponding oxygen data is supplied with a 55-GHz profiling radiometer.

(B) Additional comments

It is often stated that the dry-air contribution to line-integrated refractivity can be attained "with sufficient accuracy from ground-level measurements and available knowledge of the variation of atmospheric density with altitude," (Reference 25). If this is true, then the need for an oxygen radiometric system is questionable. The need for the oxygen measurement capability is adequately established in the profiling mode of operation; but beyond that, consider that Equation 127, when the entire depth of the atmosphere is considered, is essentially that presented by Menius, et al (Reference 25), for analysis of the MARCOR data. Note especially that equal weights are given to both the "mean" temperature and the brightness temperature for their effect on the specification of integrated absorption coefficient. Therefore, concern over accuracies in brightness-temperature measurement, as related to accuracies in integrated absorption specification, is just half the problem. Equal concern must be given to the accurate specification of $\langle T \rangle$. Accuracy in $\langle T \rangle$ to the same degree as the accuracy

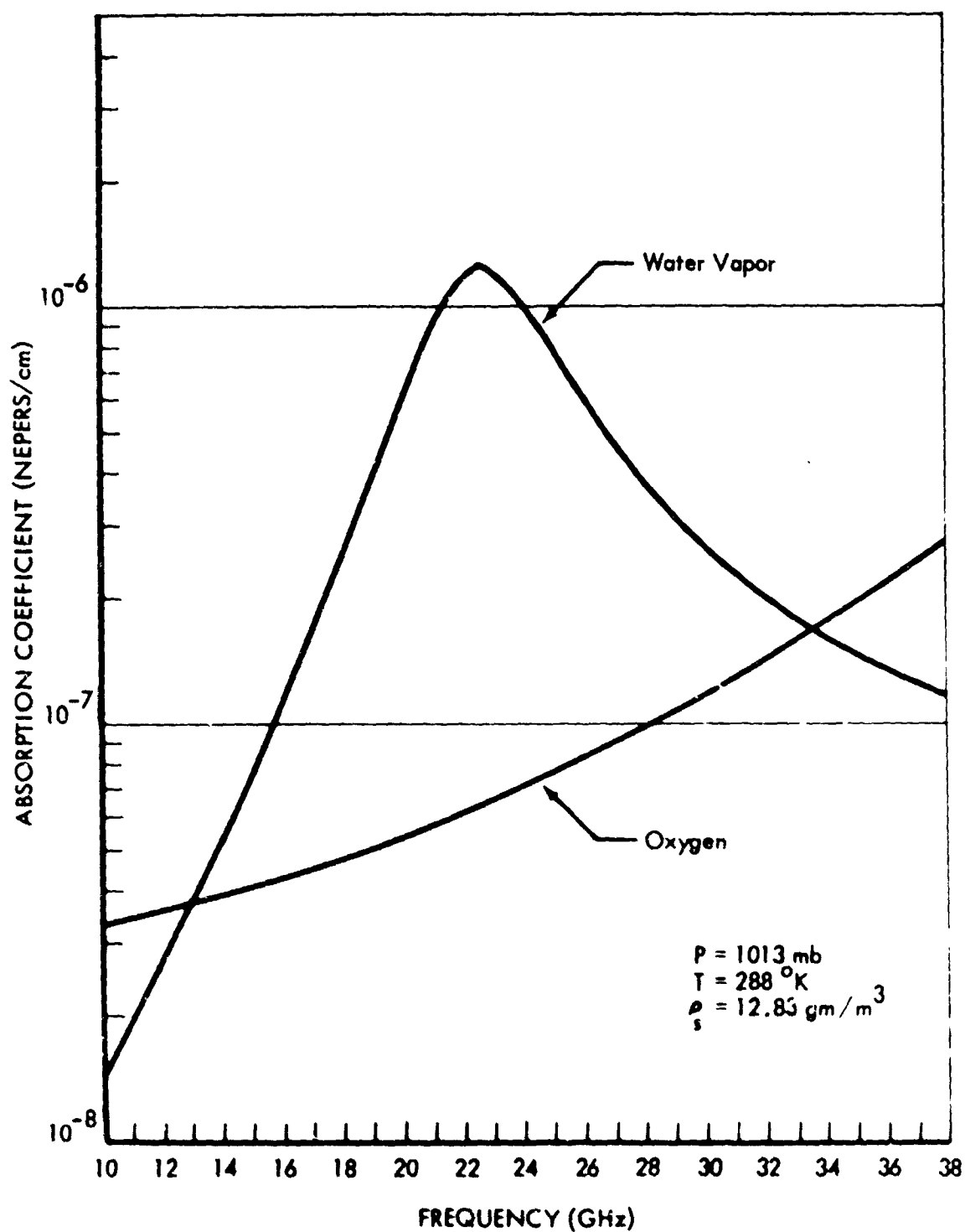


Figure 17: WATER-VAPOR AND OXYGEN ABSORPTION IN A SATURATED ATMOSPHERE AT STANDARD SURFACE TEMPERATURE AND PRESSURE

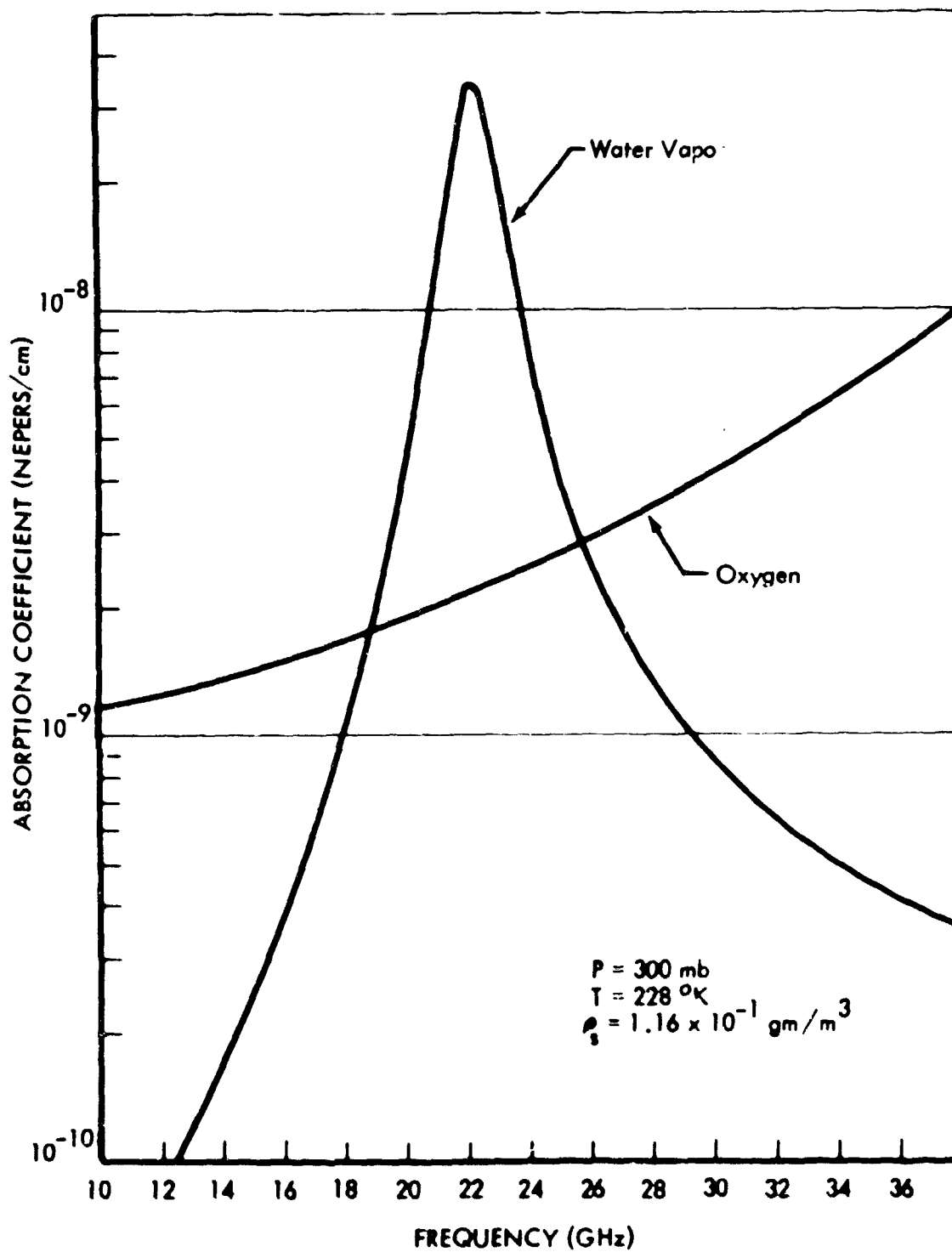


Figure 18: WATER-VAPOR AND OXYGEN ABSORPTION IN A SATURATED ATMOSPHERE AT 300 mb (Standard Temperature)

in T_B simply cannot be attained, "from ground-level measurements," but can only be attained radiometrically from oxygen absorption measurements in the manner outlined in the paragraph entitled "The Oxygen Profile." That is, the $\langle T \rangle$ input to any water-vapor brightness-temperature analysis must be supplied from the data attained through oxygen-absorption measurements.

C. Summary

Several radiometric refractometer configurations are required if the need for \bar{N} -measurement is to be satisfied in all ranging activities. A combination infrared/microwave active system will provide the most accurate \bar{N} data. This is the system best suited for use in missile test range operations, insofar as such operations are characterized by: (1) the availability of cooperative targets, and (2) conformance of test schedules to ideal weather conditions. In using the $1.26\text{-}\mu$ oxygen and the $1.37\text{-}\mu$ water-vapor infrared band, and the 22-GHz microwave water band, all three terms of the integrated Smith-Weintraub refractivity equation are measured in their precise functional form.

To extend the operational capability of the active system to cloudy conditions, microwave absorption in the 55-GHz oxygen band can be used to approximate the dry-air term of \bar{N} , and the 22-GHz band can be used to provide data relating to both water-vapor terms. However, in this approach some loss of accuracy is incurred because an independent measure of a suitably defined "mean" temperature must be acquired for an adjustment of the oxygen and water-vapor data. That is, the microwave data must be multiplied by this mean temperature before that data can be accepted as defining the first two terms of the \bar{N} equation.

For the case of noncooperative targets, the passive mode of operation is mandatory; i.e., \bar{N} must be determined by measuring atmospheric thermal emissions in the microwave oxygen and water-vapor bands previously specified. Moreover, multifrequency capabilities must be provided in each band to permit a degree of \bar{N} profiling — a mandatory capability if the passive system is to be applied to tracking noncooperative targets imbedded in the atmosphere.

6. ERROR ANALYSIS

To estimate residual errors that remain in \bar{N} or in slant-range data after the line-integral refractometers just discussed are applied to typical ranging operations, certain assumptions must be made regarding the atmosphere and the measurement process and instrumentation. This will consist largely of postulations of simplified models for the refractometers and atmosphere, which will permit at least a semblance of analytical procedure in an otherwise intractable problem. The final results can be given no more of an interpretation other than that they represent reasonable estimates of what actuality will eventually show.

A. Basic \bar{N} -error equation

Denoting integrated values by an overbar, Equation 79 is written as

$$\bar{N} = \frac{k_1}{\omega_{c_2}} \bar{\rho}_{o_2} + k_2 \bar{\rho}_w + k_3 \left(\frac{\bar{\rho}_w}{T} \right). \quad (130)$$

There are uncertainties in each element of the right-hand side of Equation 130. The k-constants and ω_{o_2} are uncertain to the extents indicated in Equations 74 and 77, respectively; there will also be, as in any physical measurement, uncertainties in the specifications of $\bar{\rho}_{o_2}$, $\bar{\rho}_w$, and $(\bar{\rho}_w/T)$. If all these uncertainties are assumed to be uncorrelated, the corresponding uncertainty in \bar{N} can be determined from the total differential of \bar{N} :

$$d\bar{N} = \frac{\partial \bar{N}}{\partial k_1} dk_1 + \frac{\partial \bar{N}}{\partial k_2} dk_2 + \frac{\partial \bar{N}}{\partial k_3} dk_3 + \frac{\partial \bar{N}}{\partial \omega_{c_2}} d\omega_{c_2} + \frac{\partial \bar{N}}{\partial \bar{\rho}_{o_2}} d\bar{\rho}_{o_2} + \frac{\partial \bar{N}}{\partial \bar{\rho}_w} d\bar{\rho}_w + \frac{\partial \bar{N}}{\partial (\frac{\bar{\rho}_w}{T})} d\left(\frac{\bar{\rho}_w}{T}\right) \quad (131a)$$

expressed in terms of finite increments as

$$\Delta \bar{N} = a \Delta k_1 + b \Delta k_2 + c \Delta k_3 + d \Delta \omega_{c_2} + e \Delta \bar{\rho}_{o_2} + f \Delta \bar{\rho}_w + g \Delta \left(\frac{\bar{\rho}_w}{T} \right) \quad (131b)$$

In the above incremental equation, the coefficients, which are to be evaluated with reference to some set of "standard" conditions, are defined by

6. ERROR ANALYSIS

To estimate residual errors that remain in \bar{N} or in slant-range data after the line-integral refractometers just discussed are applied to typical ranging operations, certain assumptions must be made regarding the atmosphere and the measurement process and instrumentation. This will consist largely of postulations of simplified models for the refractometers and atmosphere, which will permit at least a semblance of analytical procedure in an otherwise intractable problem. The final results can be given no more of an interpretation other than that they represent reasonable estimates of what actuality will eventually show.

A. Basic \bar{N} -error equation

Denoting integrated values by an overbar, Equation 79 is written as

$$\bar{N} = \frac{k_1}{\omega_{O_2}} \bar{\rho}_{O_2} + k_2 \bar{\rho}_w + k_3 \left(\frac{\bar{p}_w}{T} \right). \quad (130)$$

There are uncertainties in each element of the right-hand side of Equation 130. The k-constants and ω_{O_2} are uncertain to the extents indicated in Equations 74 and 77, respectively; there will also be, as in any physical measurement, uncertainties in the specifications of $\bar{\rho}_{O_2}$, $\bar{\rho}_w$, and (\bar{p}_w/T) . If all these uncertainties are assumed to be uncorrelated, the corresponding uncertainty in \bar{N} can be determined from the total differential of \bar{N} :

$$d\bar{N} = \frac{\partial \bar{N}}{\partial k_1} dk_1 + \frac{\partial \bar{N}}{\partial k_2} dk_2 + \frac{\partial \bar{N}}{\partial k_3} dk_3 + \frac{\partial \bar{N}}{\partial \omega_{O_2}} d\omega_{O_2} + \frac{\partial \bar{N}}{\partial \bar{\rho}_{O_2}} d\bar{\rho}_{O_2} + \frac{\partial \bar{N}}{\partial \bar{\rho}_w} d\bar{\rho}_w + \frac{\partial \bar{N}}{\partial (\frac{\bar{p}_w}{T})} d\left(\frac{\bar{p}_w}{T}\right) \quad (131a)$$

expressed in terms of finite increments as

$$\Delta \bar{N} = a \Delta k_1 + b \Delta k_2 + c \Delta k_3 + d \Delta \omega_{O_2} + e \Delta \bar{\rho}_{O_2} + f \Delta \bar{\rho}_w + g \Delta \left(\frac{\bar{p}_w}{T} \right) \quad (131b)$$

In the above incremental equation, the coefficients, which are to be evaluated with reference to some set of "standard" conditions, are defined by

$$\begin{aligned}
a &= \frac{\partial \bar{N}}{\partial k_1} = \frac{\bar{\rho}_{O_2}}{\omega_{O_2}} & d &= \frac{\partial \bar{N}}{\partial \omega_{O_2}} = -\frac{k_1 \bar{\rho}_{O_2}}{\omega_{O_2}^2} & g &= \frac{\partial \bar{N}}{\partial \left(\frac{\bar{p}_w}{T}\right)} = k_3 \\
b &= \frac{\partial \bar{N}}{\partial k_2} = \bar{\rho}_w & e &= \frac{\partial \bar{N}}{\partial \bar{\rho}_{O_2}} = \frac{k_1}{\omega_{O_2}} \\
c &= \frac{\partial \bar{N}}{\partial k_3} = \left(\frac{\bar{\rho}_w}{T}\right) & f &= \frac{\partial \bar{N}}{\partial \bar{\rho}_w} = k_2
\end{aligned} \tag{132}$$

With uncorrelated uncertainties, the variance in \bar{N} is simply

$$\begin{aligned}
(\Delta N)^2 &= \{ (a \Delta k_1)^2 + (b \Delta k_2)^2 + (c \Delta k_3)^2 + (d \Delta \omega_{O_2})^2 \} \\
&\quad + \{ (e \Delta \bar{\rho}_{O_2})^2 + (f \Delta \bar{\rho}_w)^2 + (g \Delta \left[\frac{\bar{p}_w}{T}\right])^2 \}
\end{aligned} \tag{133}$$

In the above equation, notice that the sum of the terms in the first set of brackets on the right-hand side represents the contribution to the variance in \bar{N} arising from basic uncertainties (the Δk 's and $\Delta \omega_{O_2}$) in the integrated refractivity equation itself. As such, it defines the fundamental limit of the accuracy to which \bar{N} may be specified by measuring subsidiary meteorological parameters. In other words, reduction of the incremental terms in the second bracket by using improved sampling techniques, can be pushed just so far. Consider, first, the evaluation of the terms included in the first brackets.

B. Variance in \bar{N} established by equation uncertainties

The standard conditions required for assignment of values to the constants a through d in Equation 133 may be taken as those defined by the U. S. Standard Atmosphere. This atmosphere has an equivalent thickness*, L, in the zenith direction of 8.4 km, an oxygen partial density of $2.66 \times 10^2 \text{ gm/m}^{-3}$, and a temperature of 288°K. Also, consider a standard atmospheric water-vapor content of 2.0 precipitable centimeters. The relationship between precipitable centimeters, w and ρ_w is

$$\rho_w = \frac{w}{L} \cdot 10^4 \cdot \frac{\text{gm}}{\text{m}^3} \tag{134}$$

*Equivalent thickness is defined by the height to which a homogeneous atmosphere would extend at temperature T and pressure p.

when W is given in precipitable centimeters, and the path length L is given in meters. In this homogeneous atmosphere, the integrated partial densities may be considered simply as the product of density by path length. Taking the k - and ω_{02} -uncertainties as given in Equations 74 and 77, the standard conditions listed above, and the atmospheric path as the equivalent atmospheric path, the numerical values of the factors appearing in the first set of brackets on the right-hand side of Equation 133 are as given in Table 6. According to the definition of air mass as the ratio of the path length through the atmosphere at any given angle to the path length toward the zenith (Reference 46), the values are listed as applying to one standard air mass.

Table 6: Values of the Constants a , b , c , and d , and of the Error Components Δk_1 , Δk_2 , Δk_3 , and $\Delta \omega_{02}$, in the \bar{N} rms Error Equation, Through One Standard Air Mass

| Constant | Numerical Values | | Error Component |
|----------|---------------------|---------------------------|----------------------|
| | Constant | Error Component | |
| a | 1.02×10^7 | $\pm 3.7 \times 10^{-5}$ | Δk_1 |
| b | 2.0×10^4 | $\pm 3.92 \times 10^{-2}$ | Δk_2 |
| c | 6.95×10^1 | ± 14.3 | Δk_3 |
| d | -9.75×10^6 | $\pm 5.0 \times 10^{-5}$ | $\Delta \omega_{02}$ |

The data in Table 6 permits the estimates, shown in Table 7, of the contribution of each of the error components to the total variance in \bar{N} .

Table 7: Contributions of the Error Components to the Total Variance in \bar{N}

| Contributions to Total Variance due to: | | | | Total \bar{N} Variance Per Air Mass | Total \bar{N} rms Error Per Air Mass |
|---|--------------------|--------------------|----------------------|--|--|
| Δk_1 | Δk_2 | Δk_3 | $\Delta \omega_{02}$ | | |
| 1.43×10^5 | 6.15×10^5 | 9.88×10^2 | 4.88×10^2 | 7.59×10^5 | 8.71×10^2 |

The data contained in Table 7 define the inherent limitation to the accuracy attainable in line-integrated refractivity measurement through application of

oxygen and water-vapor optical depth measurement data to Equation 79. That is, assuming errorless determinations of \bar{P}_{O_2} , \bar{P}_w , and (\bar{P}_w/T) could be made, the inferred \bar{N} data would be subject to an rms error in \bar{N} of about 8.71×10^2 meters per air mass, or to about 0.04 percent in \bar{N} . To such precision then, the equation for line-integrated refractivity becomes, from Equation 79 with the k - and ω_{O_2} -values to three significant figures,

$$\bar{N} = 0.964 \bar{P}_{O_2} + 0.53 \bar{P}_w + 1730 \left(\frac{\bar{P}_w}{T} \right). \quad (135)$$

C. Variance in \bar{N} established by radiometric measurement errors

The terms in the second set of brackets on the right-hand side of Equation 133 determine the contribution of the uncertainty in \bar{N} -specification due to errors (the $\Delta \bar{P}$'s) in measurement of \bar{P}_{O_2} , \bar{P}_w , and (\bar{P}_w/T) . Two factors may be considered as contributing to such measurement errors; viz., instrumental "noise," and atmosphere-induced errors. Consider first the latter factor, assuming, in effect, "perfect" instrumentation. This will establish the atmospheric "noise level" to which the instrumentation may be designed.

(1) Modified transmission equations

The basic premise of the radiometric approach to the measurement of the integrated partial density data demanded by Equation 135 is that the attenuation (or emission) of energy in an atmospheric-constituent absorption band proceeds in portion to the total amount of the constituent in the path over which the energy is propagated. To isolate energy in the absorption bands of interest, narrow band-pass interference filters may be used in infrared regions of the spectrum, and, at radio wavelengths, suitable band-pass amplifiers may be used to accomplish the same result. But where such mechanisms may be extremely efficient, in general the passed bands will be of a width to require that they be considered as delineating still an unresolved spectral absorption line structure. A description of transmittance in such a band requires a more complicated transmission function (i.e., explicit definition of Equation 80) than the simple Bouguer-Beer Law relationship of Equation 84 (Reference 47). That is, in the development of a function to describe atmospheric transmittance over a group of unresolved

lines, it must be recognized that the net effect represents the summing up, over the frequency interval defined by the band-width of the filter, of the individual effects of a multitude of lines, each contributing to absorption according to Equations 66 & 67. The transmitted spectral radiation is therefore not uniform, since in the region of absorption lines it is decreased, and at the centers of intense lines it is possible for the absorption to be complete. Thus, as the thickness of the transmitting gas is changed, there is a change not only in the intensity of the radiation, but also in its spectral composition, which predetermines the peculiarity of the absorption laws in spectral measurements of unresolved structures.

In general, an isolated group of lines in an unresolved band is characterized by differing mutual distributions, degrees of overlapping, integral intensities, half-widths, and values of effective collision diameters. For such a system a general solution to the problem of calculating the band transmittance is not possible, since it is peculiarly complex, and awkward, and requires a knowledge of the individual character of each line. Accordingly, various model systems have been proposed, approaching in greater or lesser degree to actual molecular spectra. Elsasser, for example, proposed a system of lines of equal intensity and width occurring with equal distances between lines, an adequate representation of the oxygen spectrum (Reference 48). In his statistical model, Goody introduced a system of randomly distributed lines, the intensities of which are similarly randomly distributed, as a representation of the water-vapor spectrum (Reference 23). From these models, the following transmission functions, defined for Lorentzian line shapes, may be stated. First, from the Goody model, the transmission in a water-vapor band is

$$\tau_w(\Delta\nu, \bar{P}_w) = \exp \left[\frac{\epsilon P_w}{\pi d \left(1 + \frac{\epsilon \bar{P}_w}{\pi \Delta\nu} \right)^2} \right], \quad (136)$$

and from the Elsasser model the oxygen transmission is

$$\tau_{O_2}(\Delta\nu, \bar{P}_{O_2}) = \int_{-1/2}^{+1/2} \exp \left[\frac{\epsilon \bar{P}_{O_2}}{d} \cdot \frac{\sinh(2\pi \Delta\nu/d)}{\cosh(2\pi \Delta\nu/d) - \cos(\nu/d)} \right] d\left(\frac{\nu}{d}\right) \quad (137)$$

where \bar{c} denotes the average line intensity in the spectral interval, d the mean spacing between lines.

(2) Interpolation equations

Equations 136 and 137 can be approximated (References 49 and 47) in the following fashion. For large water-vapor optical depths ("strong" absorption), the term $(\bar{\rho}_w/\pi\Delta\nu)$ in the denominator of the argument of the exponential in Equation 136 is much greater than unity, and the equation reduces the

$$\ln \tau_w \approx -c_1 (\bar{\rho}_w \Delta\nu)^{1/2} \quad (138)$$

where c_1 denotes a generalized absorption coefficient incorporating the line intensity and line spacing parameters. Conversely, at small optical depths $(\bar{\rho}_w/\pi\Delta\nu) \ll 1$, and

$$\ln \tau_w \approx -(c_2 \bar{\rho}_w + c_3 \bar{\rho}_w^2) \quad (139)$$

In the intermediate case when $(\bar{\rho}_w/\pi\Delta\nu) = 1$,

$$\ln \tau_w \approx -c_4 \bar{\rho}_w \quad (140)$$

In the case of oxygen, "strong" band absorption is associated with pronounced "overlapping" of the regularly spaced lines. Thus the strong absorption is defined when the term $2\pi\Delta\nu/d$ in the arguments of the transcendental functions on the right-hand side of Equation 137 are much larger than unity. When such is the case,

$$\ln \tau_{O_2} \approx -c_5 \bar{\rho}_{O_2} \quad (141)$$

In the weak absorption case, $2\pi\Delta\nu/S \ll 1$, and

$$\tau_{O_2} \approx 1 - c_6 \bar{\rho}_{O_2} \quad (142)$$

For the intermediate case

$$\tau_{O_2} \approx 1 - c_7 (\bar{\rho}_{O_2} \Delta\nu)^{1/2} \quad (143)$$

Keep in mind that Equations 138, 139, 140, 141, 142, and 143 are basically interpolation equations that express their respective general transmission laws in terms of three successive approximations. At just what value of transmittance a given form of one of the interpolations takes over from another cannot be stated absolutely. There obviously must be a smooth transition from one to the other.

(3) Line-broadening errors

A peculiarity to be noted in Equations 138 through 143 is that in the "square-root law" regimes of both water-vapor and oxygen transmission, τ is a function not only of the integrated densities, but also of the line width, $\Delta \nu$. It is likely, moreover, that in performing the transmission measurements to obtain the necessary data for computing line-integrated refractivity in ranging operations, a good part (if not the bulk) of such measurements will be performed at transmittance values where the square-root laws are applicable. Thus, in general, the inversion of the τ -data to yield $\bar{\rho}$ -data will involve relations of the type

$$\bar{\rho} = f(\tau, \Delta \nu) \quad (144)$$

In the manner of Equation 133 then, the variance of the uncertainty in $\bar{\rho}$ -specification can be estimated from an expression of the form

$$(\Delta \bar{\rho})^2 = (h \Delta \tau)^2 + [i \Delta(\Delta \nu)]^2 \quad (145)$$

Two effects are thus seen to contribute to errors in $\bar{\rho}$ -data: those arising from τ -measurement errors, and those stemming from uncertainties in the specification of the line-width parameter, $\Delta \nu$.

Consider first that the latter source of error in $\bar{\rho}$ -specification is determined by the pressures of both the absorbing and foreign gases of the atmosphere, by the temperature, and by the effective collision diameters of the absorbing and foreign gas molecules. These collision diameters are determined, too, relative to the pressures of the gases and not by the number of collisions (Reference 47). The net result is that in terms of pressure and temperature, $\Delta \nu$ can be expressed as

$$\Delta\nu = f_1(\Delta\nu_0, p_0, T_0, p, T) \quad (146)$$

where the subscripts denote the values of the various parameters under some set of standard conditions.

Equation 146 indicates that, due to the dependence of $\Delta\nu$ on p and T , the line-width parameter also is a function of position in the atmosphere. Therefore, the integration of partial density called for to effect an evaluation of \bar{N} must really be an integration of the product of partial density by line width; i.e.,

$$\bar{\rho} = \int_0^s \rho(s) \Delta\nu(s) ds \quad \text{a)}$$

or

$$\bar{\rho} = \int_0^s \rho(s) f_2[p(s), T(s)] ds \quad \text{b)}$$

The integration called for in Equation 147b can be accomplished explicitly only if one is willing to assume: first, an explicit form for f_2 ; second, horizontal homogeneity and an exponential variation of both pressure and temperature with altitude so that an explicit expression for f_2 as a function of position in slant-path operations may be specified; and third, that the mixing ratio of ρ remains constant throughout the atmosphere. When this is done, the integration called for yields an expression for an equivalent optical depth (defined as a function of slant-path end point), surface conditions of temperature and pressure, and slant-path elevation angle (see, for example, Reference 50); i.e.,

$$\bar{\rho}_e = f_3(S, p_{sfc}, T_{sfc}, \epsilon) \quad (148)$$

On the basis of an equation of the type depicted by Equation 148, an explicit functional relationship could be derived, in the manner of Equation 131, for the uncertainties in $\bar{\rho}$ -specification attributable to uncertainties in p and in T , and thus $\Delta\nu$. However, all assumptions required to arrive at such an equation

are questionable at best. Regarding the case of water-vapor absorption especially, the assumption of the constant mixing ratio is particularly bad. On a statistical basis, the constant mixing ratio might at least approach something near actuality, but on a day-to-day operational basis, atmospheric water vapor is usually found to occur in well-defined layers at various heights throughout the depth of the atmosphere.

Rather than go the route of the explicit error analysis then, an appeal is made to direct observation as to what the effects of pressure and temperature line broadening effects might have on the accuracy of \bar{P} measurement. Foster, Volz, and Foskett (Reference 51) have developed a photoelectric spectral hygrometer for the ESSA for determining integrated water-vapor densities. The hygrometer monitors the relative radiant intensity of direct solar energy transmitted in a water-vapor absorption band, and, in the manner specified previously, compares the absorbed energy to the energy received in a nearby atmospheric window. The instrument is mounted on a clock-driven equatorial telescope mount, so that the device tracks the Sun from sunrise to sunset. The device was calibrated through comparisons of the hygrometer outputs to measures of precipitable water vapor calculated from standard radiosonde data. In this way, pressure and temperature line-broadening effects were "calibrated in" to the system. Having calibrated their system, subsequent operation has shown that changes in total precipitable water, as detected by the spectral hygrometer, were consistently comparable to those changes indicated by successive radiosonde measurements, regardless of the altitude, (hence, the temperature and pressure) at which the changes occurred. Subsequent attempts were made in an effort to obtain a quantitative appraisal of the line-broadening effect on \bar{P}_w -determinations, with the results that the magnitude of such effects were found to result in errors not normally in excess of 2 or 3 percent of the total amount of water vapor, with the extreme error, under conditions of extreme water-vapor layering, being on the order of 10 percent. As indicated earlier, these estimates may also be considered representative of the accuracy to which the measurement of the integrated ratio of water vapor density-to-temperature may be performed at microwave frequencies. These estimates, based on the findings of Foster, et al, are also in agreement with those of Kondrat'ev, et al

(Reference 52). Because the oxygen-mixing ratio is constant throughout the depth of the atmosphere, the layering problem is largely eliminated as a source of \bar{p}_{O_2} -specification uncertainty. Horizontal heterogeneity still will give an equivalent layering effect. Therefore, although the oxygen data will be much more precise than that of water vapor, an error of from ± 0.5 to 1 percent must still be accepted. The latter estimate is substantiated by the work of Westwater (Reference 27).

(4) N-errors related to transmittance measurement errors

Proceeding now to the contribution of τ -measurement errors to uncertainties in \bar{p} -specification (Equation 145), consider the implications of the various forms of the water-vapor and oxygen transmission laws (as stated in Equations 138 through 140, and 141 through 143, respectively) as to the relation between $\Delta\tau$ and $\Delta\bar{p}$. Defining the relative errors in \bar{p} -specification and τ -measurement as $\delta(\bar{p}) = \Delta\bar{p}/\bar{p}$ and $\delta(\tau) = \Delta\tau/\tau$, respectively, the following relations are obtained by differentiation of Equations 138 and 139, and 141 and 142:

$$\frac{\delta(\bar{p}_w)}{\delta(\tau)} = -\frac{2}{\ln \tau_w}, \text{ strong absorption} \quad (149)$$

$$\frac{\delta(\bar{p}_w)}{\delta(\tau)} = -\frac{1}{\ln \tau_w}, \text{ weak absorption} \quad (150)$$

and

$$\frac{\delta(\bar{p}_{O_2})}{\delta(\tau_{O_2})} = -\frac{1}{\ln \bar{p}_{O_2}}, \text{ strong absorption} \quad (151)$$

$$\frac{\delta(\bar{p}_{O_2})}{\delta(\tau_{O_2})} = \frac{\tau_{O_2}}{(1-\tau_{O_2})}, \text{ weak absorption} \quad (152)$$

Equations 149 through 152 are presented in Figure 19. The solid line depicts the ratio of the relative error in the integrated water-vapor density specification to the relative error in water-vapor transmittance measurement. The dashed line depicts the same ratio for the case of oxygen. The segments in the center of the curves denote the "transition" regions, as implied by Equations 140 and 143, between the "strong" and "weak" absorptions of Equations 138 and 141, and 140 and 143, respectively. The curves indicate that over a wide range of transmittances, the relative error in \bar{p} -specification, as related to the relative error in τ -measurement, is not very sensitive to the actual magnitude of the measured transmittance. A rule of thumb may, therefore, be es-

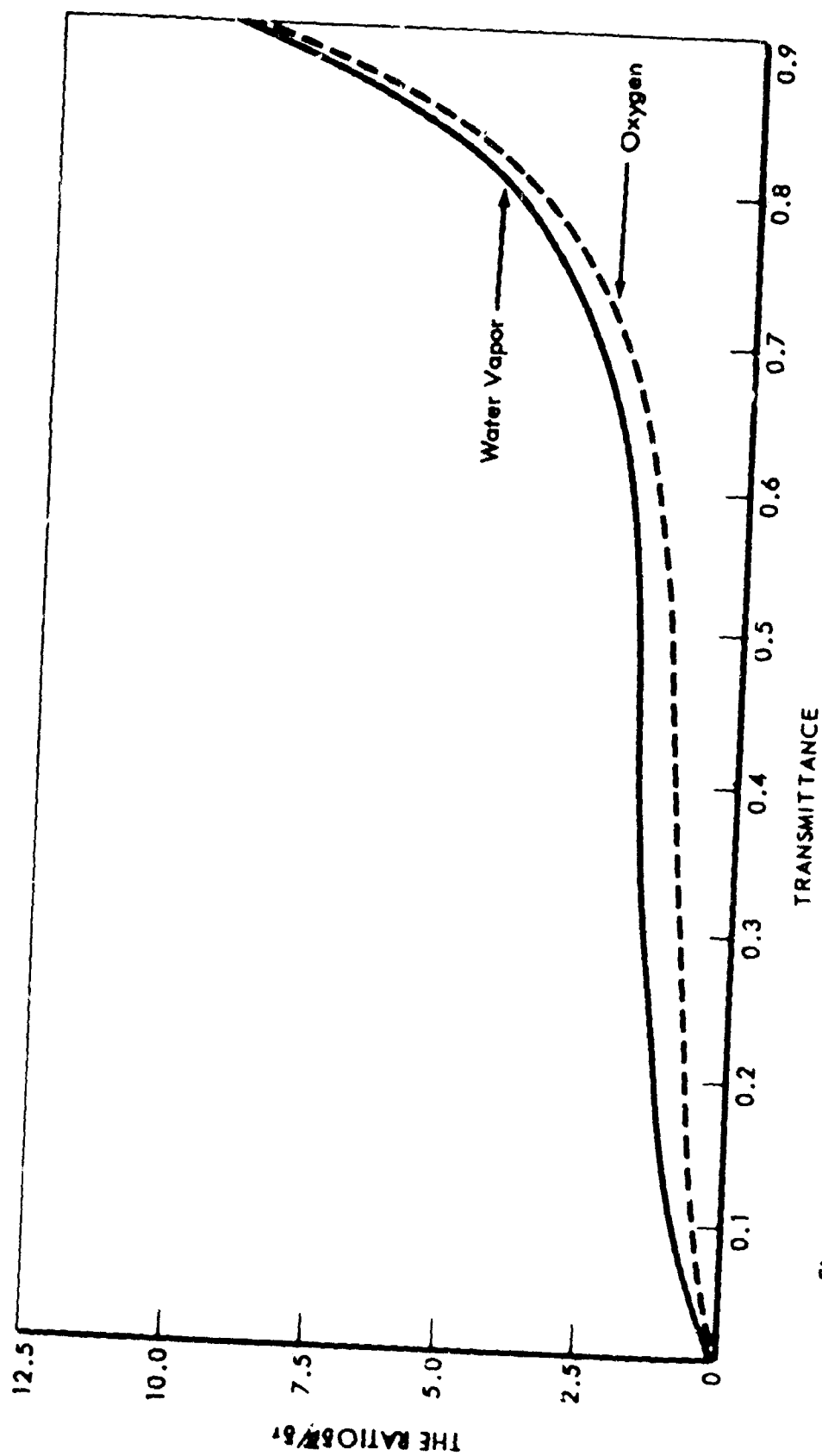


Figure 19: THE RATIO OF RELATIVE INTEGRATED DENSITY TO RELATIVE TRANSMITTANCE
ERRORS AS A FUNCTION OF TRANSMITTANCE

tablished for the purpose of the error analysis to follow: for transmittances ranging from about 10 to 70 percent, the relative error in $\bar{\rho}$ will be about twice that in τ . Also, because of the similar nature of the line-broadening effects at microwaves, this rule of thumb may be expected to apply to the case of microwave as well as infrared absorption.

The τ -error increment now, in terms of the actual measurements performed by a differential absorption spectrometer system, is obtained by differentiation of Equation 94:

$$\Delta\tau_a = K \left[-\frac{I_{sens}}{(I_{ref})^2} \Delta I_{ref} + \frac{1}{I_{ref}} \Delta I_{sens} \right] \quad (153)$$

But also from Equation (94), notice that

$$I_{ref} = \frac{K}{\tau_a} I_{sens} \quad (154)$$

and

$$\frac{I_{sens}}{I_{ref}} = \frac{\tau_a}{K} \quad (155)$$

Using Equations 154 and 155 appropriately in Equation (153), the latter transforms to

$$\Delta\tau_a = \tau_a \left[\frac{\Delta I_{sens}}{I_{sens}} - \frac{\Delta I_{ref}}{I_{ref}} \right] \quad (156)$$

The terms in the brackets of Equation (156) define relative changes in received sensing and reference-band energies attributable to effects other than energy absorption by the atmospheric constituent being sensed. If the above percentage changes are equal, the right-hand side of the equation is zero, and no error in absorption transmittance measurement will result. This, of course, is the reason for employing a reference band in the first place. However, several processes that are wavelength-dependent could act to attenuate both the reference and sensing-band energy intensities, thus making the right-hand side of Equation (156) nonzero, with the resultant degradation of $\bar{\rho}$ -measurement. Such processes might include (1) differential attenuation caused by the atmospheric continuum spectrum, and (2)

scintillation effects. These two effects can again be considered to act in an uncorrelated manner in the measurement degradation.

(A) Effects of the continuum spectrum — Infrared continuum

The infrared continuum spectrum is established by three processes: (1) scattering by the atmospheric aerosol, (2) absorption by the particles of which the aerosol is composed, and (3) absorption due to wings far removed from the resonant frequency line absorptions of all the various absorbing atmospheric constituents. Because, however, these processes combine to yield the continuum effect, the continuum transmission can be described by the Bouguer law,

$$\ln \tau_c = c'm, \quad (157)$$

where τ_c represents the continuum transmittance, c' the continuum extinction coefficient, and m the air mass. With regard to c' , it is significant to note that within the limits of the Bouguer law, the ratios in the brackets on the right-hand side of Equation 156 constitute the exact definitions of the extinction coefficient (Reference 53). Accordingly, Equation 156 may be expressed as

$$\frac{\Delta \tau_a}{\tau_a} = [c'_{sens} - c'_{ref}] \quad (158)$$

That is, the relative error in the absorption transmittance ascribable to the continuum extinction effect is given simply by the difference between the sensing and reference band continuum extinction coefficients.

Gates (Reference 54) presents the relationship between the continuum extinction coefficients and wavelength shown in Figure 20. Also indicated are the ordinates locating the 1.27μ oxygen band, the 1.32μ water-vapor band, and the 1.22μ window. With the window serving as the reference band for the other two absorption bands, the differences between the absorption and reference-band continuum extinction coefficients are estimated as being on the order of 10^{-3} for both the water-vapor and oxygen bands. Estimating the $\bar{\rho}$ -specification errors as twice these τ -measurement errors, it can still be said that, with the reference-

scintillation effects. These two effects can again be considered to act in an uncorrelated manner in the measurement degradation.

(A) Effects of the continuum spectrum — Infrared continuum

The infrared continuum spectrum is established by three processes: (1) scattering by the atmospheric aerosol, (2) absorption by the particles of which the aerosol is composed, and (3) absorption due to wings far removed from the resonant frequency line absorptions of all the various absorbing atmospheric constituents. Because, however, these processes combine to yield the continuum effect, the continuum transmission can be described by the Bouguer law.

$$\ln \tau_c = c' m, \quad (157)$$

where τ_c represents the continuum transmittance, c' the continuum extinction coefficient, and m the air mass. With regard to c' , it is significant to note that within the limits of the Bouguer law, the ratios in the brackets on the right-hand side of Equation 156 constitute the exact definitions of the extinction coefficient (Reference 53). Accordingly, Equation 156 may be expressed as

$$\frac{\Delta \tau_a}{\tau_a} = [c'_{\text{sens}} - c'_{\text{ref}}] \quad (158)$$

That is, the relative error in the absorption transmittance ascribable to the continuum extinction effect is given simply by the difference between the sensing and reference band continuum extinction coefficients.

Gates (Reference 54) presents the relationship between the continuum extinction coefficients and wavelength shown in Figure 20. Also indicated are the ordinates locating the 1.27μ oxygen band, the 1.32μ water-vapor band, and the 1.22μ window. With the window serving as the reference band for the other two absorption bands, the differences between the absorption and reference-band continuum extinction coefficients are estimated as being on the order of 10^{-3} for both the water-vapor and oxygen bands. Estimating the $\bar{\rho}$ -specification errors as twice these τ -measurement errors, it can still be said that, with the reference-

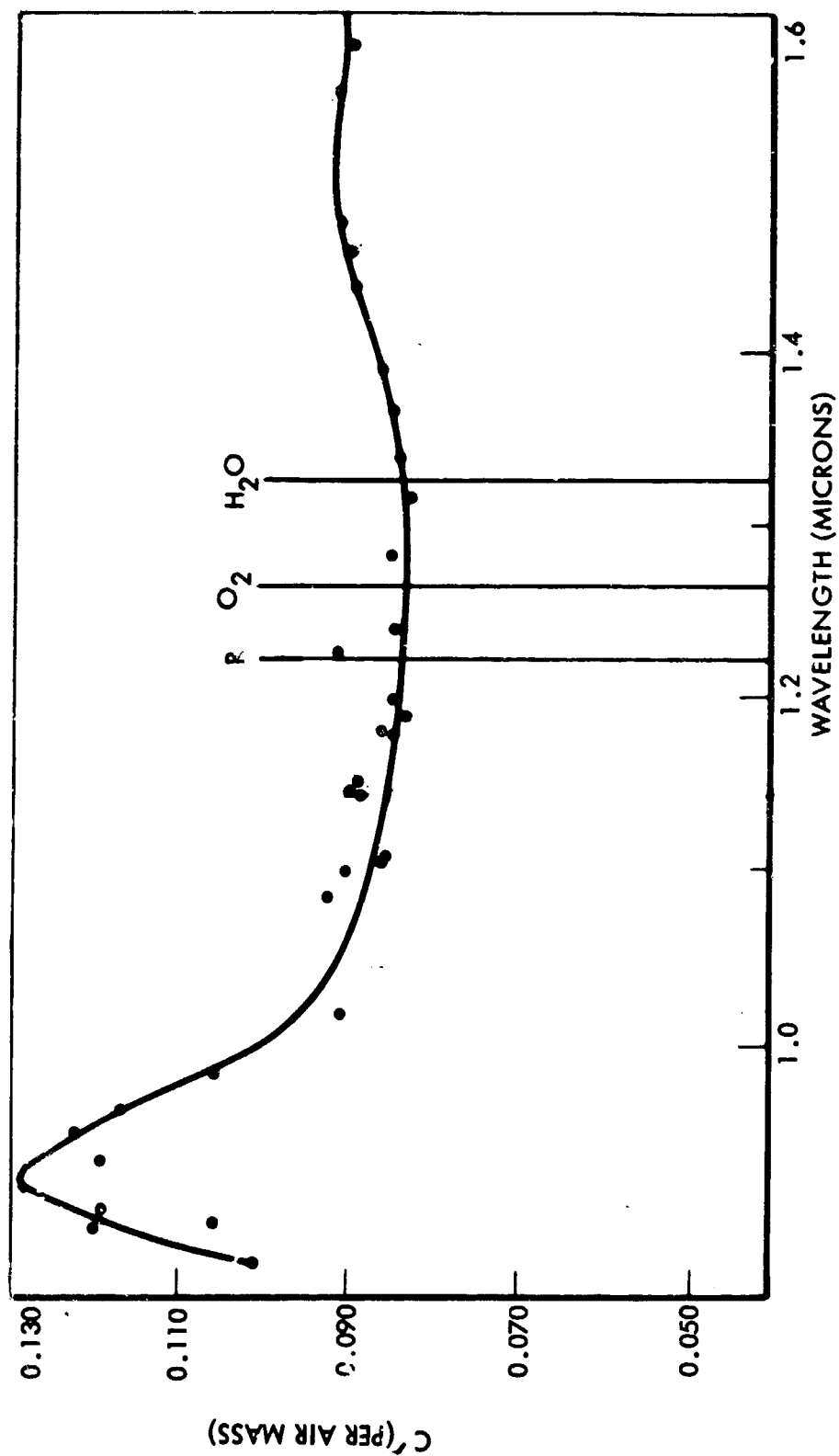


Figure 20: THE INFRARED CONTINUUM EXTINCTION COEFFICIENT AS A FUNCTION OF WAVELENGTH

to-absorption-ratio mode of operation, the continuum extinction effects (as compared to line-broadening effects) on the degradation of the integrated water-vapor and oxygen density data are negligible.

(B) Effects of the continuum spectrum — Microwave continuum.

At microwave frequencies, the continuum spectrum of greatest concern is that presented by the occurrence of clouds. Deirmendjian has calculated cloud extinction coefficients as a function of microwave wavelength, assuming representative cloud models as regards droplet-size distributions and concentrations (Reference 55). The results are shown in Figure 21. Also indicated are the ordinates denoting the water-vapor absorption band and its reference, and the oxygen band and its reference.

Contrary to Figure 20, the data contained in Figure 21 indicate a pronounced dependence of extinction coefficient on wavelength. However, from the figure, the difference in extinction coefficients at the wavelengths of the water-vapor-absorption and reference bands is calculated as

$$\frac{\Delta \tau_w}{\tau_w} \approx [0.003 - 0.001] = 0.002 \quad (159)$$

and that between the oxygen-absorption and reference bands as

$$\frac{\Delta \tau_{o_2}}{\tau_{o_2}} \approx [0.020 - 0.002] = 0.018 \quad (160)$$

Even multiplying the right-hand side of Equation 159 by two, in accordance with the dictates of Figure 19, the relative error in (ρ_w/τ) , attributable to the cloud continuum extinction is still an order of magnitude less than the previously specified error associated with line-broadening effects. Therefore, the error may be neglected.

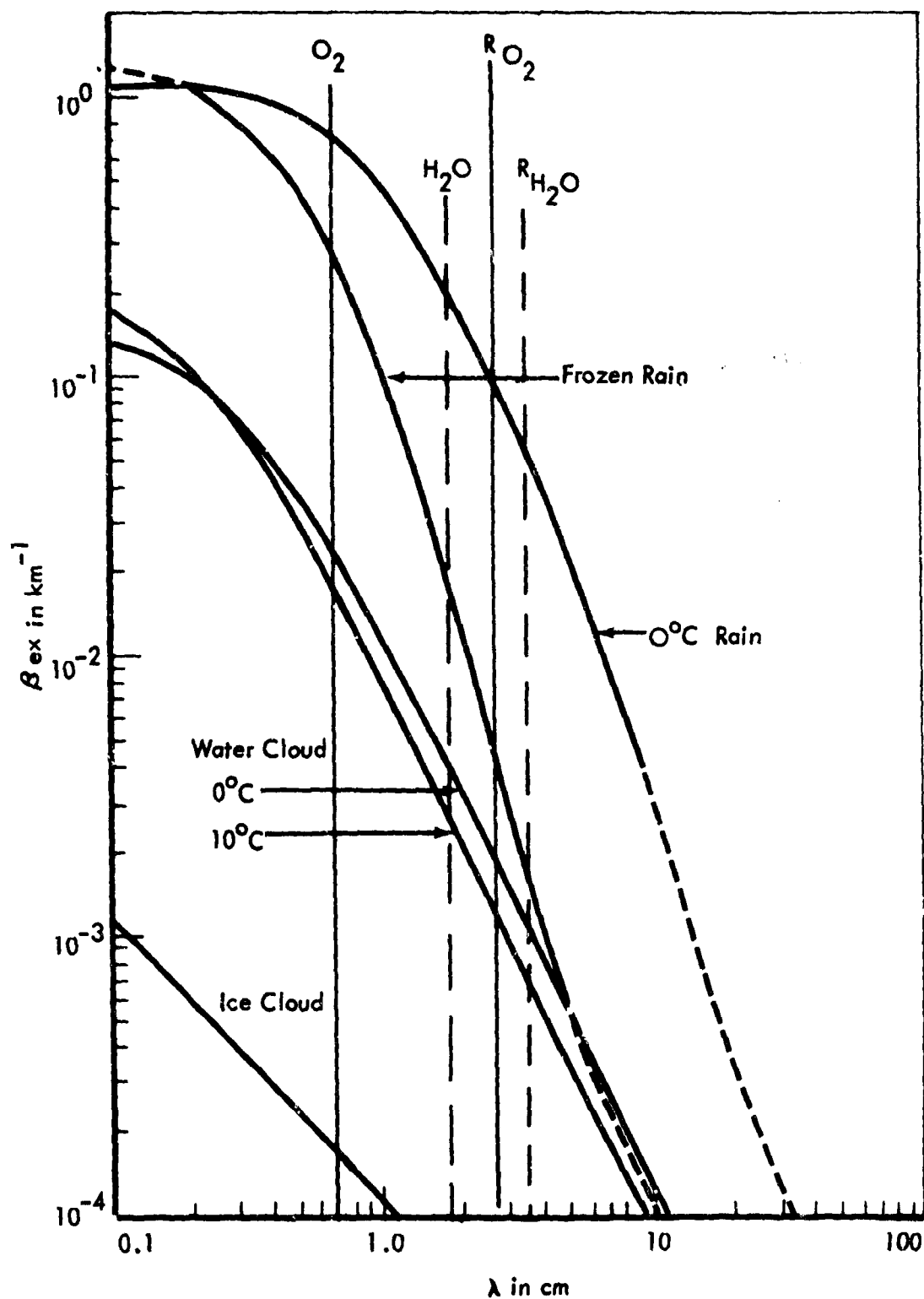


Figure 21: COMPUTED EXTINCTION CURVES FOR CLOUD AND PRECIPITATION AS A FUNCTION OF THE WAVELENGTH (After Deirmendjian, 1963)

In the case of oxygen, however, twice the extinction coefficient difference implies a relative error in (ρ_{O_2}/T) measurement of better than 1 percent. The oxygen continuum extinction error therefore should not be dismissed, but rather attempts should be made to actually correct the data. Suppose, as suggested by Deirmendjian, the cloud continuum extinction coefficient is expressed as (Reference 55)

$$c(\lambda) = A \lambda^{-q} \quad (161)$$

where A is a parameter depending on the physical composition (i.e., cloud-drop-let-size distribution, concentration, etc.) of the actual clouds extant, and q is a constant. Goldstein (Reference 56) suggests the value $q = 2$. Suppose further that the ratio between the two microwave reference signals is acquired along with the sensing-to-reference signals. Then, in line with Equation 155

$$\frac{I_{ref1}}{I_{ref2}} = K_{ref} \cdot \frac{\tau_{c1}}{\tau_{c2}} \quad (162)$$

where K_{ref} denotes the ratio of the intrinsic source energy at the first reference wavelength to that at the second reference wavelength, and τ_{c1} and τ_{c2} denote the corresponding continuum transmittances. From the Bouguer extinction law it also follows that

$$\ln \frac{\tau_{c1}}{\tau_{c2}} = \ln \left(\frac{1}{K_{ref}} \cdot \frac{I_{ref1}}{I_{ref2}} \right) = [c(\lambda_2) - c(\lambda_1)] \quad (163)$$

The right-hand side of Equation 163, may, by virtue of Equation 161, be redefined to yield

$$\ln \left(\frac{1}{K_{ref}} \cdot \frac{I_{ref1}}{I_{ref2}} \right) = A (\lambda_2^{-q} - \lambda_1^{-q}) \quad (164)$$

and, therefore,

$$A = \frac{1}{(\lambda_2^{-q} - \lambda_1^{-q})} \cdot \ln \left(\frac{1}{K_{ref}} \cdot \frac{I_{ref1}}{I_{ref2}} \right). \quad (165)$$

Thus, measurement of the ratio of the reference-signal intensities suffices to evaluate the parameter A required for estimating the continuum extinction coefficient, in accordance with Equation 161, for any wavelength. The right-hand side of Equation 158 is thus quantified, and the numerical value of the percentage error in τ_a measurement is established. The τ_a data, as defined by Equation

155, may therefore be corrected appropriately, probably to within 10 percent of the value given in Equation 160. The residual error in τ_{o_2} would thus be something more like

$$\frac{\Delta \tau_{o_2}}{\tau_{o_2}} \simeq 0.0018 \quad (166)$$

One further advantage may be gained from measuring the ratio of the microwave reference signals. The percentage error in oxygen-absorption measurement thereby established defines the magnitude of the cloud continuum transmittance. In turn, this transmittance is a function of (and therefore provides a measure of) the liquid water content of the cloud (Reference 56). Knowledge of the cloud's liquid water content will permit estimation of the contribution to line-integrated refractivity established by the cloud droplets themselves.

(C) Effects of mean-temperature specification errors

When microwave oxygen measurements are performed, the acquired data, to yield the correct form of the oxygen term in the N-equation, must be operated on in accordance with Equation 112. That is, the integrated oxygen-absorption coefficient must be multiplied by the mean temperature to obtain the desired integrated oxygen density:

$$\bar{P}_{o_2} = \langle T \rangle \left(\frac{\bar{P}_{o_2}}{\bar{T}} \right) \quad (167)$$

An additional source of error in \bar{P}_{o_2} specification thus becomes evident; consider that

$$\Delta \bar{P}_{o_2} = \langle T \rangle \Delta \left(\frac{\bar{P}_{o_2}}{\bar{T}} \right) + \left(\frac{\bar{P}_{o_2}}{\bar{T}} \right) \Delta (\langle T \rangle) \quad (168)$$

An error in $\langle T \rangle$ measurement, therefore, also contributes to an error in \bar{P}_{o_2} specification. Specifically the $\langle T \rangle$ -caused relative error in \bar{P}_{o_2} is precisely that of the $\langle T \rangle$ error itself; i.e.,

$$\frac{\Delta \bar{P}_{o_2}}{\bar{P}_{o_2}} = \frac{\Delta (\langle T \rangle)}{\langle T \rangle} \quad (169)$$

In effect, Equation 169 constitutes an additional term that must be added to the right-hand side of Equation 145 to completely specify the error in \bar{P}_{o_2} measurement under cloudy conditions. The magnitude of Equation 169 would more than

likely contribute an additional percentage of error in \bar{P}_{o_2} . That is, the mean-temperature specification error would result in

$$\frac{\Delta \bar{P}_{o_2}}{\bar{P}_{o_2}} \simeq 0.01 \quad (170)$$

The above estimate implies a $\Delta(\langle T \rangle)$ error of order $\pm 3^\circ\text{K}$.

(D) Scintillation effects

Intensity (and phase and amplitude) scintillations of signals received from remote energy sources are caused by the scattering of direct waves by random inhomogeneities in the atmospheric refractive index field. To good approximation, the inhomogeneities can be treated as equivalent optical elements, and the relative signal fluctuations caused by them explained by the Born single-scattering solution to the Schroedinger wave equation. Using this approach, Wheelon, for the case of a plane wave falling on a turbulent medium in which is immersed an upward-looking receiver (Figure 22), presents the following expression for the variance of the relative intensity fluctuation (Reference 57)

$$\left(\frac{\Delta I}{I}\right)^2 = \frac{2\pi L}{\lambda^2} \int_0^\infty k S(k) \Phi\left(\frac{k^2 \lambda L}{2\pi}\right) dk \quad (171)$$

where L is the atmospheric path through turbulence (Figure 22), λ is the wavelength of the propagated energy; where k now denotes the wave number of the turbulent refractive index eddies, $S(k)$ denotes the spectrum of that turbulence. Note once more that the left-hand side of Equation 171 defines precisely the terms on the right-hand side of Equation 156, which are now required to estimate scintillation effects on τ_a measurement.

The function

$$\Phi(x) = \frac{x^2}{2(1+x^2)} + O\left(\frac{1}{kL}\right) \quad (172)$$

attains its physical significance through recognition that $k^2 \lambda L$ is the scattering parameter $\mathcal{N} = \lambda L / l^2$ (where $k = 1/l$, with l the linear dimension of the turbulent eddies) appropriate to each eddy size in the hierarchy described by $S(k)$. The eddies that are large compared with \mathcal{N} give Fresnel scattering, whereas large values of \mathcal{N} correspond to Fraunhofer scattering. Equation 172 in

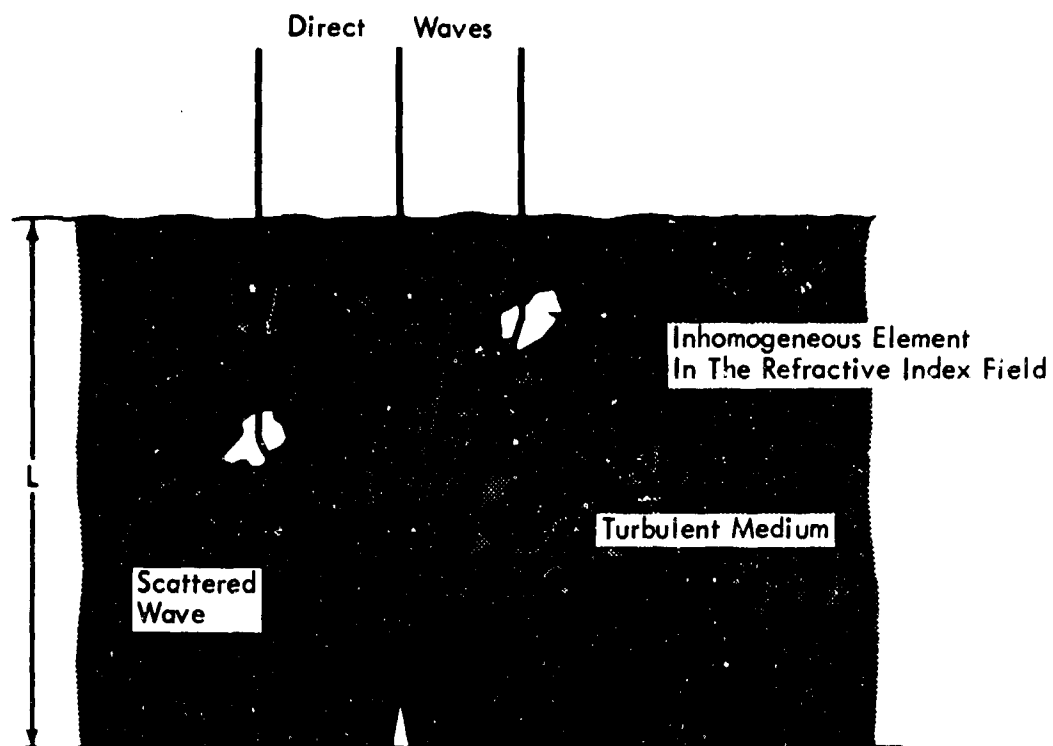


Figure 22: SCATTERING BY REFRACTIVE INDEX INHOMOGENEITIES AS THE CAUSE OF SCINTILLATION IN THE IDEALIZED LINE-OF-SIGHT PROBLEM OF A SOURCE VIEWED UPWARD THROUGH A TURBULENT MEDIUM

combination with 171 establishes the following limiting expressions for the variance in intensity fluctuations:

$$\left(\frac{\Delta I}{I}\right)^2 = \frac{L^3}{4\pi} \int_0^\infty k^3 S(k) dk, \text{ when } k^2 \ll \frac{1}{L\lambda} \quad (173)$$

and

$$\left(\frac{\Delta I}{I}\right)^2 = \frac{4\pi L}{\lambda^2} \int_0^\infty k S(k) dk, \text{ when } k^2 \gg \frac{1}{L\lambda} \quad (174)$$

The Fresnel approximation of Equation 173 will always be valid for λ of infrared wavelengths, whereas the Fraunhofer approximation of Equation 174 must be considered if λ is of microwave wavelengths. Thus, the variance of the relative intensity fluctuations at infrared wavelengths is (to good approximation) given by the cube of the path through turbulence, times the integral, over all wavenumber magnitudes of the third moment of the refractive index spectrum. No explicit dependence on wavelength is indicated. At microwave wavelengths, however, such a wavelength dependence is indicated, with the variance in relative intensity varying as the reciprocal of wavelength squared times turbulence path length to the first power times the integral of the first moment of the refractive index spectrum. Each case will be considered separately.

1. Scintillation at infrared wavelengths

For analytical purposes, a Gaussian refractive index correlation function

$$c(s) = e^{-\frac{s^2}{l_0^2}} \quad (175)$$

may be assumed. The associated spectrum is

$$S(k) = \pi^{3/2} \langle (\Delta n)^2 \rangle l_0^3 e^{-\frac{l_0^2}{4} k^2} \quad (176)$$

where $\langle (\Delta n)^2 \rangle$ is the variance of the refractive index fluctuations Δn . The resulting elementary integration called for by Equation 173 may now be performed to yield

$$\left\langle \left(\frac{\Delta I}{I}\right)^2 \right\rangle_{IR} = \frac{2\pi^{3/2} L^3}{l_0} \langle (\Delta n)^2 \rangle_{IR} \quad (177)$$

where l_0 denotes the turbulence length scale. The relative intensity variance is thus related to the variance in the refractive index. The standard deviation of relative intensity is thus

$$\left\langle \left(\frac{\Delta I}{I} \right)^2 \right\rangle_{IR}^{1/2} = \left(\frac{2\pi k L^3}{\ell_0} \right)^{1/2} \langle (\Delta n)^2 \rangle_{IR}^{1/2} \quad (178)$$

and if the refractive index fluctuations are assumed to be normally distributed, an average intensity fluctuation can be calculated as

$$\left\langle \frac{\Delta I}{I} \right\rangle_{IR} = \left(\frac{2\pi k L^3}{\ell_0} \right)^{1/2} \frac{5}{4} D(n)_{IR} \quad (179)$$

where $D(n)$, the mean deviation, is taken as 4/5 the standard deviation. According to Equation 156 then, scintillation-caused transmittance errors are dependent on the difference between sensing and reference-band mean deviations in refractive index. Specifically,

$$\left(\frac{\Delta T_a}{T_a} \right)_{IR} = \left[\frac{25\pi k L^3}{16 \ell_0} \right]^{1/2} \left[D(n)_{IR_{sens}} - D(n)_{IR_{ref}} \right] \quad (180)$$

As compared to temperature and pressure influences, water vapor only slightly affects refractive index at infrared wavelengths. Edlen (Reference 58) expresses refractive index for any atmospheric state in terms of n in standard air as

$$(n-1)_\lambda = (n_s-1)_\lambda \cdot f(p, T) \quad (181)$$

Incremental changes in n due to turbulence in the pressure and temperature fields would, therefore, be estimated from

$$\Delta n = (n_s-1)_\lambda \left[\frac{\partial f}{\partial p} \Delta p + \frac{\partial f}{\partial T} \Delta T \right] \quad (182)$$

The function $f(p, T)$ is not wavelength-dependent, so the ratio of n -fluctuations at different wavelengths would simply be as the ratio of standard-air refractive indices. Mean deviations would show the same relationship so that

$$\frac{D(n)_{IR_{sens}}}{D(n)_{IR_{ref}}} = \frac{(n_s-1)_{IR_{sens}}}{(n_s-1)_{IR_{ref}}} = \frac{N_{IR_{sens}}}{N_{IR_{ref}}} \quad (183)$$

and, therefore,

$$D(n)_{IR_{sens}} - D(n)_{IR_{ref}} = D(n)_{IR_{ref}} \left(\frac{N_{IR_{sens}}}{N_{IR_{ref}}} - 1 \right) \quad (184)$$

Considering the sensing and reference infrared wavelengths "as specified" Edlen's normal dispersion formula indicates that the refractivity ratio in the parenthesis on the right-hand side of Equation 184 will differ from unity in about the fourth decimal place. Therefore,

$$\left[D(n)_{IR_{sens}} - D(n)_{IR_{ref}} \right] \sim 10^{-4} D(n)_{IR_{ref}} \quad (185)$$

At visible wavelengths, Reiger reports a turbulence-generated standard deviation in n of about 3×10^{-8} (Reference 59). This estimate is based partly on measurement and partly by inference from scintillation data. The mean deviation of refractive index will also be on the order of 10^{-8} , and the final order-of-magnitude estimate for the difference in infrared-sensing and reference-band mean deviations is thus

$$\left[D(n)_{IR_{sens}} - D(n)_{IR_{ref}} \right] \sim 10^{-12} \quad (186)$$

In view of the order of magnitude defined above, scintillation effects, through suitable instrument design (i.e., simultaneous sampling of all bands through a single aperture) can be reduced to negligible proportions in spite of the dependence of intensity scintillations on the $3/2$ - power of the atmospheric turbulence path. For if turbulence is considered to be confined mainly to altitudes below 10km, then even at a slant-path elevation of 1 degree, L will only be on the order of 10^2 km. The turbulence length scale, l_0 , is on the order of 10m (Reference 60). The coefficient of the mean deviation difference in Equation 180 is thus on the order of 10^7 . Thus

$$\left(\frac{\Delta n_a}{n_a} \right)_{IR} \sim 10^{-5} \quad (187)$$

The implication contained in the order-of-magnitude Equation 187 is borne out by the work of Yates (Reference 6), wherein he could detect no scintillation dependence on wavelength in the infrared portion of the spectrum. His work, moreover, involved using one wavelength near the N_2O absorption band, where anomalous dispersion effects might be expected to augment the mean deviation differences stated in Equation 186. However, no such effect was noted.

2. Scintillation at microwave wavelengths

With the same Gaussian correlation function assumed for turbulence in the microwave refractive index, the integration called for in Equation 174 is performed to yield

$$\left(\frac{\Delta I}{I}\right)_{\mu\text{-wave}}^2 = \frac{8\pi^{5/2} \ell_o L}{\lambda^2} \langle (\Delta n)^2 \rangle_{\mu\text{-wave}} \quad (188)$$

Again with the mean deviation in n taken as 4/5 the standard deviation,

$$\left(\frac{\Delta I}{I}\right)_{\mu\text{-wave}} \approx \left(\frac{25\pi^{5/2} \ell_o L}{2}\right)^{1/2} \cdot \frac{1}{\lambda} \cdot D(n)_{\mu\text{-wave}} \quad (189)$$

Therefore, from Equation 156

$$\left(\frac{\Delta \tau_a}{\tau_a}\right)_{\mu\text{-wave}} = \left(\frac{25\pi^{5/2} \ell_o L}{2}\right)^{1/2} \left[\frac{D(n)_{\mu\text{-wave sens}}}{\lambda_{\text{sens}}} - \frac{D(n)_{\mu\text{-wave ref}}}{\lambda_{\text{ref}}} \right] \quad (190)$$

Arguing as before in developing Equation 183, the mean deviation in the sensing-band refractive index can be expressed in terms of $D(n)_{\text{ref}}$ times the ratio of refractivity at the two wavelengths. Therefore,

$$\left(\frac{\Delta \tau_a}{\tau_a}\right)_{\mu\text{-wave}} = \left(\frac{25\pi^{5/2} \ell_o L}{2}\right)^{1/2} D(n)_{\mu\text{-wave}} \left[\frac{\left(\frac{N_{\mu\text{-wave sens}}}{N_{\mu\text{-wave ref}}} - 1\right)}{\lambda_{\text{sens}}} - \frac{1}{\lambda_{\text{ref}}} \right] \quad (191)$$

There is no normal dispersion at microwave frequencies, so the only factor that makes the refractivity ratio in Equation 191 different from unity is the effect of anomalous dispersion. Sullivan (Reference 62) points out that such anomalous dispersion effects result in differences in refractivity across an absorption band on the order of 10^{-2} . The ratio of refractivities at frequencies within and outside such bands will be on the order of 10^{-3} . Equation 191 may thus be approximated as

$$\left(\frac{\Delta \tau_a}{\tau_a}\right)_{\mu\text{-wave}} \approx \left(\frac{25\pi^{5/2} \ell_o L}{2}\right)^{1/2} D(n)_{\mu\text{-wave}} \left[- \frac{\lambda_{\text{ref}} + \lambda_{\text{sens}}}{\lambda_{\text{ref}} \lambda_{\text{sens}}} \right] \quad (192)$$

With the sensing and reference wavelengths indicated in Figure 21, the term in brackets on the right-hand side of Equation 192 is on the order of 10^0 .

Therefore, again accepting the value 10^{-8} as the mean deviation in refractive index at the reference wavelength, it may be stated that

$$\left(\frac{\Delta \tau_a}{\tau_a}\right)_{\mu\text{-wave}} \approx \left(\frac{25\pi^{5/2} \ell_o L}{2}\right)^{1/2} \cdot 10^{-8} \quad (193)$$

Postulating the values for ℓ_o and L mentioned in conjunction with the analysis of the Fresnel scattering, the final order-of-magnitude estimate is obtained as shown below:

$$\left(\frac{\Delta \tau_a}{\tau_a}\right)_{\mu\text{-wave}} \approx 10^{-6} \quad (194)$$

Again, the (\bar{P}/T) -specification error associated with γ measurement errors of the orders shown above are negligible in comparison with the errors arising from line-broadening effects. The fact that scintillation has even less impact on γ measurement at microwave wavelengths than at infrared wavelengths (in spite of the explicit microwave scintillation wavelength dependence) is ascribable to the much weaker effect of turbulence path length at microwave frequencies.

(5) Considerations of passive operational mode

The above error analysis is derived when considering an active system. Because of the basic connection at any frequency between absorption and emission, however, the results can be applied directly to the case of passive systems, except for the scintillation effect. Scintillation phenomena do not affect sky brightness temperature measurements, and consideration of them may be dismissed entirely. Line-broadening effects on emission (i.e., sky brightness temperature) measurements, however, are the same as on transmittance measurements. And insofar as only microwaves are utilized in the passive mode, the continuum effects are similarly the same. This follows because the microwave continuum is that presented by clouds, and the process that establishes it is absorption.

(6) Cumulative \bar{N} error

Assuming the line-broadening, the continuum extinction, the scintillation, and the $\langle T \rangle$ -specification errors in \bar{P} specification to be uncorrelated, then the total rms value of $\Delta\bar{P}$ or of $\Delta(\bar{P}/T)$ can be considered to consist of the square root of the sum of the variances in \bar{P} or $\Delta(\bar{P}/T)$ generated by each effect individually; i.e.,

$$\left[\Delta\left(\frac{\bar{P}}{T}\right) \right]^2 = \left\{ \left[\Delta\left(\frac{\bar{P}}{T}\right) \right]^2_{\text{line broadening}} + \left[\Delta\left(\frac{\bar{P}}{T}\right) \right]^2_{\text{continuum effect}} + \left[\Delta\left(\frac{\bar{P}}{T}\right) \right]^2_{\text{scintillation}} + \left[\Delta\left(\frac{\bar{P}}{T}\right) \right]^2_{\langle T \rangle \text{ specification}} \right\} \quad (195)$$

The above equation is an expansion of Equation 145, and defines the individual contributing effects to errors in \bar{P} or (\bar{P}/T) . The first two terms on the right-hand side of Equation 195 are active contributors to errors, regardless of the configuration of the radiometric system; i.e., active-hybrid IR/microwave

system, all-microwave active system, or the passive system. The third term contributes error only in the active mode of operation, and the fourth term only when microwave absorptions are measured to determine values of $\bar{\rho}$ from $(\bar{\rho}/T)$ data. The last term thus applies to the cloudy-weather active system or to the passive system. The magnitudes of the various contributions to the total variance in $\bar{\rho}$ or $(\bar{\rho}/T)$ -specification are summarized in Table 8.

The variance shown in Table 8, estimated according to the dictates of Figure 19 from the previously specified relative errors in $\bar{\rho}$ -measurement, are listed by contributing effects applicable to the different radiometric measurement system configurations. The total variance listed at the bottom of each column represents the column sum in accordance with Equation 195. The rms value is simply the square root of total variance. The associated rms line-integrated refractivity errors for one standard air mass are listed in Table 9. The values listed were computed in accordance with Equation 133, after defining \bar{N} for one standard air mass in accordance with the standard conditions listed in Paragraph 6. B. and Equation 135.

Note, from Table 8, that the line-broadening effect is the biggest contributor to \bar{N} errors in the hybrid system. In both the all-microwave active and passive systems, the biggest contributor is the effect of error in the $\langle T \rangle$ -specification.

D. Residual errors in slant range and elevation angle

(1) Basic residual error equations

In Paragraph 2. A., ΔS was considered the atmospheric contribution to slant range. Considering that the uncertainty in the specification of ΔS constitutes the residual slant range error, then from Equation 9, by differentiation,

$$\Delta(\Delta S) = 10^{-6} \Delta \bar{N} \quad (196)$$

where $\Delta(\Delta S)$, the error of estimate of the atmospheric range contribution, denotes residual error.

Table 8: Relative Errors in \bar{p} and (\bar{p}/T) Specifications per Unit Standard Air Mass Ascribable to Atmospheric Effects on Different Radiometric System Configurations

| Mechanism Contributing to Measurement Error | Variance in Relative Error per Unit Air Mass | | | | | |
|---|--|--------------------------------------|--|--|--------------------------------------|--|
| | Active Hybrid (Clear-Weather) | | Active Microwave (Cloudy-Weather) | | Passive | |
| | $\frac{\Delta \bar{p}_{O_2}}{\bar{p}_{O_2}}$ | $\frac{\Delta \bar{p}_w}{\bar{p}_w}$ | $\frac{\Delta (\frac{\rho}{T})}{(\frac{\rho}{T})}$ | $\frac{\Delta \rho_{O_2}}{\rho_{O_2}}$ | $\frac{\Delta \bar{p}_w}{\bar{p}_w}$ | $\frac{\Delta (\frac{\rho_w}{T})}{(\frac{\rho_w}{T})}$ |
| Line-Broadening | 2.5×10^{-5} | 2.5×10^{-3} | 2.5×10^{-3} | 2.5×10^{-5} | 2.5×10^{-3} | 2.5×10^{-3} |
| Continuum Extinction | 2×10^{-6} | 2×10^{-6} | | 1.3×10^{-5} | 1.6×10^{-5} | 1.6×10^{-5} |
| Scintillation | 2×10^{-10} | 2×10^{-10} | 2×10^{-12} | 2×10^{-10} | 2×10^{-10} | |
| < T > -Specification | | | | 2×10^{-4} | 2×10^{-4} | |
| Total Variance | 2.7×10^{-5} | 2.5×10^{-3} | 2.5×10^{-3} | 2.38×10^{-4} | 2.72×10^{-3} | 2.52×10^{-3} |
| Total rms Value | 5.19×10^{-3} | 5.0×10^{-2} | 5×10^{-2} | 1.54×10^{-2} | 5.22×10^{-2} | 5.02×10^{-2} |

Table 9: \bar{N} -specification Errors (per Unit Standard Air Mass) Ascribable to Atmospheric Effects on Different Radiometric System Configurations

| RMS \bar{N} -error per Air Mass | Radiometric System | | |
|--------------------------------------|----------------------------------|--------------------------------------|--------------------|
| | Active Hybrid (Clear-Weather) | Active Microwave (Cloudy Weather) | Passive |
| Absolute Error (Meters) | 1.32×10^4 | 3.54×10^4 | 3.54×10^4 |
| Relative Error (Percent) | 0.54 | 1.47 | 1.47 |

In a similar manner, $\Delta\epsilon$ was considered the atmospheric contribution to elevation angle. The residual elevation-angle error in interferometric tracking operations (Figure 3) can be obtained from differentiation of Equation 18. The result is, in finite increment form:

$$\Delta(\Delta\epsilon) = \csc 2\epsilon \left[\sin \phi_1 \Delta(\Delta\phi_1) + \sin 2\phi_2 \Delta(\Delta\phi_2) \right] \quad (197)$$

where the $\Delta(\Delta\phi_i)$ denote residual errors in the interferometer angles.

(2) Error estimates

(A) Slant range

The magnitude of the residual slant-range error is, by Equation (196), linearly related to the magnitude of the error in line-integration refractivity. The \bar{N} error, furthermore, is linearly related to the air mass value. Air mass is simply the length of the atmospheric path traversed by a ray (emanating from a source entirely outside the atmosphere) in reaching the Earth, measured in terms of this path when the source is at the zenith. The air mass value to be assigned the atmospheric path between a radar and a target thus varies with (1) target elevation angle, and (2) target altitude so long as the target is within the atmosphere. The air-mass variation with elevation angle is shown in Figure 23. From the data contained in Figure 23, the air-mass variation with target altitude can be estimated from

$$m(\epsilon_o, h) = m(\epsilon_o) - m(\epsilon_1) \left[1 - \frac{p(h_1)}{p_o} \right] \quad (198)$$

where $m(\epsilon_o, h)$ is the air-mass value of the atmospheric path in the direction ϵ_o to target height h_1 , $m(\epsilon_o)$ is the air mass for the total atmospheric path air mass in the direction ϵ_o , $p(h_1)$ is the atmospheric pressure at height h_1 and p_o is the surface pressure. The value $m(\epsilon_1)$ is the total atmospheric path air mass in the direction ϵ_1 , where ϵ_1 , the local line-of-sight elevation at the target, is given by

$$\epsilon_1 = 90 - \cos^{-1} \left[\frac{S^2 + h_1(2r + h_1)}{2S(r + h_1)} \right] \quad (199)$$

The geometry of the problem is as shown in Figure 24. Equation 198 simply states that air mass between radar and target is given by the difference between the total air mass and the air mass above the target.

The geometrical relationships between target altitude, slant range, and elevation angle are shown by the set of dashed curves in Figure 25. The curves are labeled by target altitude in kilometers, the ordinate labels are slant ranges in miles, and the abscissa labels are elevation angles. The top of the effective atmosphere is considered to be at an altitude of 40 kilometers. With the curves, know-

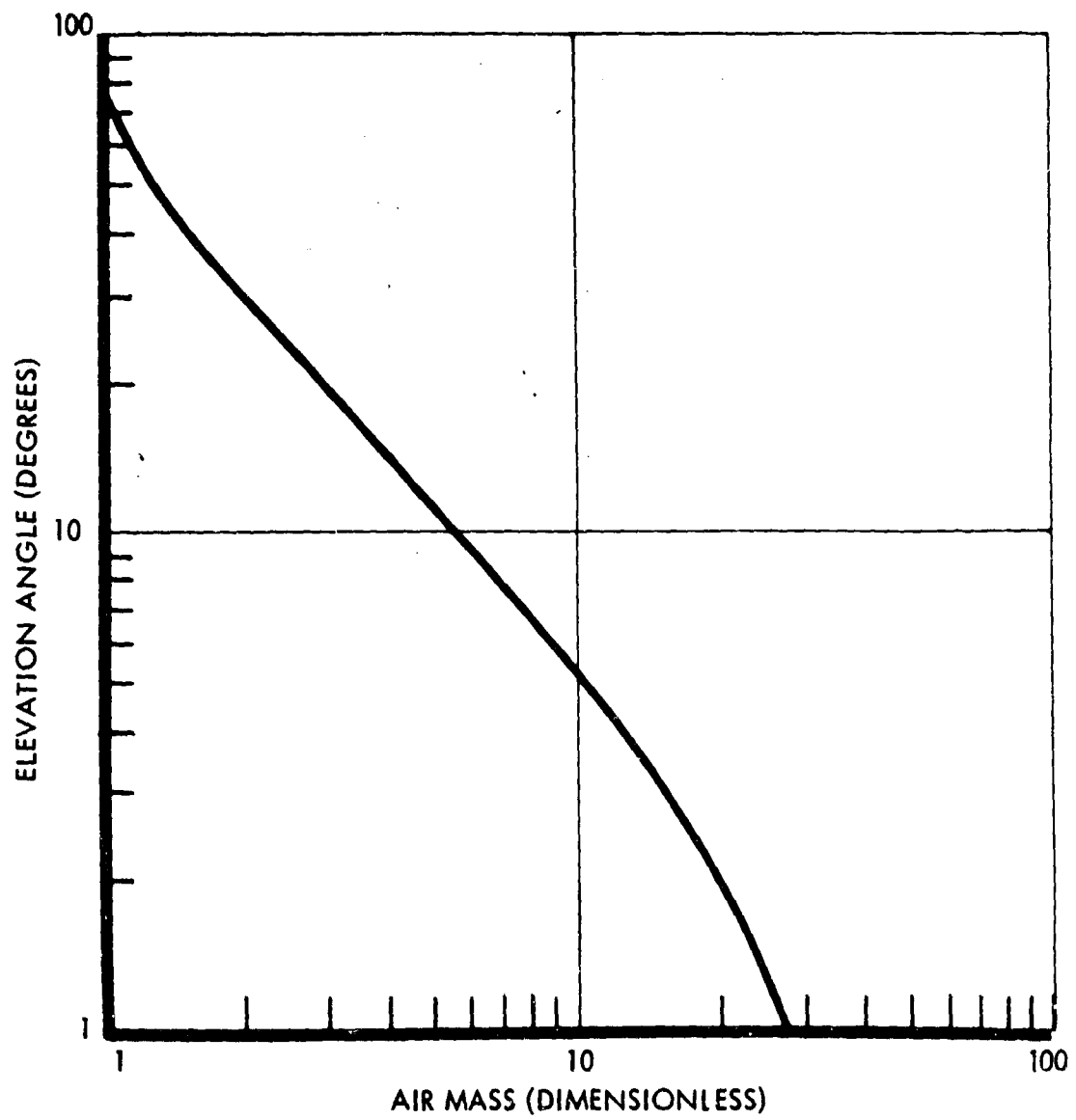


Figure 23: AIR MASS AS A FUNCTION OF ELEVATION ANGLE

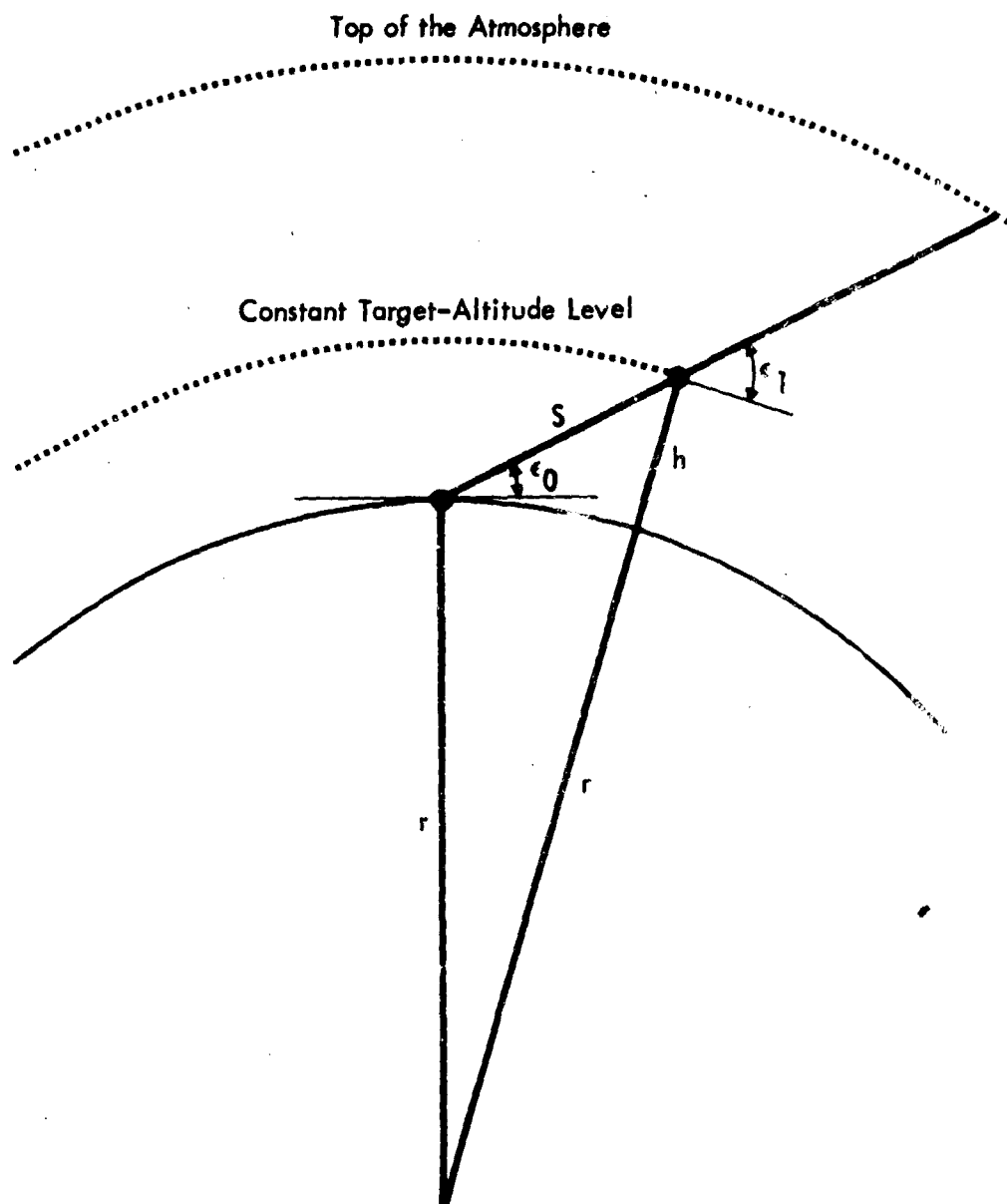


Figure 24: THE GEOMETRY RELATING TO SPECIFICATION OF AIR MASS AS A FUNCTION OF TARGET ALTITUDE

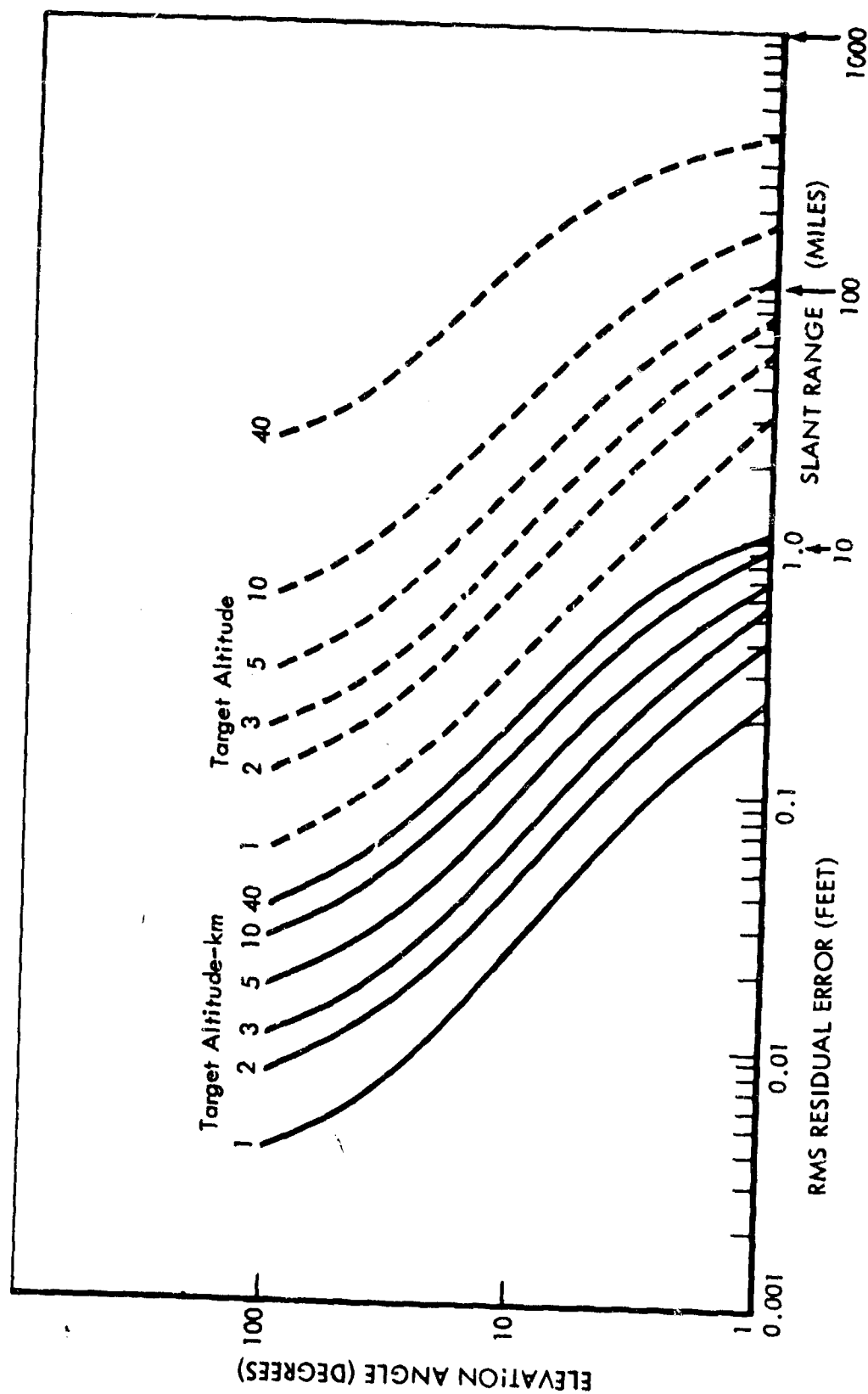


Figure 25: ROOT-MEAN-SQUARE RESIDUAL SLANT-RANGE ERROR NOMOGRAM

ledge of any two range parameters permits determination of the third. For example, the slant range at a 10 degree elevation angle to a target at 10-kilometers altitude would be about 34 miles. This is determined by following the 10 degree abscissa to its intersection with the 10-kilometer target altitude and noting the ordinate that also intersects this point. Similarly, a target at an altitude of 40 kilometers (the top of the atmosphere) 100 slant-range miles away would be viewed at an elevation angle of about 13 degrees. This is determined by following the 100-mile ordinate to its intersection with the 40 kilometer target altitude and noting the value of the abscissa that also intersects the point.

The geometrical relationships defined by the dashed curves in Figure 25 were used first to define, in accordance with Figure 23 and Equation 198, the air-mass value to be assigned the slant path in any direction to any altitude. Then, invoking the linear relationship between air mass and \bar{N} -measurement error, the defined air-mass values were multiplied by the absolute rms values per unit air mass contained in Table 9 to determine the corresponding residual slant-range errors. These data are plotted as the solid curves in Figure 25. Figure 25 can thus be used as a nomogram for determining the residual slant-range error associated with any receiver-to-target geometry. That is, the intersection of any abscissa with the solid and the dashed target altitude determines the slant range to the target and the residual error that would result if that slant range were measured with a radar and corrected with radiometrically acquired \bar{N} -data. For example, suppose a target at an altitude of 40 kilometers was viewed at a 10 degree elevation angle. The intersection of the 10 degree abscissa with the dashed 40-kilometer target altitude fixes the true range at about 130 miles, and its intersection with the 40-kilometer solid curves establishes about a 0.2-foot residual slant-range error. Therefore the radar-measured range would be $S = 130 \text{ miles} \pm 0.2 \text{ feet}$.

The data contained in Figure 25 were replotted in a different fashion in Figure 26. Ordinate labels are slant range in miles, abscissa labels are rms residual slant-range errors in feet, and the family of curves is labeled by slant-range elevation angle. For example, the slant-range residual error associated with a slant range of 30 miles to a target at 20 degrees elevation would be about 0.1 foot. This value is obtained by following the 30-mile slant-range

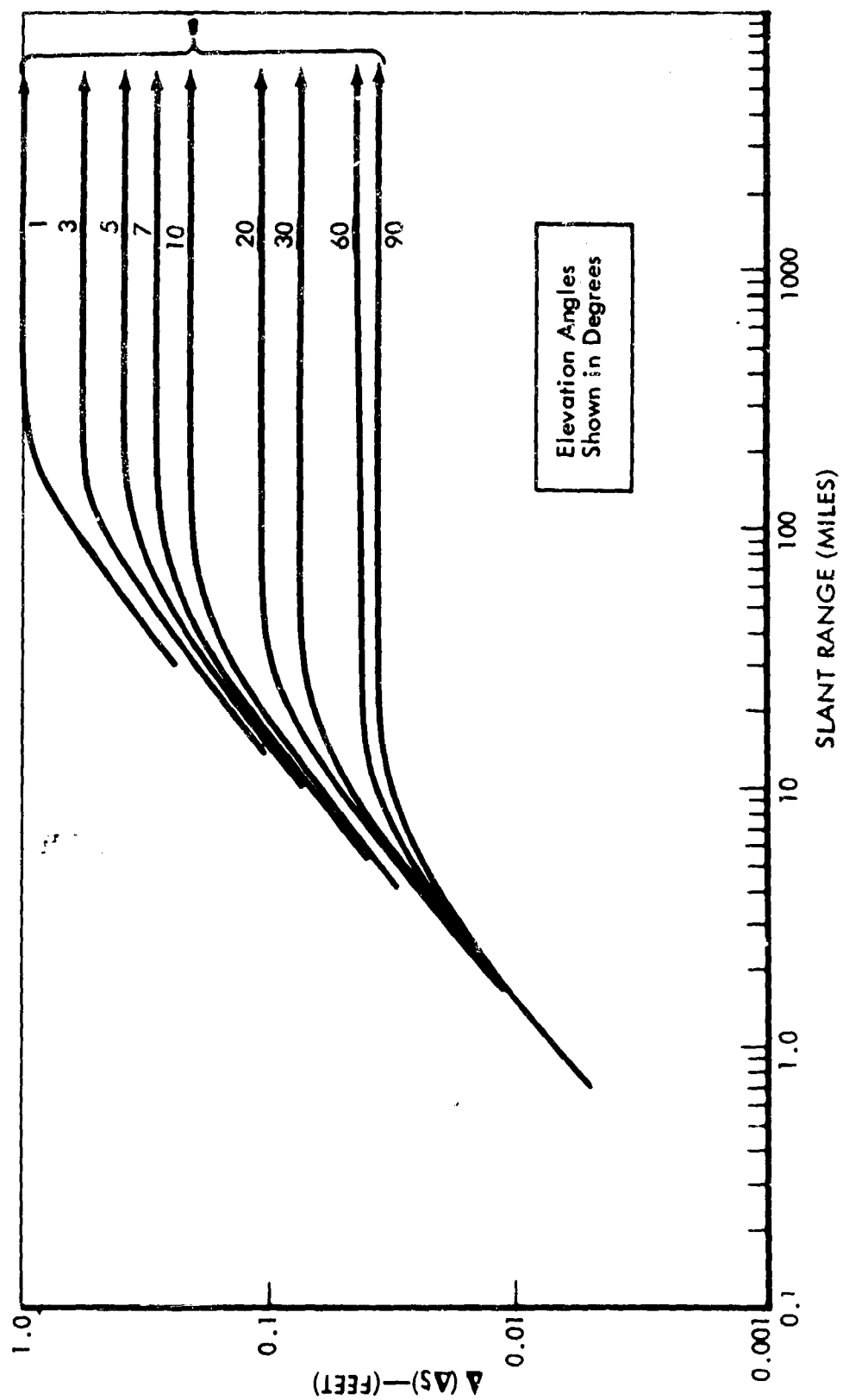


Figure 26: ROOT-MEAN-SQUARE RESIDUAL SLANT-RANGE ERRORS AS FUNCTIONS OF SLANT-RANGE AND ELEVATION ANGLE

ordinate to its intersection with the 20 degree curve and noting the abscissa that also intersects this point. For the same geometry, the same residual error could have been obtained from Figure 25. Figure 26 illustrates, however, that once the target leaves the atmosphere, the residual error is independent of slant range. For example, a target viewed at a 20 degree elevation angle 100 slant-range miles away is already beyond the atmosphere (i. e., at an altitude in excess of 40 kilometers). The residual error has already attained its maximum value (about 0.107 feet) and will stay at that value regardless of the increase in slant range.

It must be emphasized that the residual slant-range errors specified in Figures 25, 26, and 27 can only be considered as representative of actuality because they are based on consideration of a standard air mass. To recapitulate; a standard air mass has been defined as one in which pressure, temperature, and equivalent thickness are as defined by the U. S. Standard Atmosphere, and as one in which there is a total water content of 2.0 precipitable centimeters. A real atmosphere that departs from this standard will, of course, generate residual errors different from the ones specified.

It is further emphasized that the values presented are those that would be realized if slant-range data were corrected by using the hybrid-active-system line integral refractometer. Use of either the all-microwave active system or the passive system would result in residual errors about 2.5 times greater than those indicated above. For the latter system, the realization of a residual slant-range error only 2.5 times that attainable with the hybrid active system would be strictly true only for targets entirely outside the atmosphere. Targets imbedded in the atmosphere raise the problem of how well the contribution to \bar{N} from the atmosphere in front of the target, the only contribution that acts to establish Δ (ΔS) can be distinguished from that behind the target with systems of limited profiling capability. Of course, as emphasized in Paragraph 5. B. (2)(A), the more frequencies used in the profiling radiometer, the more detailed the measured profile. However, such a philosophy can be carried just so far, purely on the basis of economics. With just a four-channel radiometer, which permits the determination of \bar{N} to four different levels, the assumption simply of an exponential decrease of line-integrated refractivity with height between levels should result in no more than a 10-percent increase in the relative error in \bar{N} estimated to any

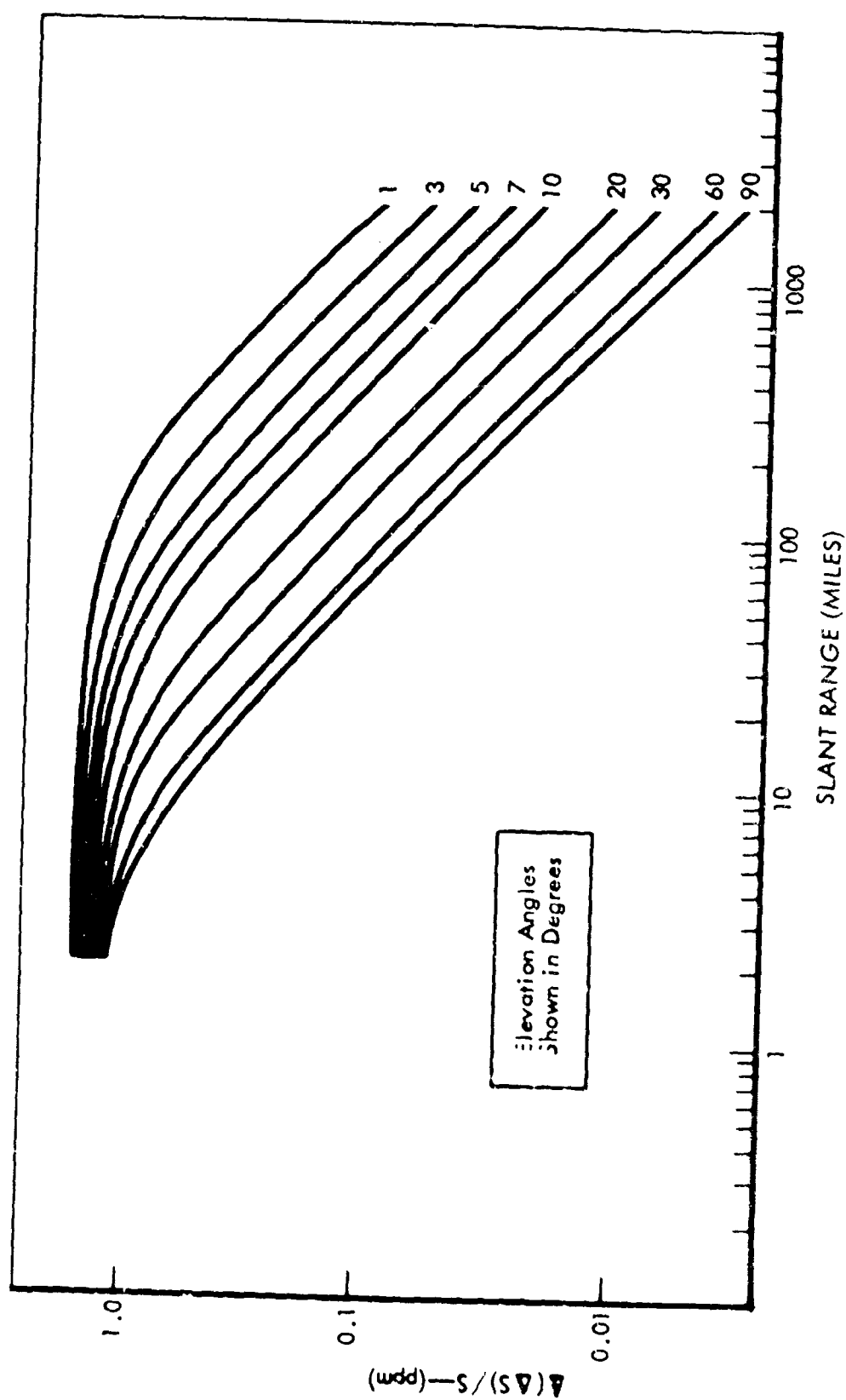


Figure 27: ROOT-MEAN-SQUARE RESIDUAL SLANT-RANGE ERRORS IN PARTS PER MILLION AS FUNCTIONS OF SLANT-RANGE AND ELEVATION ANGLE

point within that layer. Such an additional uncertainty would require multiplying the residual errors applicable to atmosphere-imbedded targets shown in Figures 25, 26, and 27 by a factor of three as opposed to 2.5.

(B) Elevation angle

To determine the residual elevation-angle error resulting from the residual errors in slant-range measurement, the ϕ -terms of Equation 197 must first be evaluated as dictated by Equations 11 and 12. Specifically, this would entail evaluations of such expressions as

$$\sin 2\phi_{1,2} = 2 \left\{ \frac{1}{B_{1,2}} \left[(S_0 - S_{1,2}) + \frac{B_{1,2}^2 - (S_0 - S_{1,2})^2}{2 S_0} \right] \cdot \sin \left(\cos^{-1} \left[(S_0 - S_{1,2}) + \frac{B_{1,2}^2 - (S_0 - S_{1,2})^2}{2 S_0} \right] \right) \right\} \quad (200)$$

and

$$\Delta(\Delta\phi_{1,2}) = \frac{1}{B_{1,2}} \left\{ \frac{[B_{1,2}^2 - (S_0^2 + S_{1,2}^2)]}{2 S_0^2} \Delta(\Delta S_0) + \frac{S_{1,2}}{S_0} \Delta(\Delta S_{1,2}) \right\} \csc \left\{ \cos^{-1} \left[(S_0 - S_{1,2}) + \frac{B_{1,2}^2 - (S_0 - S_{1,2})^2}{2 S_0} \right] \right\} \quad (201)$$

A bewildering complexity in the dependence of $\Delta(\Delta\epsilon)$ on the geometry of the problem is demonstrated. That is, different combinations of the three interferometer slant ranges — S_0 , S_1 , and S_2 — with their corresponding slant residuals — $\Delta(\Delta S_0)$, $\Delta(\Delta S_1)$, and $\Delta(\Delta S_2)$ — would result in different values for $\Delta(\Delta\epsilon)$. The specification of a particular combination for quantitative evaluation of Equation 197 is strictly arbitrary, and the results derived must be accepted as being only representative as to the order of magnitude in the $\Delta(\Delta\epsilon)$ that might be realized in actual ranging operations.

In making such a specification, (strictly as a matter of convenience to reduce the computational complexity of the problem) consider elevation-angle measurements to locus of points everywhere equidistant from the interferometric slave stations and at a constant elevation angle from the mother station. In this case $S_1 = S_2 = S$, $\phi_1 = \phi_2 = \phi$, and it may be assumed that $\Delta(\Delta\phi_1) \approx \Delta(\Delta\phi_2)$. If it is further considered that $B_1 = B_2 = B$, then Equation 197 reduces to

$$\sin 2\epsilon \Delta(\Delta\epsilon) = 2 \sin 2\phi \Delta(\Delta\phi) \quad (202)$$

Furthermore, Equation 18 may be written

$$\sin^2 \epsilon = 1 - 2 \cos^2 \phi \quad (203)$$

or

$$\cos^2 \epsilon = 2 \cos^2 \phi \quad (204)$$

Equation 202 thus defines the elevation angle in terms of the interferometer angle ϕ as defined by either equation 11 or 12. Equations 201, 202, and 204 thus permit a parametric study to determine $\Delta(\Delta\epsilon)$ as a function of slant range and slant-range residual for the geometry specified. The results for $B = 20$ miles are shown in Figure 28. Ordinate labels are slant range in miles as measured from the mother station; the abscissa labels are residual elevation angles in microradians. The family of curves is labelled by elevation angle. The data contained in Figure 28 is even less general than those contained in Figures 25, 26, and 27 because not only does the standard air mass restriction apply in this case, but the special geometry invoked for the parametric study must also be kept in mind. In spite of these restrictions, it is still safe to state that interferometrically determined elevation angles will be correct to orders of tens of microradians if the determining slant-range data are corrected through radiometric \bar{N} -measurement to the values shown in Figures 25, 26, and 27.

E. Summary

Regarding the determination of \bar{N} from spectrographic measurements of integrated oxygen and water-vapor absorption coefficients, two factors cause uncertainties in the final \bar{N} -specification. The first is related to uncertainties in the refractivity equation itself; the second is related to spectrographic measurement errors. The former effect is negligible compared to the latter.

Spectrographic measurement errors stem from (1) uncertainties in the functional relationships describing, for any portion of the electromagnetic spectrum, transmittance as a function of bandwidth; (2) pressure and temperature line-broadening effects; (3) continuum extinction effects; (4) scintillation effects; and (5) effects of errors in mean-temperature specification.

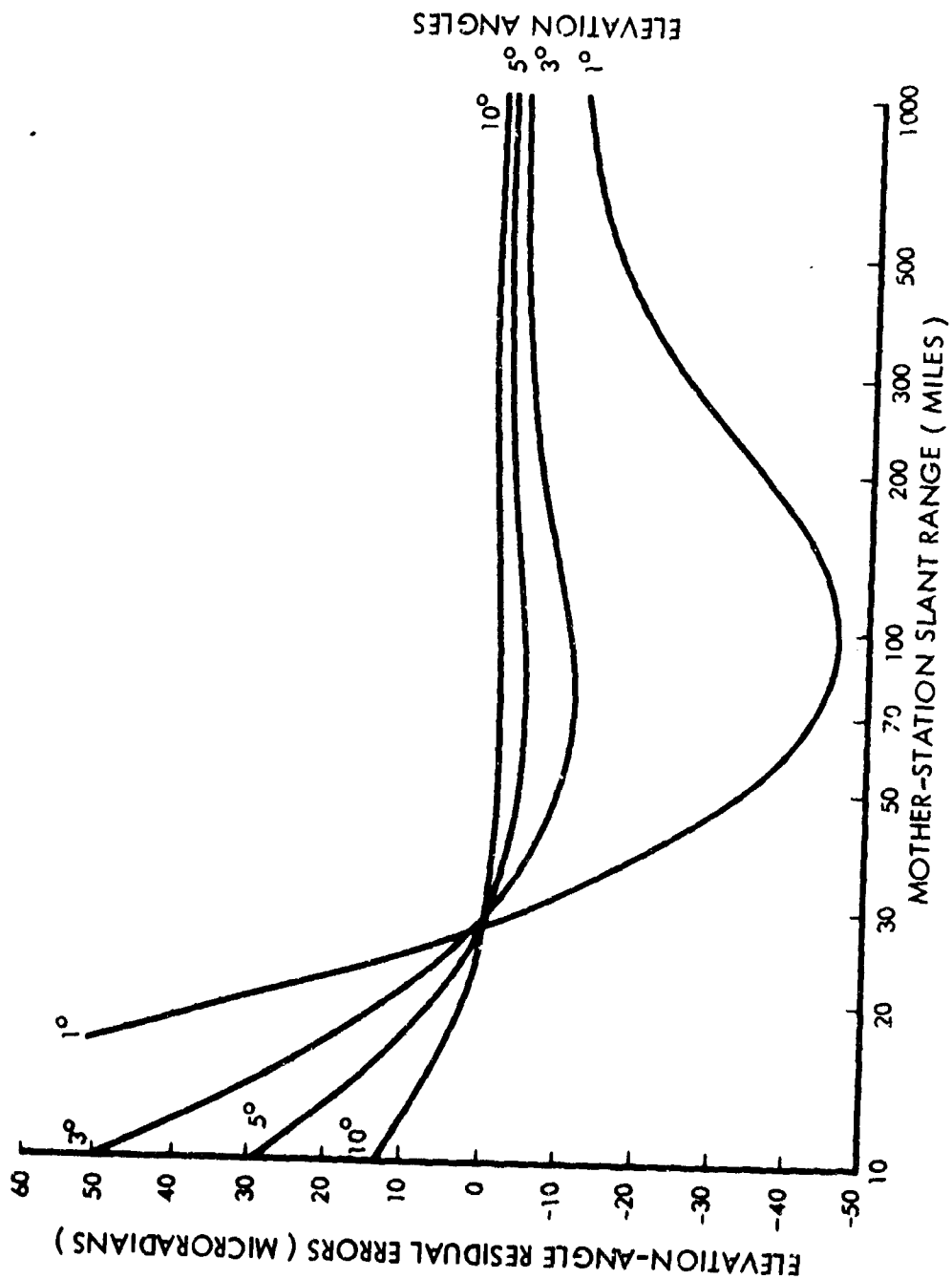


Figure 28 : RESIDUAL ELEVATION ANGLE ERRORS AS FUNCTIONS OF SLANT RANGE AND ELEVATION ANGLE WHEN $S_1 = S_2 = S$

Item 1 above establishes the fundamental measurement error, and its effect is felt regardless of the radiometric system configuration. The remaining items are classed as atmospheric effects. Of these latter items, Items 2, 3, and 4 affect spectrographic measurements performed with the hybrid active system; items 2, 3, 4 and 5 apply to the all-microwave active system; items 2, 3, and 5 apply to the passive system.

The reference-to-sensing signal ratio mode of operation greatly reduces the effect of Items 2 and 3 on measurement error. In descending order: line-broadening and mean-temperature specification effects result in the greatest percentage of error in the ultimate \bar{N} -specification; continuum extinction effects are next in importance; scintillation effects can be dismissed from consideration entirely. Under typical operating conditions, the total effect of all error contributors is that, with the hybrid system, \bar{N} -specification will be correct to from 0.5 to 1.0 percent, and with the all-microwave active or passive system the \bar{N} -error will amount to from 1.0 to 2.0 percent of \bar{N} . These \bar{N} -errors result in hybrid-system slant-range errors of about 1.0 feet rms for targets outside the atmosphere viewed at a 1 degree elevation angle. This error will be increased by about a factor 2.5 with the all-microwave or passive system. The associated residual elevation-angle errors will be on the order of tens of microradians.

Residual-error magnitudes decrease with decreasing slant range for targets imbedded in the atmosphere. In this case, however, the passive system accuracies will be degraded by an additional 10 percent over that realized by the all-microwave system, due to limited passive-system profiling capabilities.

Section II

INSTRUMENTATION

1. BACKGROUND

The considerations relating to the radiometric measurement of line-integrated refractivity discussed in Section I served to establish basic design features for the various line-integral refractometer configurations. Specifically, measurements of received energy intensities in absorptions bands must be referenced to similar measurements performed in nearby atmospheric windows; this is done to minimize degradation of the acquired data by continuum extinction effects. Furthermore, the active-system measurements must be performed simultaneously and through a single aperture to eliminate scintillation effects. With these general features in mind, the following instrument designs are offered as guides to ultimate instrument development.

2. INFRARED ACTIVE SYSTEM

A. Boeing system

(1) Description

An infrared system incorporating the basic design features listed above has been developed and qualitatively field tested by The Boeing Company (Reference 63). Briefly, energy from a continuous spectrum source is collected at a receiver through a single aperture. The field is collimated with a reflecting optical system. Temperature-compensated lead sulfide cells are used to sense the intensity of the collected energy in three bands of the infrared spectrum: one centered at a wavelength of 1.27 microns, the second at 1.73 microns, the third at 2.12 microns. The first wavelength lies in the oxygen band previously identified, the second is in the wing of the 1.86-micron water-vapor band, and the third is an atmospheric window. Wavelengths are isolated with narrow-band germanium interference filters. The required band-energy ratios are effectively determined by passing the appropriate detector outputs through logarithmic signal converters and then through a differential amplifier to a recorder. A more detailed description of the system is given in Appendix I.

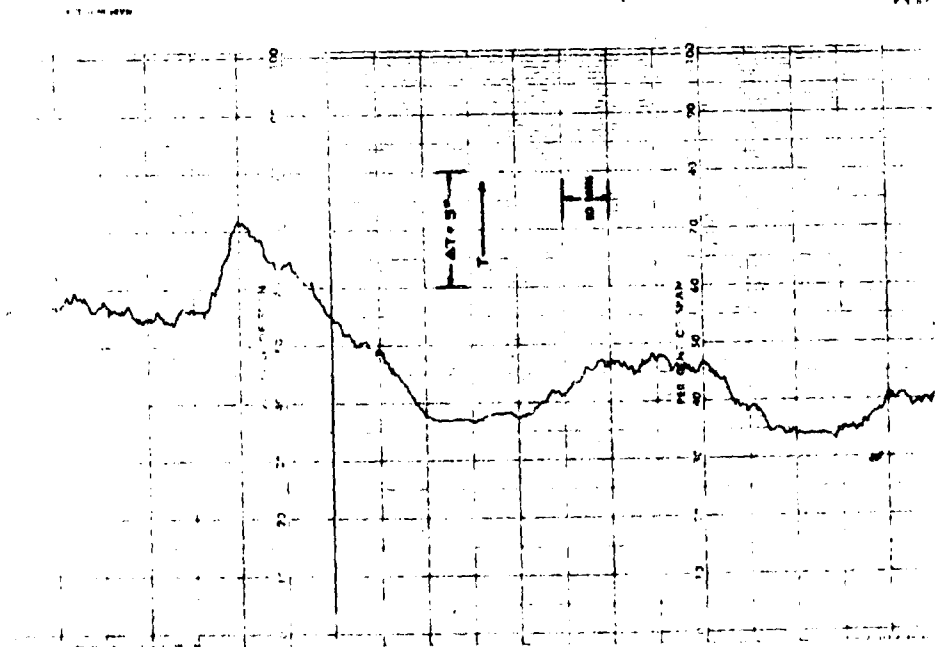
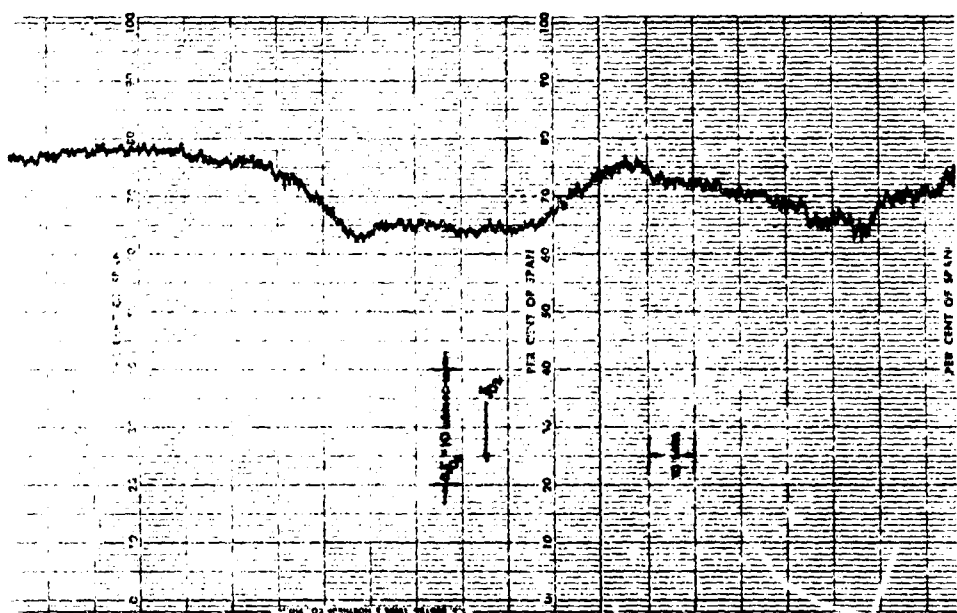
(2) Performance

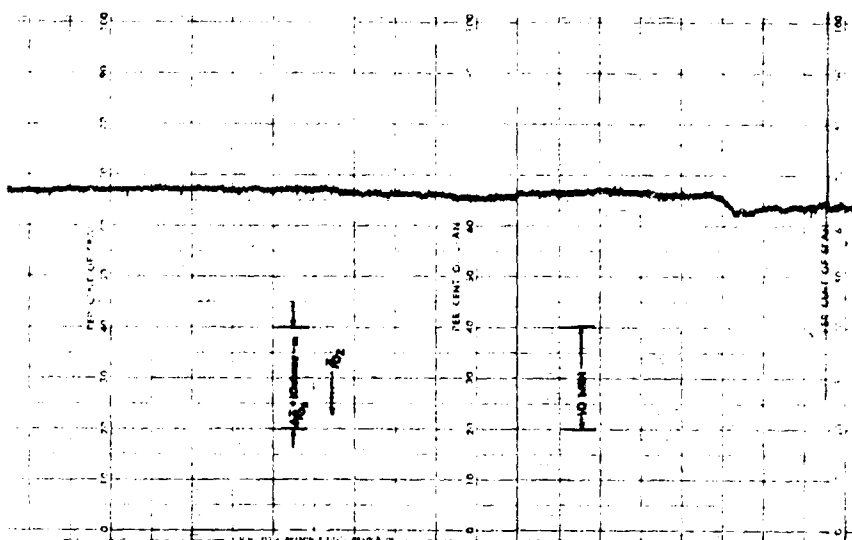
Examples of data collected with the Roeling infrared system are as shown in Figures 29, 30, and 31. Shown in Figure 29 are simultaneous recording of dry-bulb temperatures (the left-hand trace) and of line-integrated oxygen density (the right-hand trace) measured over a 2-kilometer propagation path. The scale factors are as indicated on the figure. Note that temperature increases to the right, and $\bar{\rho}_{O_2}$ increases to the left. The latter recorder response was selected because density is inversely proportional to temperature. Therefore, a given change in the temperature trace will be reflected in a corresponding change in the oxygen trace. The general trends of the two traces are well correlated, but the smoothed effect in the integrated value is also readily apparent. This effect demonstrates conclusively why estimates of line-integrated refractivity from point-measurement data are so uncertain.

Figure 30 again shows simultaneously recorded temperature and $\bar{\rho}_{O_2}$ traces, along with a wind direction and speed record. The notable feature is the correlation of the "humps" in the bottom portions of all four traces. The change in wind direction and speed obviously heralded warm-air advection (as evidenced in the temperature trace) — a circumstance that is also reflected in the $\bar{\rho}_{O_2}$ trace. Again, the integrated effect is not as great as the single-point effect.

Figure 31 shows simultaneous dry-bulb and integrated water-vapor density traces. As expected, very little correlation is noted between these two. The traces were obtained in early morning after a foggy night. Therefore, the slight warming trend indicated at the bottom of the temperature trace was reflected in the integrated vapor density, or absolute humidity, trace. The effect is attributable to the increased capacity of the air to hold more water vapor at the increased temperature.

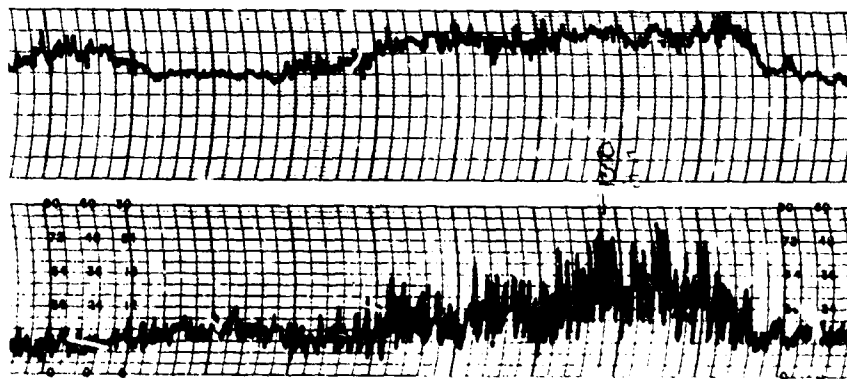
The purpose of the tests conducted during which the data shown in Figures 29, 30, and 31 were acquired was not one of instrument calibration, but rather to establish the basic worth of the instrument philosophy and design. For this purpose the tests were successful. That is, it was conclusively





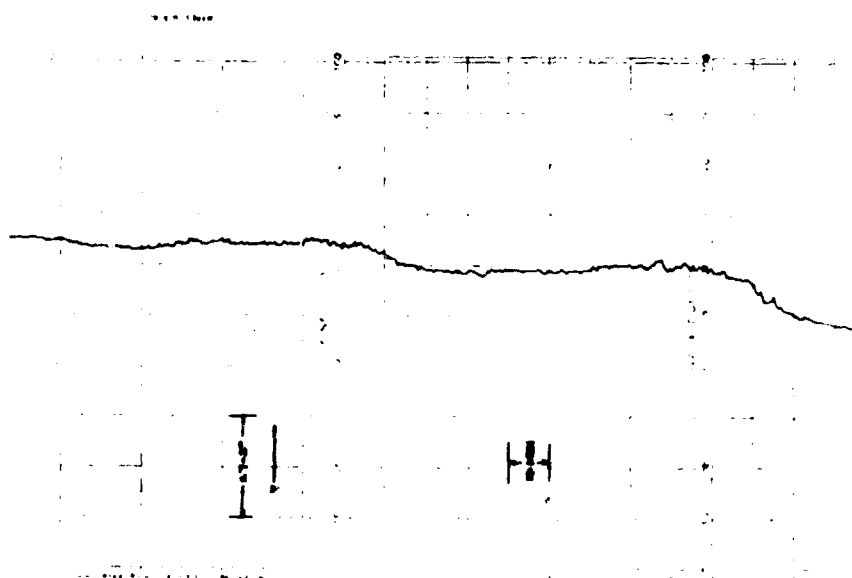
LINE-INTEGRATED OXYGEN DENSITY

Barham & Mitty Inc. WIND SPEED/WIND DIRECTION CHART MODEL 31771

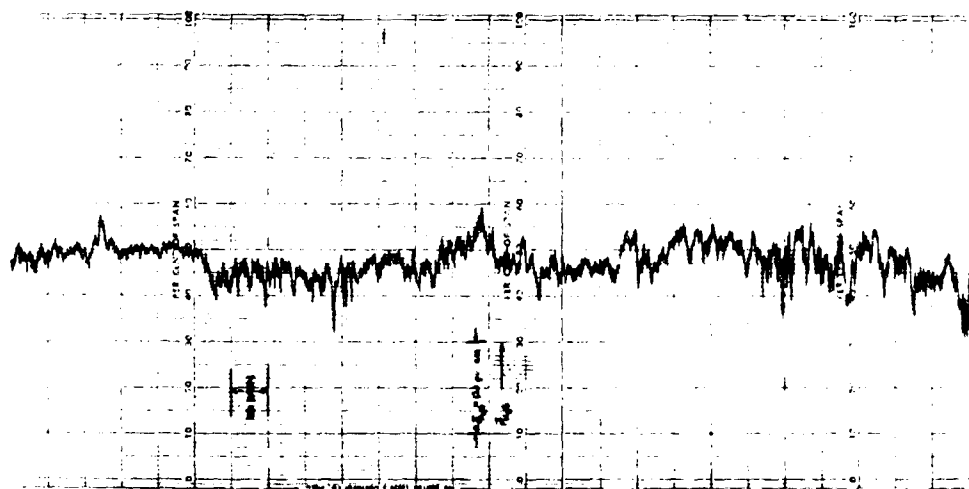


WIND DIRECTION

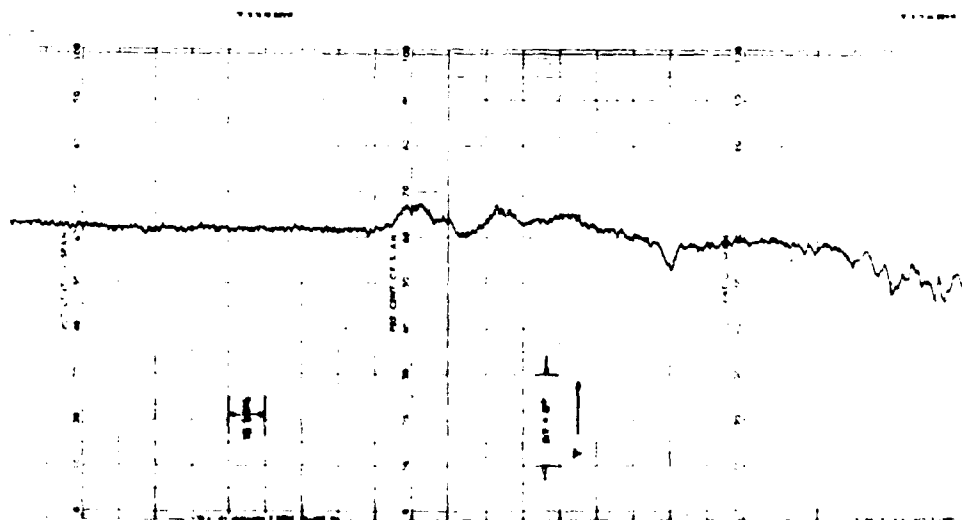
WIND SPEED



DRY BULB TEMPERATURE



LINE-INTEGRATED WATER VAPOR DENSITY



DRY BULB TEMPERATURE

demonstrated that (1) integrated oxygen and water-vapor density data are readily attainable by spectrographic means, and (2) that the sensing-to-reference band ratio mode of operation serves effectively to negate the potentially adverse effects of continuum extinction and scintillation on data quality.

B. Range operations system

The Boeing infrared system just described defines the basic design for the development of the system applicable to range operations. For such operations, however, it is tentatively suggested that the sampling wavelengths be 1.264 microns for the oxygen band, 1.32 microns for the water-vapor band, and 1.22 microns for the window. Such relocation of the water-vapor sensing wavelength will likely ensure transmittances high enough for measurable signals even at the extreme ranges likely to be encountered in ranging operations. The relocation of the window wavelength is for closer grouping of the three wavelengths for the maximum compensation for continuum extinction effects (see Equation 158). The system can be further upgraded by (1) increasing the size of the collecting optics, and (2) using cooled radiation detectors. The former procedure results in the direction of a greater amount of energy onto the detector, the latter in increased detector detectivities (Reference 64).

C. Expected performance

The power received by a detector from a remote source emitting energy in the wavelength interval $\Delta\lambda$ can be estimated from

$$P = I_{\lambda_e} A_T \cdot \frac{A_{opt}}{S^2} \cdot \tilde{\tau}_{at} \cdot \tilde{\tau}_{opt} \cdot \Delta\lambda \quad (205)$$

where P is the received power, I_{λ_e} the radiant intensity of the source, A_T the area of the target, A_{opt} the aperture area of the collecting optics, $\tilde{\tau}_{at}$ the transmittance of the atmosphere, $\tilde{\tau}_{opt}$ the transmittance of the collecting optical system, $\Delta\lambda$ the wavelength interval of the band pass filter, and S the slant range

Consider the following parameter values:

$$I_{\lambda_e} \approx 5 \times 10^2 \text{ watts cm}^{-2} \text{ sterad.}^{-1} \text{ micron}$$

$$A_T \approx 4 \times 10^1 \text{ cm}^2$$

$$P_{\text{rec}} = 10^{-3} \text{ cm}^2$$

$$P_{\text{rec}} = 10^{-3}$$

$$P_{\text{rec}} = 10^{-1}$$

$$L_{\text{eff}} = 5 \times 10^{-2} \text{ microns}$$

$$S^2 \simeq 1.4 \times 10^{15} \text{ cm}^2$$

The above set of parameters relate to a 3-inch-diameter 3000°C target viewed with a 24-inch-diameter telescope at an elevation angle of 1 degree and at a slant range of about 380 kilometers (the distance to the top of the atmosphere). Under these conditions the power received is on the order of 10^{-12} watts. The detection of such low signal levels is within the capability of current cooled-detector technology. Thus, on an average "clear" day, the infrared system could continue to function until tracked targets left the atmosphere. Thereafter, operation would switch to the all-microwave system. On excessively hazy days, the switch to all-microwave operation might have to be effected sooner.

3. MICROWAVE ACTIVE SYSTEMS

The philosophy of the microwave active systems is the same as the active infrared system; that is, received powers in oxygen and water-vapor bands must be referenced to power levels received in atmospheric windows. The requirement is for dual-frequency beacons and dual-frequency receivers. For the water-vapor measurements, it is therefore suggested that 3.5 GHz be used as the reference frequency and 17 GHz as the sensing frequency. This sensing frequency, lying in the wing of the 22-GHz water-vapor band, is harmonically related to the reference frequency; thus, frequency multiplying techniques can be used in both

beacon and receiver to simplify instrument design. Similarly, for the oxygen measurements, 11-GHz can be used as the reference frequency, and 44-GHz (in the wing of the 60-GHz oxygen band) can be used as the sensing frequency. Here, too, the reference and sensing frequencies are harmonically related, again leading to simplification in instrument design.

Both the beacon and receiver designs in both the 44-GHz and the 17-GHz systems have similar design concepts. The beacons will differ only in the rf transmitter power requirements, and the receivers will differ only in mixers and local oscillators. Therefore, beacon and receiver designs can be presented as applicable to both systems.

A. Dual-frequency beacons

The basic beacon design is shown in Figure 32. In general, both dual-frequency beacons will be pulse-modulated units featuring solid-state signal generation. In the 8.5/17-GHz system, signals can be amplified with traveling-wave tube amplifiers (TWT); in the 11/44-GHz system, signals can be amplified with pulsed high-power magnetrons. Carrier frequencies can be derived by using a veractor multiplying chain to up-convert a low-frequency crystal-controlled oscillator output. Highly stable local oscillators will serve both frequencies in each system. In the water-vapor system, a frequency doubler will serve to boost the 8.5-GHz reference frequency to the 17-GHz sensing frequency.

The modulators will be transistorized and will contain oscillators, squaring circuits, switch drivers, and switches. The switches will be capable of switching 1-watt power levels with an insertion loss less than 1 db, on/off isolation of 40 db, and switching rise times of 10 nanoseconds. Presently available diode switches reliably satisfy these requirements. The remaining modulator functions are not significant design impositions, and standard-type circuits will be used.

The bandpass filters can be of the waveguide, using Tchebysheff techniques to achieve minimum ripple and insertion loss while retaining the desired cutoff characteristics. Loads must be equalized at the filter output and input to ensure minimum mismatch losses.

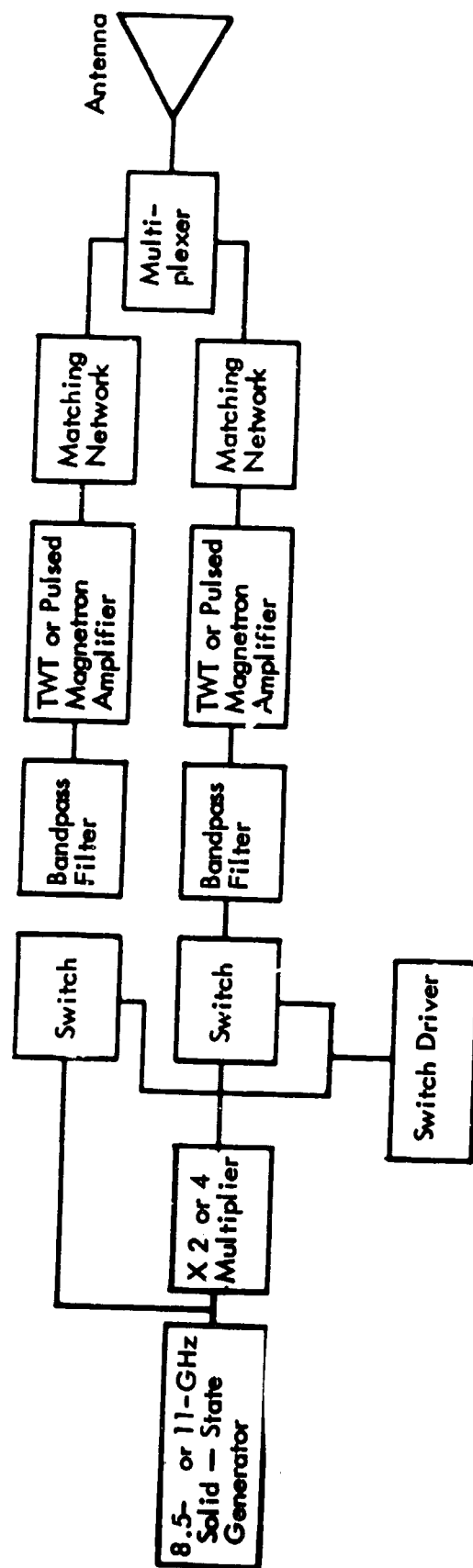


Figure 32: BLOCK DIAGRAM OF THE 17-GHz OR 44-GHz ACTIVE-SYSTEM BEACON

B. Dual-frequency receivers

The receiver shown in Figure 33 is a two-channel, superheterodyne, PRF-gated subsystem, PRF gating can be achieved by switching off the LO signal for the PRF period after receiving a pulse. At the end of the period, the "LO" signal comes back on and the receiver is again on for the next pulse. A delay of 100 nanoseconds should be incorporated to allow the full pulse to be processed. Boxcar detectors can be used to retain the data during the interpulse periods. Provision should also be made for observing with a sampling scope the data at the output of the IF amplifier to determine the influence of multiple transmission paths or noise.

Bandwidths of the receivers should be wider than those of the transmitters so that differences in the pulse slopes between short and long transmission may be observed. PRF gating can be used to remove multipaths via antenna side lobes and also to reject environmental noise between pulses.

C. Expected performance

The frequencies specified for both active microwave systems were chosen to ensure large enough atmospheric transmittance values for workable received power levels at low elevation angles and extreme slant ranges. It is expected that, even for targets beyond the atmosphere at 1 degree elevation angle, the oxygen absorption at 44-GHz will result in signal losses of order 10db. Thus, in spite of inverse-square-law radiation-spreading losses, targets may be tracked to much greater slant ranges with the microwave systems than with the infrared systems, because microwaves do not suffer from attenuation by atmospheric haze.

Because the wavelength region in which the active systems operate is not represented by suitable cw power sources, the systems are designed for pulsed operation. Consequently, the designs specified in Figures 32 and 33 largely incorporate components well within the capability of current microwave technology. With gain stabilization thereby achieved (on the order of 10^{-2} db), and with horizontal polarization to minimize forward scattering effects, transmission measurements correct to 1 percent rms should be achieved. The contribution to \bar{N} error due to instrument noise is therefore not significantly greater than that established by atmospheric effects (Table 8).

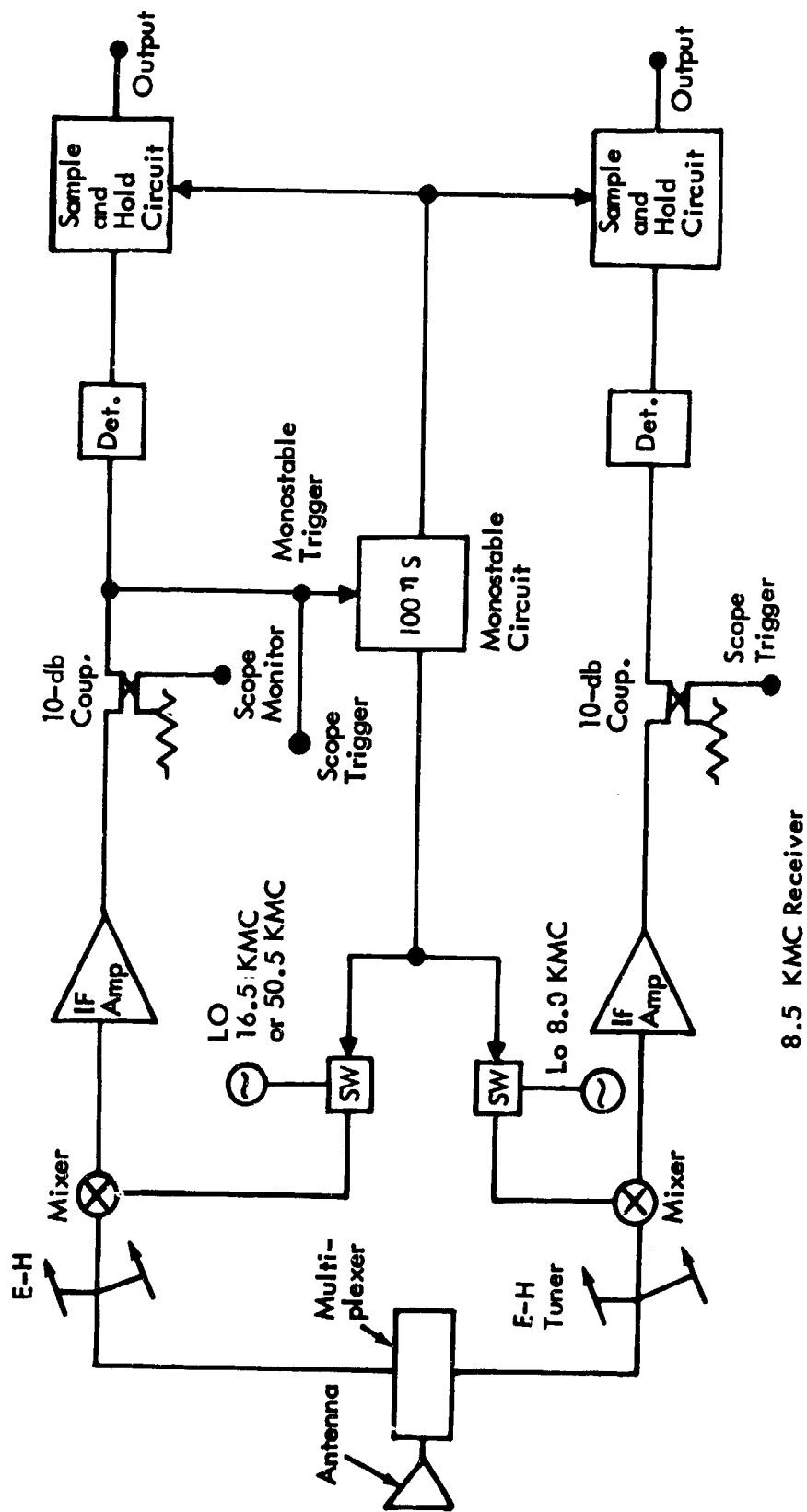


Figure 33: BLOCK DIAGRAM OF THE 17-GHz OR 44-GHz ACTIVE - SYSTEM RECEIVER

4. PASSIVE SYSTEMS

The radiometric receiver designs at 20 and 53 GHz are basically Dicke systems (Reference 65) using superheterodyne techniques. At 20 GHz, a three-channel receiver system with a window reference frequency is specified, while at 53 GHz a four-channel receiver with reference is required. For both the 20- and 53-GHz systems, each channel will be capable of measuring brightness temperature to 1°K.

A. Oxygen system

The design of the 53-GHz radiometer is shown in Figure 34. This system is designed with tunnel-diode amplifiers as the IF amplifiers so that two or more bands can be handled simultaneously. Duplication of some electronic components can be avoided with this technique.

For this 53-GHz region, the noise comparison source is injected at the IF because ferrite switches at 53 GHz would only have isolation in the off-state of approximately 20 db. The diode switch will give isolation of 60 db or more and will not modulate the local oscillator. The system will require accurate, known conversion loss. Single-sideband reception in the superheterodyne receiver is necessary so that only the absorption frequency region about 53 GHz is selected. The IF is selected at X-band to support the two individual channels simultaneously because the 300-MHz requirement on the bandwidth is somewhat restrictive and four frequency bands cannot be supported in one tunnel-diode amplifier. Although a traveling-wave tube (TWT) could theoretically support the four bands, the noise figure would be higher and the gain stability worse. Previous studies have shown that tunnel-diode amplifiers show excellent short-term (time \simeq 1 second) gain stability.

The traveling-wave tube is specified as the output stage because tunnel diode amplifiers saturate at a level given in dbm as 1 db compression point = $-(2G+10)$ dbm, where G = gain in db. If three-bands are amplified in the system simultaneously, the compression point will be lowered 10 db minimum. Consequently, the system will be designed to enter the TWT at or near a -60dbm signal level. By properly selecting waveguide size, single-sideband operation can be achieved by

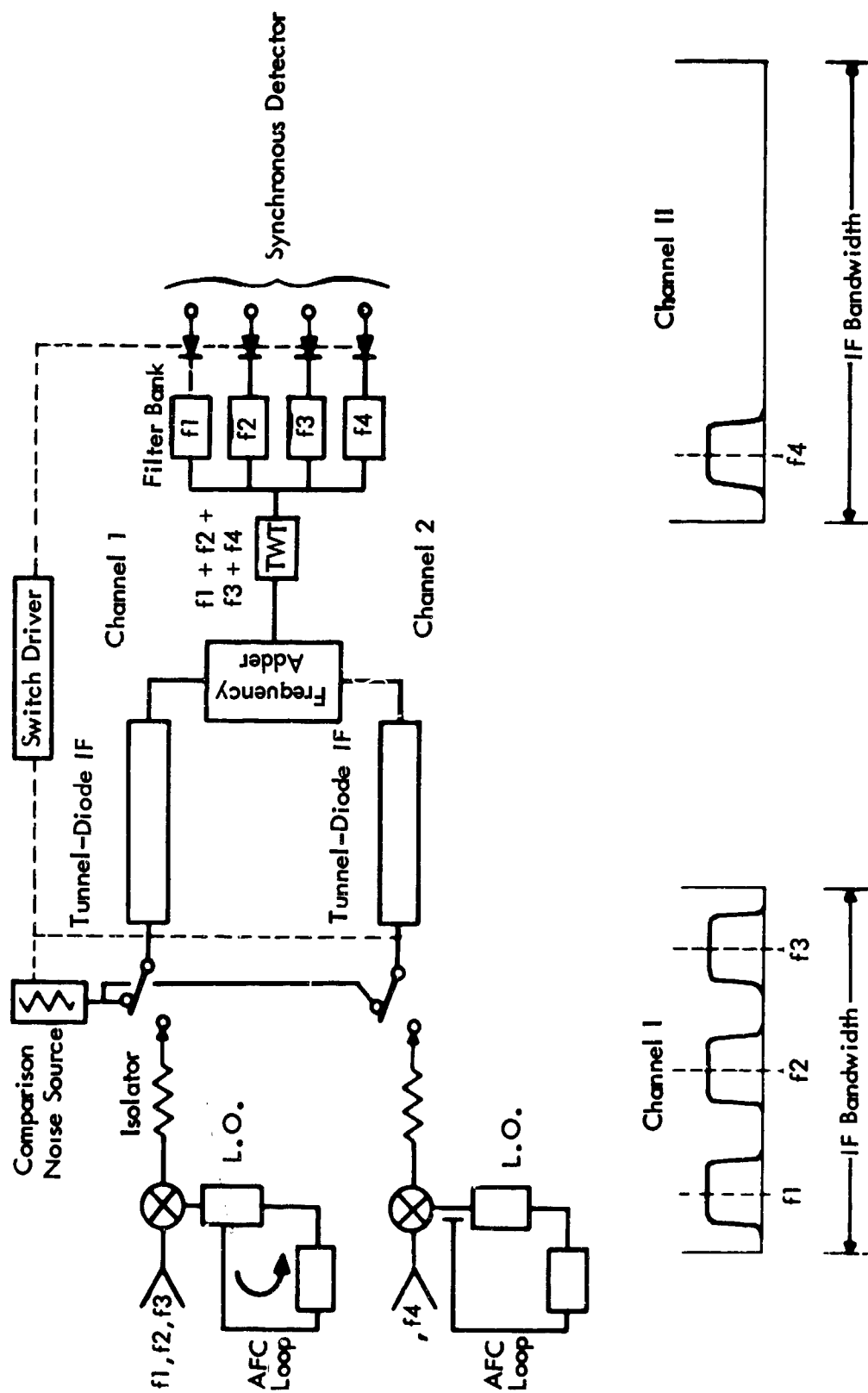


Figure 34: BLOCK DIAGRAM OF THE 53-GHz PROFILING RADIOMETER

operation of the lower sideband in a waveguide beyond cutoff. This form of filtering will modulate the impedance of the local oscillator, since filtering is accomplished before the signal enters the mixer and does not affect the desired signal. The insertion loss resulting from an increased waveguide length for the signal will be much less than that experienced in a lumped filter network. Figure 35 shows the general outline of this technique. Tentatively, operating-frequency bands have been specified as 52.3, 52.8, 53.3, and 54.8 GHz, with a bandwidth of 300 MHz per band. The three first channels are handled in a three-channel radiometer. The 54.8-GHz band must be handled in a separate channel because of the bandwidth limitations of tunnel-diode amplifiers. However, the second channel has the capability to study two additional bands and make a six-band radiometer if subsequent need arises. The bandwidth of the system can handle three bands and provide amplification with intermodulation products of ≤ 50 db.

The system is specified to have an accuracy $\Delta T_B = 1^\circ\text{K}$, and from Strom (Reference 66)

$$\Delta T_B = \left(\frac{32t}{W} T_s \right)^{1/2} \quad (206)$$

where

T_s = System noise temperature

W = Prediction bandwidth — 300 MHz

t = Look time

The system noise temperature will be approximately 5000°K. Using the above data, $t = 0.375$ second.

Field results usually show at least a 2:1 field degradation in ΔT_B measurements. Consequently, the look time will be 1 second or longer. The postdetection amplifier must be capable of handling low frequencies with good fidelity and low distortion. Because this is such an important technical area, an experimental study was undertaken to investigate design features. Figure 36 shows the schematic of a prototype postdetection amplifier; test results are shown in Figure 37. Representative sizes for this prototype postdetection amplifier are 1.5 by 0.5 by 3.5 inches.

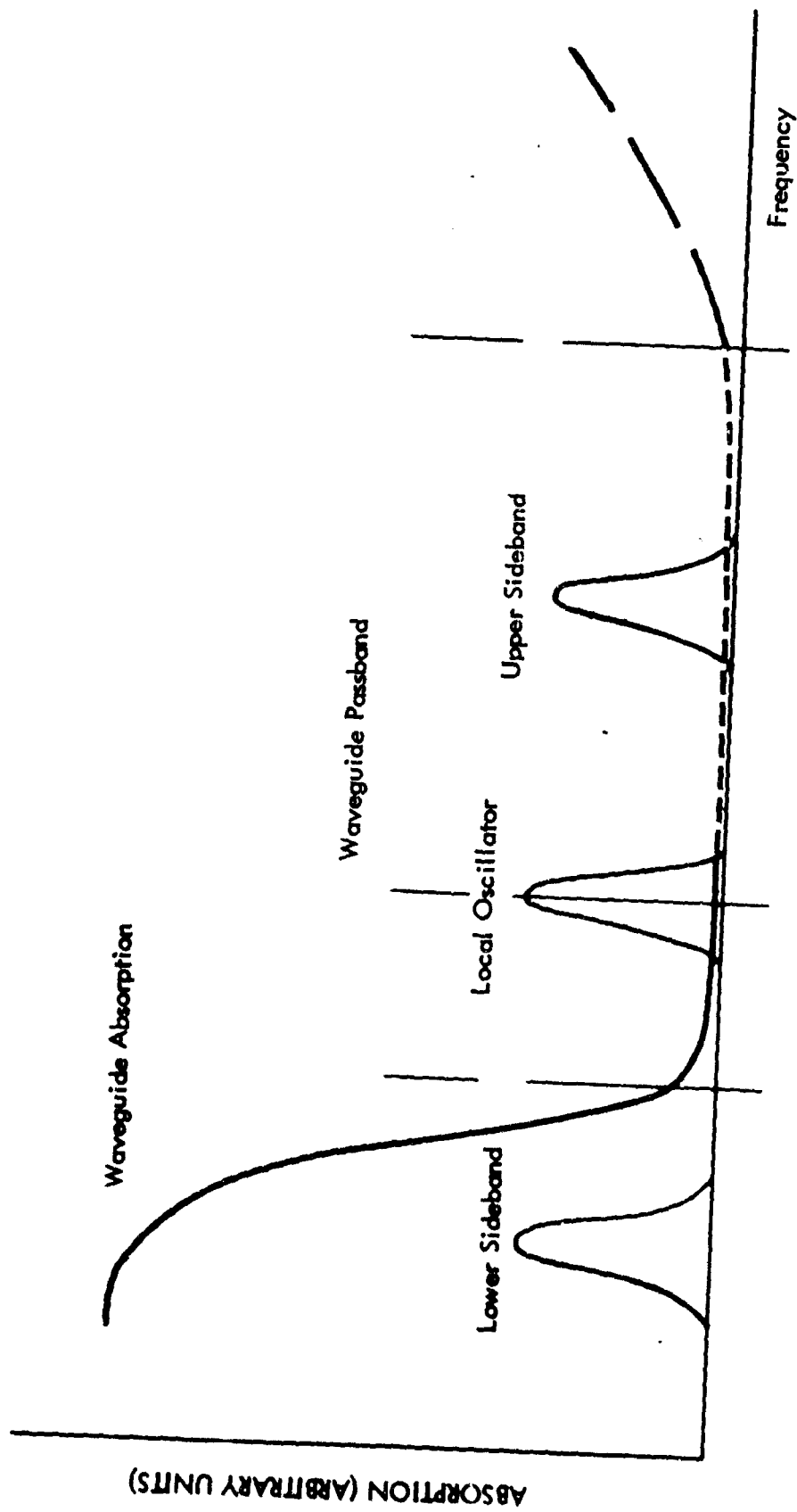


Figure 35: 53-GHz SINGLE-SIDE BAND OPERATION TECHNIQUE

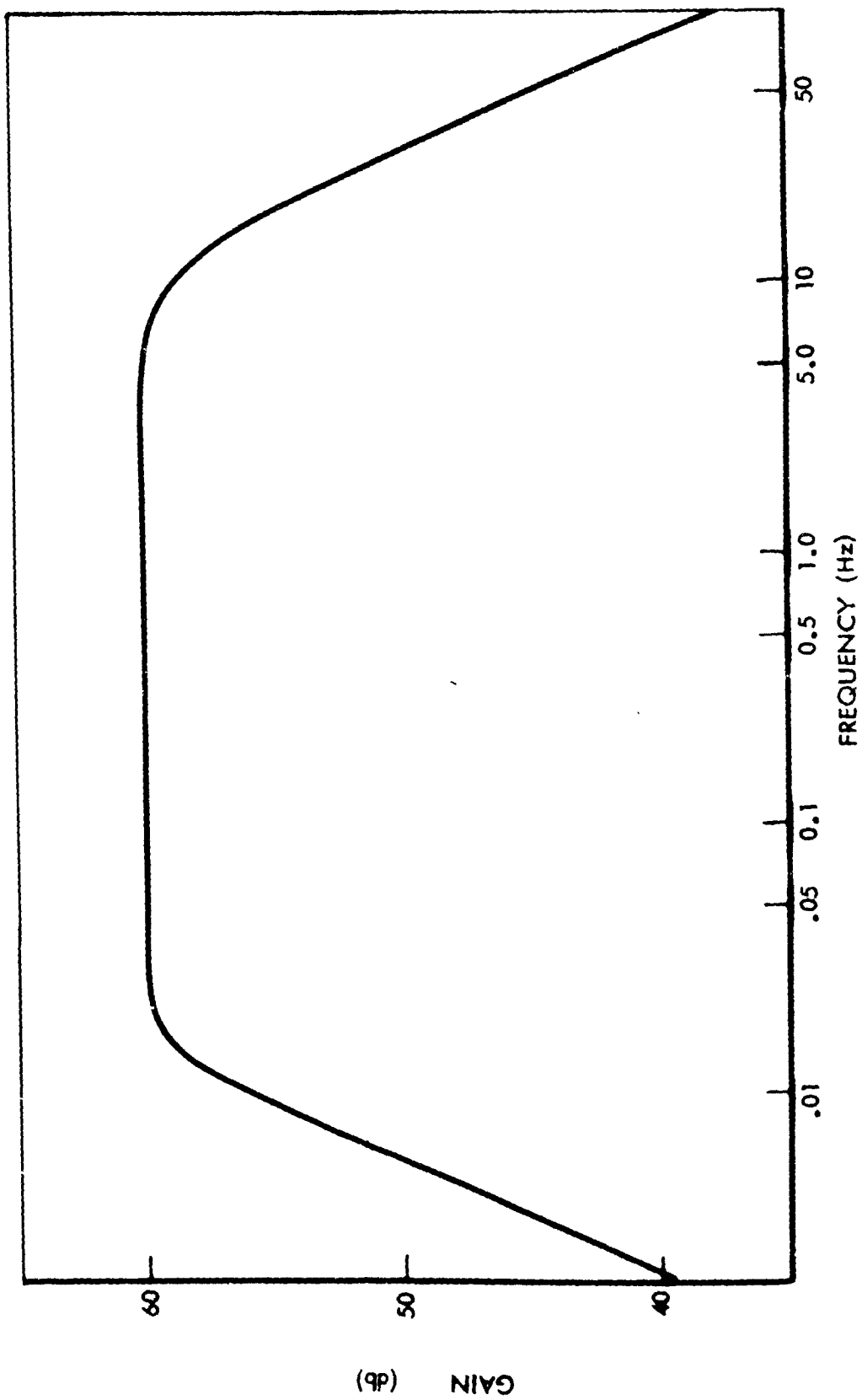


Figure 37: POSTDETECTOR AMPLIFIER-GAIN BANDWIDTH RESPONSE FOR MAXIMUM INTEGRATION TIMES

B. Water-vapor system

The 18-GHz water-vapor system is shown in Figure 38. It differs from the 53-GHz oxygen system in that each band has a separate receiver. The 20-GHz system uses transistor amplifiers in the IF to supply the 10-MHz bandwidth with the operating frequency of about 500 MHz. Sideband or image rejection is obtained by using a low pass filter, with the cutoff at the local oscillator frequency, mounted on the antenna side of the local oscillator.

The local oscillator is tentatively specified to be a solid-state unit with three frequencies tentatively specified as 19, 20, and 21 GHz, developed. The switching elements are specified as semiconductor switching diodes to reduce leakage because ferrite switches do not provide high isolation at the higher frequencies.

For the individual bands in Figure 38, the bandwidth will be 100 MHz, $T_S = 2600^\circ\text{K}$, $T_B = 1^\circ\text{K}$, and the look time is $t = 0.5$ seconds, which again will be boosted to 1 second or more to achieve the $\Delta T_B = 1^\circ\text{K}$.

C. Additional comments

Both the 20- and 53-GHz systems are cut off at the detector, unless experience gained with operating systems indicates the advisability of continuous readings in all bands. It may be sufficient only to scan the bands, but this cannot be ascertained until the systems are field tested. Insofar as possible, both systems will be designed around solid-state components to increase reliability and reduce power requirements.

The window radiometer is identical for both systems. It must be a separate instrument. The instrumentation for this receiver can be an AIL Type 2392-B universal radiometric system, which provides a cost-effective method of obtaining the window band with a minimum of design and test efforts. Although some of the system aspects outlined above may seem overly complex, such complexity is necessary to achieve desired results.

D. Expected performance

The four-channel oxygen system will permit four-layer integrated oxygen density profiling, whereas the three-channel water-vapor system will permit only

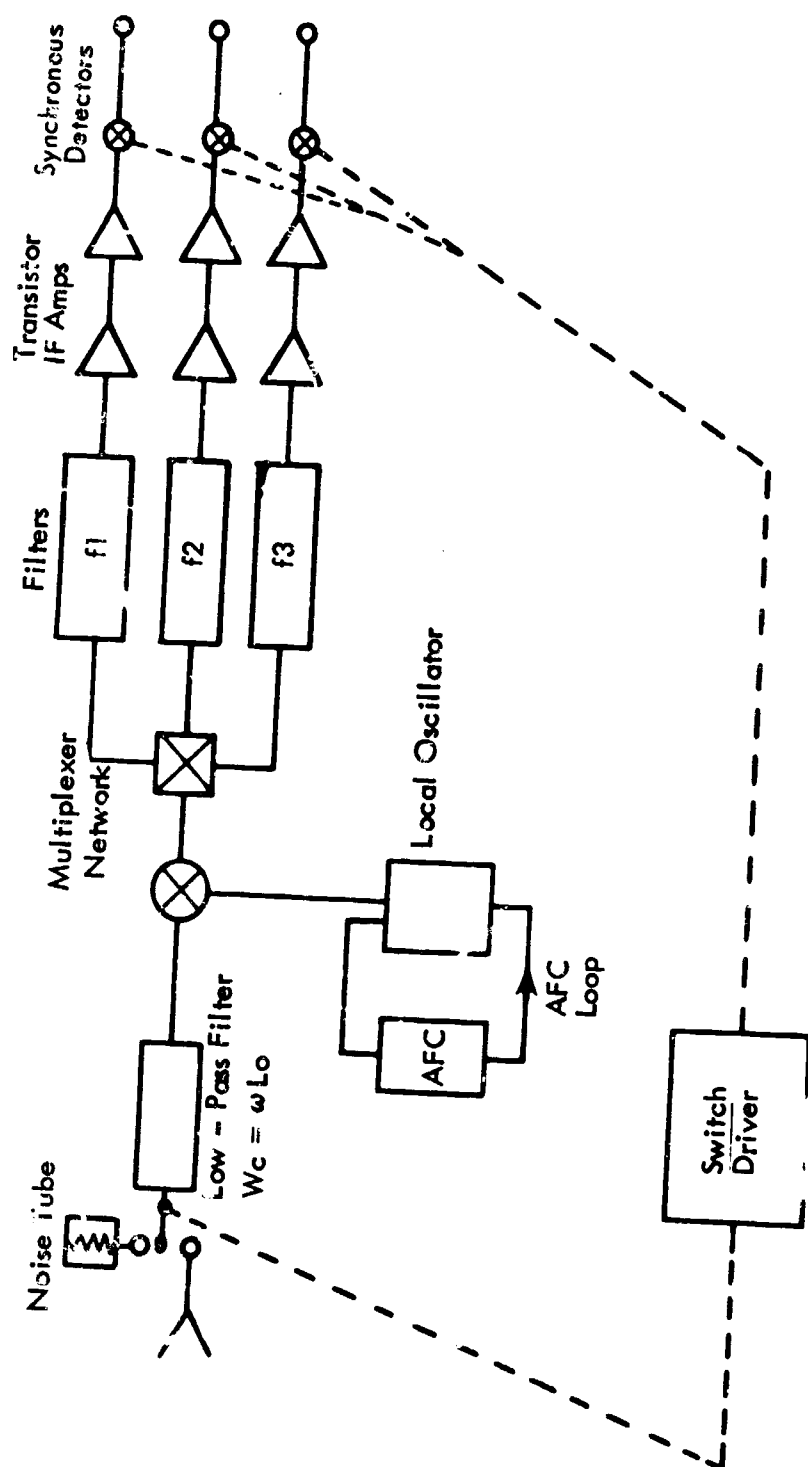


Figure 38: BLOCK DIAGRAM OF THE 20-GHz PROFILING RADIOMETER

a three-layer integrated water-vapor density profile. However, the vertical extent of the effective water-vapor atmosphere is much less than that of oxygen; therefore, three layers are considered sufficient.

An integration time of 1 second is required to effect the measurement of brightness temperature for each layer; thus, some of the real-time capability is lost. However, the values of $\overline{\rho_{o_2}}$ and $\overline{\rho_w}$ to be inferred from such measurements are applicable to layers of finite vertical extents, and must be interpreted as average values for these layers. The finite times taken by targets in moving through such layers lessens the impact of the lost real-time capability.

Both systems will provide brightness temperatures correct to $\pm 1^\circ\text{K}$, and accuracies in integrated absorption to better than 1 percent. The further contribution to \bar{N} error from instrument noise is again of minor importance.

5. SUMMARY

The three different types of radiometric systems required to satisfy all requirements for line-integrated measurement in all ranging operations are within the current capability of both infrared and microwave technology. Also, systems can be designed and constructed to perform the \bar{N} measurements in real time to the precision allowed by the limiting effects of atmospheric noise. Furthermore, insofar as the measurements are performed in real time, no data processing is required, and the information obtained can be introduced directly into the tracking radar systems readouts so that the corrected range parameter values are the direct outputs of the radar systems.

The designs of all the systems just presented — hybrid active, all-microwave active, and passive — must be accepted as tentative engineering model designs rather than as true prototype-system designs. No design can be called final because there is too much empiricism in the "laws" invoked to describe the transmission of energy through the atmosphere. Such final design can come only from experimentation with the engineering-model instrumentation.

Section III

CONCLUSIONS AND RECOMMENDATIONS

1. CONCLUSIONS

A. Range-data correction

The interferometric or trilateration mode of ranging operations isolates target slant range as the basic range parameter. Thus, ray retardation is the atmospheric effect that causes errors in ranging data. Accurate evaluation, from real-time measurement of line-integrated refractivity, \bar{N} , is therefore mandatory for precision ranging operations.

Estimates of \bar{N} from point measurements of refractivity do not satisfy the real-time precision requirements of ranging operations. The problem is the inadequacy of the representation of an integrated function as a finite sum. The direct measures of the integrated function from ray transit time differences at two radiation wavelengths — established by (1) normal dispersion at optical wavelengths, and (2) anomalous dispersion across atmospheric constituent absorption bands at radio wavelengths — also do not provide the complete answer. The normal-dispersion technique is inadequate because the data so obtained can be applied only to optical ranging devices. The anomalous-dispersion technique cannot provide a true real-time capability in \bar{N} measurement because of excessive data-processing averaging times. Also, both dispersion techniques require cooperative targets in their implementation.

B. Solution

Both absorption and refraction of radiation proceed in proportion to atmospheric composition, thereby providing the basis for an alternate approach to the measurement of \bar{N} . That is, at optical frequencies (corresponding to wavelengths less than 20 microns) the form of the atmospheric input parameter to absorption calculations is precisely that of the electronic charge distortion terms (as identified by the first two of the three-term Smith-Weintraub refractivity equation) of line-integrated refractivity; at microwave frequencies the form of the absorption parameter matches that of the \bar{N} water-vapor dipole orientation term.

Radiation-absorption measurements performed in oxygen and water-vapor absorption bands at infrared frequencies, and in a water-vapor band at microwave frequencies, will thus provide the data required for calculating line-integrated refractivity as dictated by the integrated form of the Smith-Weintraub refractivity equation.

Three, distinct, spectrographic line-integral refractometers are proposed to satisfy the demands of all types of ranging operations. For missile test-range operations — which are characterized by (1) the availability of cooperative targets, and (2) conformance of test schedules to ideal weather conditions — the combined infrared/microwave active system is offered as one that provides the capability for the most accurate \bar{N} determinations. The 1.27-micron oxygen and the 1.37-micron water-vapor band may be used for the infrared measurements; the 22-GHz water-vapor band may be used for the microwave measurement.

To extend the capability of the active system to all-weather operations, an all-microwave system is envisioned. The 22-GHz water-vapor-band measurements can be used to evaluate both water-vapor terms of the \bar{N} equation. Absorption measurements in the 55-GHz oxygen band may be used in place of the 1.27-micron oxygen measurement.

A passive mode of operation is suggested for noncooperative targets. In this mode the absorption measurements are equivalently performed by measuring thermal emissions of the atmosphere in the 55-GHz oxygen and 22-GHz water-vapor bands. Also, multifrequency operation in each band will provide a capability for a degree of \bar{N} profiling.

C. Expected results

By referencing absorption-band-radiation intensity measurements to similar measurements performed in nearby atmospheric-window regions of the absorption spectrum, it is anticipated that line-integrated refractivity may be correctly estimated to within 0.5 to 1.0 percent when using the hybrid, combined infrared/microwave line-integral refractometer. With the all-microwave system, \bar{N} will be accurate to within 1.0 to 2.0 percent. An additional 0.5-percent error will arise when the passive microwave system is applied to tracking targets imbedded in the atmosphere. Such accuracies in \bar{N} measurement imply that,

with the hybrid system, residual errors in slant-range measurements to targets outside the atmosphere viewed at a 1-degree elevation angle will be about 1.0-foot rms. With the other systems proposed, the slant-range residual error will increase by the factor of increase in the basic \bar{N} uncertainty. The associated residual elevation-angle errors will be on the order of tens of microradians.

D. Instrumentation

The three different types of radiometric systems needed to satisfy requirements for line-integrated refractivity measurements in all ranging operations are within the current capability of both infrared and microwave technology. Moreover, systems can be designed to perform \bar{N} measurements in real time to the precision allowed by the limiting effects of atmospheric noise.

2. RECOMMENDATIONS

The designs for the three basic \bar{N} measurement systems — hybrid active, all-microwave active, and passive — presented in this study are not true prototype designs, but must be accepted as tentative engineering-model designs. There is too much empiricism in the "laws" invoked to describe the transmission of energy through the atmosphere for any design to be set forth as final.

It is recommended, therefore, that the instrument designs presented be implemented as engineering models, and that such models then be evaluated to determine the advisability of proceeding to the true prototype system. Such an evaluation will necessarily involve two aspects: calibration and performance.

A. Engineering-model calibration

Because of the uncertainty that exists in the various semiempirical absorption "laws" invoked to describe the atmospheric absorption process within different atmospheric constituent absorption bands and at various radiation wavelengths (Section I, Paragraph 6.C.(1)) it is impossible to perform a theoretical instrument calibration to any degree of precision. The calibration procedure must consist of comparing the instrument outputs against corresponding measurements of the quantities of oxygen and water vapor that exist in prescribed sensing paths. A calibration procedure using laboratory procedures is not feasible because of the excessive path lengths required to duplicate the typical quantities of

oxygen and water vapor that will exist in the atmospheric paths realized when tracking targets beyond the atmosphere at low elevation angles. At a 1-degree elevation angle, for example, such an atmospheric path would be equivalent to about a 200-kilometer sea-level path. Also, the actual form of the absorption law changes as the path length (optical depth) increases beyond a certain undefinable limit. The long-path calibration cannot, therefore, be expressed as a simple multiple of the short-path calibration.

(1) Active-system calibration

Active-system calibration will consist of comparing simultaneous measurements of absorption-band transmittances and partial densities of oxygen and water vapor. The problem, however, is that conventional meteorological instruments performed the measures of f_{O_2} and f_w at a single point, whereas the transmittance measurement represents a space-integrated (i. e., over the propagation path) effect. In a perfectly homogeneous atmosphere there would be no problem in estimating integrated partial-density values from point measurements because the former values would simply constitute the latter measurements multiplied by the propagation-path length.

Complete homogeneity in actual test situations cannot be expected. Careful test-site selection (e. g., an over-water propagation path with an over-water upwind fetch) can result in the closest possible approach to the ideal, but a one-to-one correlation between the integrated partial-density value and the single-point measurement simply cannot be expected. Therefore, the calibration curve must be determined statistically. That is, time-averaged values of partial-density data must be obtained at several points along a calibration propagation path. These time-averaged values then must be averaged again against each other to obtain what amounts to a time-and-space-averaged partial-density value. Multiplying this latter value by the propagation path length should yield something comparable to what the active-system transmissometer responds to on a time-average basis.

Figures 39a and b are examples of the calibration procedure just described. The solid curve in Figure 39a represents the plot of half-hourly values of line-integrated oxygen density (obtained with the Boeing infrared system)

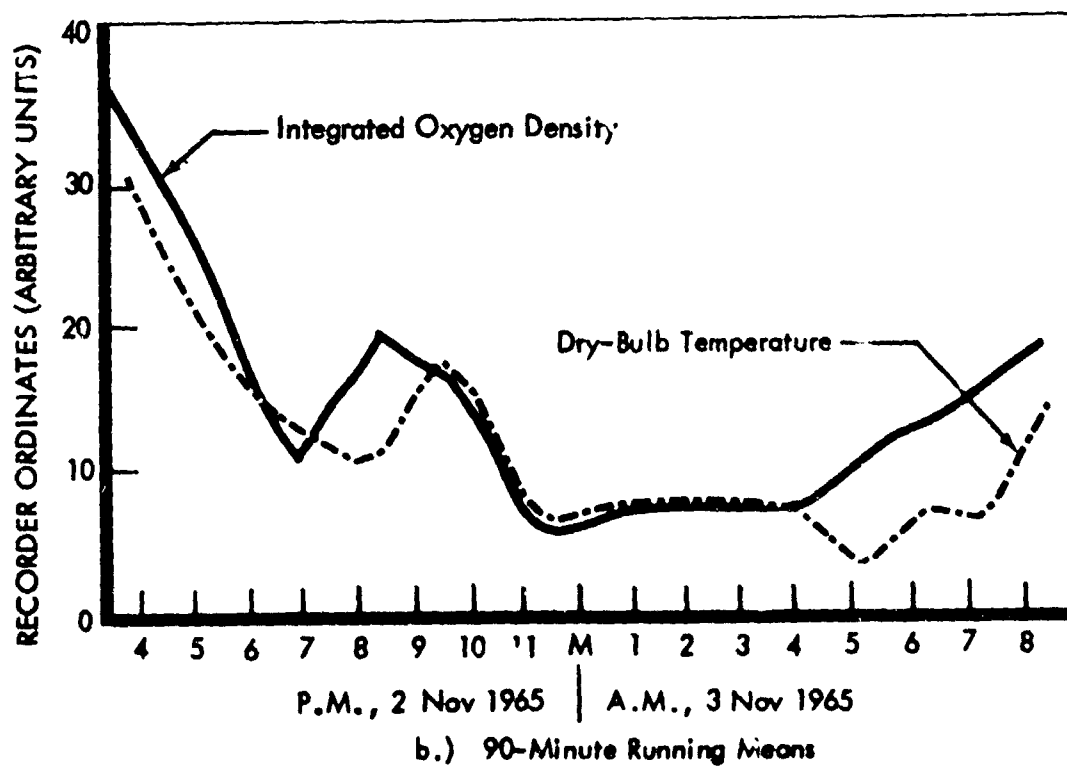
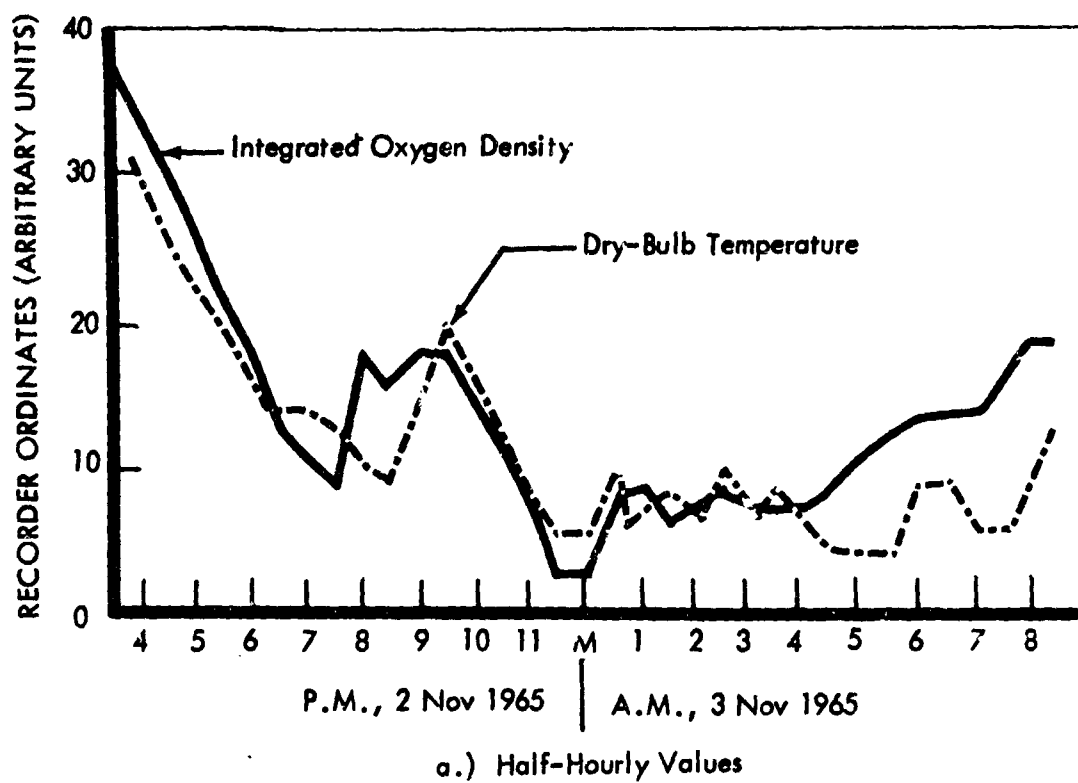


Figure 39: COMPARISON OF INTEGRATED OXYGEN DENSITY AND DRY-BULB TEMPERATURE DATA

measured over a 2-kilometer path the night of 2 November 1965. The dashed curve depicts the corresponding half-hourly values of dry-bulb temperature recorded at one end point of the propagation path. The abscissas are labeled in arbitrary units because the data are presented for comparative purposes only. A correlation between the $\overline{f_{o_2}}$ -data and the temperature data is readily apparent.

Figure 39b depicts 90-minute running means of the data contained in Figure 39a. Note that the simple time-averaging process has considerably "smoothed" both curves, and that from about 10:00 pm to 4:00 a.m. there appeared to be even a one-to-one correlation between the two sets of data. The conformance of the two sets of data would have been even more noticeable if additional temperature measurements had been performed at other points along the path. The spread in data points for a regression analysis would thus have been minimized, and the reliability of the ultimate calibration curve correspondingly increased.

The process just described should be completed for various path lengths under a variety of weather conditions to establish the calibration for the entire range of path lengths (and, hence, in transmittance) to be encountered in missile tracking operations. Note that for calibration purposes fast-response meteorological sensors are not required because averages in both time and space are to be performed anyway. Measurement accuracy is the desirable instrumentation feature. Partial densities are not to be measured directly, but are to be inferred (via the dictates of the equations of state) from precision measurements of dry-bulb and dewpoint temperatures plus atmospheric pressure. Boeing recommends that at least one set of calibration measurement be performed over a slant path from a valley to a mountain top in an attempt to determine the line-broadening pressure correction.

(2) Passive-system calibration

Calibration procedures for the passive systems would be similar to those for the active systems. That is, calibration would be based on a comparison of radiometric data with radiosonde temperature, pressure, and humidity data. Radiosonde data, however, represent approximately the amounts of water vapor and oxygen in a vertical column of the atmosphere. Hence, to establish

the passive system slant-path calibration, the radiosonde data would be multiplied by the appropriate air-mass factor. Again, the final calibration curve would be established on a statistical basis, with a regression analysis performed on a large mass of acquired radiosonde and radiometric data.

B. Engineering-model evaluation

(1) Active-system evaluation

The active-system calibration procedure outlined above will do nothing to establish the capability of the active-system line-integral refractometer for effecting the real-time, short-term, range-error corrections. Such an evaluation can best be performed through actual ranging measurements. That is, assume that a radar ranging system was set up over a fixed, measured course, such as between geodetic bench marks. The electrical range measured by the radar would show short-term fluctuation errors. Then, if the calibrated active systems were set up parallel to the radar path, the active-system data could be used to compute \bar{N} for the path and to correct the radar data continuously. If the measured electrical ranges were corrected to the known range continuously and to within the precision limits of the radar, then the refractometer evaluation would be established. If a residual bias error remained, an error in the refractometer calibration could be expected. A random residual error would indicate a "noise" error in the refractometer system. Simultaneous meteorological measurements would not be required in this evaluation scheme. Again, such tests should be performed over a range of propagation-path lengths.

(2) Passive-system evaluation

Because the passive system monitors only the self-emission of the sky, the electrical range measurements to be corrected would have to be measured to an airborne target. High-performance aircraft would suffice; that is, electrical range measurements would be made to the target, and these measurements would be corrected with the passive-system refractometer data. Again, if the correction yielded true slant-range data that was correct to within the precision limits of the radar, the capability of the refractometer would be established.

REFERENCES

1. Schulkin, M. , "Average Radio-Ray Refraction in the Lower Atmosphere, " Proc IRE, 40, pp. 554-561, May 1952.
2. von Handel, P. F. , and F. Hoehndorf, "High-Accuracy Electronic Tracking of Space Vehicles, " IRE Trans Mil Elec, MIL-3, pp. 162-172, Oct 1959.
3. Bean, B. R. , and G. D. Thayer, "Comparison of Observed Atmospheric Radio Refraction Effects with Values Predicted through Use of Surface Weather Observations, " J. Res. NBS, 67D(3), pp. 273-285, May-June 1963.
4. Gardiner, C. , "Tracking Errors at Low Elevation Angles Due to Tropospheric Refractive Effects, " Proceedings of the Second Tropospheric Refraction Effects Technical Review Meeting, Vol. II, TDR No. ESD-TDR-64-103, The Mitre Corp. , Bedford, Mass. , pp. 3.259-3.307, April 1964.
5. Mason, J. F. , "Modernizing the Missile Range; Part 2, " Mil. Elec. , pp. 108-118, March 8, 1965.
6. Chernov, L. A. , Wave Propagation in a Random Medium, McGraw-Hill Book Co. , Inc. , New York, 1960.
7. Martin, F. L. and F. E. Wright, "Radar-Ray Refraction Associated with Horizontal Variations in the Refractivity, " J. Geophys. Res. , 68(7), pp. 1861-1869, April 1963.
8. Debye, P. , Polar Molecules, Dover Publishing Co. , New York, 1957.
9. Campen, C. F. Jr. , R. M. Cunningham, and V. G. Plank, "Electromagnetic Wave Propagation in the Lower Atmosphere, " Handbook of Geophysics, (C. F. Campen, Jr. , A. E. Cole, T. P. Condron, W. S. Ripley, N. Sissenwine, and I. Solomon, Editors), The MacMillan Co. , New York, pp. 13.1-13.11, 1960.
10. Crain, C. M. , "The Dielectric Constant of Several Gases at a Wavelength of 3.2 Centimeters, " Phys. Rev. , 74, pp. 691-693, Sept 1948.
11. Birnbaum G. , "A Recording Microwave Refractometer, " Rev. Sci. Instrum. , 21(2), pp. 169-171, 1950.
12. Deam, A. P. , "An Expendable Atmospheric Radio Refractometer, " EERL Report 108, Univ. of Texas, Austin, Texas, May, 1959.
13. Hay, D. R. , H. C. Martin and H. E. Turner, "A Lightweight Refractometer, " Rev. Sci. Instrum. , 32, pp. 693-697, 1961.
14. Tolbert, C. W. and A. W. Stratton, Rev. Sci. Instrum. , 22, pp. 162-165, 1951.
15. Bean, B. R. , "The Radio Refractive Index of Air, " Proc IRE, 50(3), pp. 260-273, March 1962.

16. Smith, E. K. Jr. and S. Weintraub, "The Constants in the Equation for Atmospheric Refractive Index at Radio Frequencies, " J. Res. NBS, 50(1), pp. 39-41, Jan 1953.
17. Galbiati, L. J., "ESD Tropospheric Refraction Effects Task, " Proceedings of the Second Tropospheric Refraction Effects Technical Review Meeting, Vol. I, TDR No. ESD-TDR-64-103, The Mitre Corp., Bedford, Mass., pp. 1.3-1.13, March 1964.
18. Martin, C. F., "Accuracy of Tropospheric Refraction Correction Procedures, " Proceedings of the Second Tropospheric Refraction Effects Technical Review Meeting, Vol. II, TDR No. ESD-TDR-64-103, The Mitre Corp., Bedford, Mass., pp. 3.233-3.237, April 1964.
19. Bender, P. L., and J. C. Owens, "Correction of Optical Distance Measurements for the Fluctuating Atmospheric Refractive Index, " J. Geophys. Res., 70(10), pp. 2461-2462, May 15, 1965.
20. Taylor, D., "Electronic Instruments in Land Surveying, " Inst. Rev., pp. 510-512, Dec. 1965.
21. Sullivan, J. F., and H. M. Richardson, "Line-integral Refractometer, " 1964 World Conference on Radio Meteorology, Central Radio Propagation Laboratory, National Bureau of Standards, Boulder, Colo., pp. 324-329, Sept 1964.
22. Richardson, H. M., "Testing of the Line-integral Refractometer, " Proceedings of the Second Tropospheric Refraction Effects Technical Review Meeting, Vol. I, TDR No. ESD-TDR-64-103, The Mitre Corp., Bedford, Mass., pp. 1.91-1.106, March 1964.
23. Goody, R. M., Atmospheric Radiation I: Theoretical Basis, Oxford University Press, London, 1964.
24. Van Vleck, J. H., "Theory of Absorption by Uncondensed Gases, " Propagation of Short Radio Waves, Vol. 13, (D. E. Kerr, editor), pp. 646-664, Mc-Graw Hill Book Co., Inc., New York, 1951.
25. Menius, A. C., C. F. Martin, W. M. Layson, and R. S. Flagg, "Tropospheric Refraction Corrections Using a Microwave Radiometer, " Tech. Staff Memo No. 19, ETV-TM-64-12, Pan American World Airways, PAA Technical Staff, Patrick AFB, Florida, Nov. 16, 1964.
26. Drayson, S. R., "Atmospheric Transmission in the CO₂ Bands Between 12 μ and 18 μ , " App. Opt., 5(3), pp. 385-391, March 1966.
27. Westwater, E. R., "Ground-based Passive Probing Using the Microwave Spectrum of Oxygen, " Rad. Sci. J. Res., NBS/USNC-URSI, 69D(9), pp. 1201-1211, Sept 1965.

28. Van Vleck, J. H., The Absorption of Microwaves by Oxygen, " Phys. Rev., 71(1), pp. 413-424, April 1947.
29. Zimmerer, R. W. and M. Mizushima, "Precise Measurement of the Microwave Absorption Frequencies of the Oxygen Molecule and the Velocity of Light, " Phys. Rev., 121(1), pp. 152-155, Jan 1961.
30. Van de Hulst, H. C., Light Scattering by Small Particles, John Wiley and Sons, Inc., New York, 1957.
31. Fletcher, N. H., The Physics of Rainclouds, Cambridge University Press, Cambridge, 1962.
32. Tank, W. G., and D. R. Makela, "Reviews in Geophysics No. 2, Meteorological Support to Project Yellowstone, "Boeing Document D6-8870, The Boeing Co., Seattle, Washington, May 1962.
33. Zabrodskii, G. M., and V. G. Morachevskii. "Study of the Transparency of Clouds and Fogs, " Leningrad. Arkticheskii i Antarkticheskii Nauchno-Issledovatel'skii Institut, Trudy, 288(1), pp. 68-86, 1959.
34. Gates, D. M., and C. C. Shaw, "Infrared Transmission of Clouds," J. Opt. Soc. Amer., 50(9), pp. 876-882, Sept 1960
35. Gutnick, M., "Mean Annual Mid-Latitude Moisture Profiles to 31 Km," Air Force Surveys in Geophysics No. 147, Air Force Cambridge Research Laboratories, L. G. Hanscom Field, Mass., July 1962.
36. Fryberger, D., and E. F. Uretz, "Some Considerations Concerning the Measurement of the Atmospheric Temperature Field by Electromagnetic Means," IRE Trans. Mil. Electron, MIL-5(4), 279-285, 1961.
37. Phillips, D. L., "A Technique for the Numerical Solution of Certain Integral Equations of the First Kind," J. Assoc. Computing Machinery, 9, pp. 84-97, 1962.
38. Hildebrand, F. B., Methods of Applied Mathematics, Prentice-Hall, Inc., Englewood Cliffs, N. J., 1952.
39. Wark, D. Q., "On Indirect Temperature Soundings of the Stratosphere from Satellites," J. Geophys. Res., 66(1), pp. 77-82, Jan 1961.
40. Hilleary, D. T., and D. Q. Wark, "The Experimental Determination of the Atmospheric Temperature Profile by Indirect Means," Nature, 205(4970), pp. 489-490, Jan 1965.
41. Westwater, E. R., and R. L. Abbott, "Passive Probing in the Microwave Region and Microwave Absorption Properties of Oxygen," NBS Rpt 8799, U. S. Dept. Commerce, National Bureau of Standards, Wash., D. C., March 1965.

42. Miller, S. L., and C. H. Townes, "The Microwave Spectrum of O^{16}_2 and O^{16} and O^{17} ," Phys. Rev., 90(4), pp. 537-541, May 1953.
43. Tsao, C. J., and B. Curnutte, "Line Widths of Pressure Broadened Spectral Lines," Geophys. R. Paper 69, Geophysical Research Directorate, AF Cambridge Research Lab., Cambridge, Mass., Sept 1960.
44. Meeks, M. L., and A. E. Lilley, "The Microwave Spectrum of Oxygen in the Earth's Atmosphere," J. Geophys. Res., 68(6), pp. 1683-1703, March 15, 1963.
45. Davis, H. T., Introduction to Nonlinear Differential and Integral Equations, Dover Publications, Inc., New York, 1962.
46. Howard, J. N., J. I. F. King, and P. R. Gast, "Thermal Radiation," Handbook of Geophysics, (D. F. Campen, Jr., A. Cole, T. P. Condron, W. S. Ripley, N. Sissenwine, and I. S. Ormon, Editors), The MacMillan Co., New York, pp. 16.1-16.32, 1960.
47. Neporent, B. S., and M. S. Kiseleva, "Measurement of the Humidity of Gas Mixtures by Infrared Absorption Spectra," Optics and Spectroscopy, XVI (5), pp. 437-442, May 1964.
48. Elsasser, W. M., "Heat Transfer by Infrared Radiation in the Atmosphere," Harvard Meteorological Studies No. 6, Harvard University Press, Cambridge, Mass., 1942.
49. Gates, D. M., and W. J. Harrop, "Infrared Transmission of the Atmosphere to Solar Radiation," App. Optics, 2(9), pp. 887-898, Sept 1963.
50. Carpenter, R. O'B., J. A. Wight, A. Quesada, and R. E. Swing, "Predicting Infrared Molecular Attenuation for Long Slant Paths in the Upper Atmosphere," Scientific Report No. 1, Contract No. AF19(604)-2405, Baird-Atomic, Inc., Cambridge 38, Mass., 1957.
51. Foster, N. B., D. T. Volz and L. W. Foskett, "A Spectral Hygrometer for Measuring Total Precipitable Water," Humidity and Moisture, Vol. I, (A. Wexler, Editor), Reinhold Publishing Corp., New York, 1965.
52. Kondrat'ev, K. YA., I. YA. Badinov, S. V. Ashcheulov, and S. D. Andreev, "Equipment for the Study of Infrared Absorption and Heat Radiation Spectra of the Atmosphere," Izvestia, Atmospheric and Oceanic Physics Series, 1(2), pp. 175-192, 1965.
53. Johnson, J. C., Physical Meteorology, John Wiley and Sons, Inc., New York, 1954.
54. Gates, D. M., "Near Infrared Atmospheric Transmission to Solar Radiation," J. Opt. Soc. Amer., 50(12), pp. 1299-1304, Dec 1960.
55. Deirmendjian, D., "Complete Microwave Scattering and Extinction Properties of Polydispersed Cloud and Rain Elements," Report No. R-422-PR, The Rand Corp., Santa Monica, Calif., Dec 1963.

56. Goldstein, H., "Attenuation by Condensed Water," Propagation of Short Radio Waves, Vol. 13, (D. E. Kerr, Editor), McGraw-Hill Book Co., Inc., New York, 1951.
57. Wheelon, A. D., "Relation of Radio Measurements to the Spectrum of Tropospheric Dielectric Fluctuations," J. App. Phys., 28(6), pp. 684-693, June 1957.
58. Edlen, B., "The Dispersion of Standard Air," J. Opt. Soc. Amer., 43(5), pp. 339-344, May 1953.
59. Reiger, S. H., "Atmospheric Turbulence and the Scintillation of Starlight," Report No. R-406-PR, The Rand Corp., Santa Monica, Calif., Sept 1962.
60. Lumley, J. L., and H. A. Panofsky, The Structure of Atmospheric Turbulence, Interscience Publishers of John Wiley and Sons, Inc., New York, 1964.
61. Yates, H., "Summary of Discussions on Atmospheric Scintillations," Secretary's Report on Infrared Backgrounds and Atmospheric Physics, (J. N. Howard, Chairman), The Boeing Co., Seattle, Wash., June 1963.
62. Sullivan, J. F., "The Mitre Line-Integral Refractometer," Proceedings of the Second Tropospheric Refraction Effects Technical Review Meeting, Vol. I, TDR No. ESD-TDR-64-103, The Mitre Corp., Bedford, Mass., pp. 1.77-1.89, March 1964.
63. Tank, W. G., "A Long-path Absorption Refractometer," Proceedings of the Third Tropospheric Refraction Effects Meeting, Vol. II, TDR No. ESD-TDR-64-148, The Mitre Corp., Bedford, Mass., January 1966.
64. Kruse, P. W., L. D. McGlauchlin and R. B. McQuistan, Elements of Infrared Technology: Generation, Transmission and Detection, John Wiley and Sons, Inc., New York, 1962.
55. Dicke, R. H., "The Measurement of Thermal Radiation at Microwave Frequencies," Rev. Sci. Instrum., 17(7), pp. 268-275, July 1946.
66. Strom, L. D., "The Theoretical Sensitivity of the Microwave Radiometer," Ph.D. Thesis, Univ. of Texas, Austin, Texas, 1 April 1957.

Appendix I
A LONG-PATH ABSORPTION REFRACTOMETER

by
W. G. Tank
The Boeing Company

Reprinted from Proceedings of the Third Tropospheric Refraction Effects Meeting,
Volume II, ESD-TDR-64-148, January 1966

A LONG-PATH ABSORPTION REFRACTOMETER

W. G. Tank*

INTRODUCTION

Because the earth's atmosphere is generally turbulent, the density and water vapor content of air vary, at every point, with time. This heterogeneity of atmospheric composition implies that the speed of electromagnetic signals through the atmosphere is a function of location. Mathematically, this fact can be expressed as $n = n(x)$, where n denotes the normalized propagation speed, or atmospheric refractive index. The conversion factor from time measurement in systems of space measurement based, as are electromagnetic ranging devices, essentially on the simple expression that distance is the product of speed and time, must therefore be the space-averaged propagation speed,

$$\bar{n} = \frac{1}{L} \int_0^L n(x) dx, \quad (1)$$

where L denotes the propagation path. In determining \bar{n} with standard meteorological instrumentation, one is always limited, physically, to determining $n(x)$ at some finite number of values of x along the path. The integral expression for \bar{n} permits the interpretation that, even though errorless determinations of the index n at each of, say, k sampling points were made, the average index \bar{n} would still be subject to a finite sampling error to the extent that

$$\frac{1}{k} (n_1 + n_2 + \dots + n_k) \neq \frac{1}{L} \int_0^L n(x) dx.$$

*Boeing Company, Seattle, Washington.

The above inequality constitutes the current limit to the accuracy attainable in distance measurement using electromagnetic ranging techniques. This paper proposes a refractive index measuring system under development at Boeing capable of relaxing that limit.

THE INSTRUMENT SYSTEM

Theoretical Background

The refractive index at a point in clear air can be written as the sum of two terms,

$$n = A \sum_{i=1}^N \rho_i + B \rho_w, \quad (2)$$

where the ρ 's refer to the densities or concentrations of the different atmospheric gases. Specifically, ρ_w refers to the water vapor density, ρ_i to the densities of the other constituents (oxygen, nitrogen, argon, etc.). The indicated summation is to proceed over all these latter constituents, thus providing, according to Dalton's Law, a measure of the total dry-air density. Water vapor is by far the most variable constituent of the atmosphere. The dry air components show remarkable constancy in their relative proportions. Hence, knowledge of the air content (i. e. , amount per unit volume) or density of just one of these latter constituents constitutes such knowledge of all the rest.

Accepting Equation (2) and all its implications, the absorption of infrared radiation by different atmospheric gases at selected wavelength bands now provides the basis for an instrument system to determine n as a truly integral function of path length, for the total amount of energy absorbed from a beam propagated through the atmosphere depends only on the amount of the absorbing constituent along the path, and not on its distribution. Hence, monitoring an infrared beam in a water vapor absorption band and in an absorption band of one

of the dry air constituents will provide all the information required to compute refractive indices according to Equation (2), which value, because of the actual physical process of absorption, will then precisely represent the n defined in Equation (1).

System Description

The idea of determining atmospheric composition by measuring atmospheric infrared absorptions is certainly not new, the idea preceding efficient means of implementation by nearly forty years (Fowle^[1]). The concept is simplicity itself, requiring, basically, a continuous spectrum radiation source, a radiation detector, and means for effecting narrow-band, wavelength isolation. The need for a precisely calibrated source can be negated by measuring received energy in two different but adjacent bands of the infrared spectrum, one of which is attenuated by the constituent of interest, the other not. The desired constituent density measurement is then provided by the ratio of the two band energies sensed. In this scheme the former band is considered the sensor, the latter the reference. To determine the atmospheric refractive index in this manner, then, a minimum of three wavelength bands must be monitored — two serving as sensors (one for water vapor, the other for any one of the dry-air gases), the third as the reference.

The Sensing and Reference Bands

The choice as to which three wavelength bands to use is largely arbitrary. The three should, however, be grouped as closely as possible together in order to minimize adverse effects on system accuracy that could be caused by differential scattering effects in a hazy atmosphere (more on this later). Furthermore, to take advantage of the simplicity, reliability, and obtainability offered by lead sulfide cell infrared detectors as system radiation sensors, all wavelengths should be in the region of peak sensitivity of such cells. Accordingly, consider

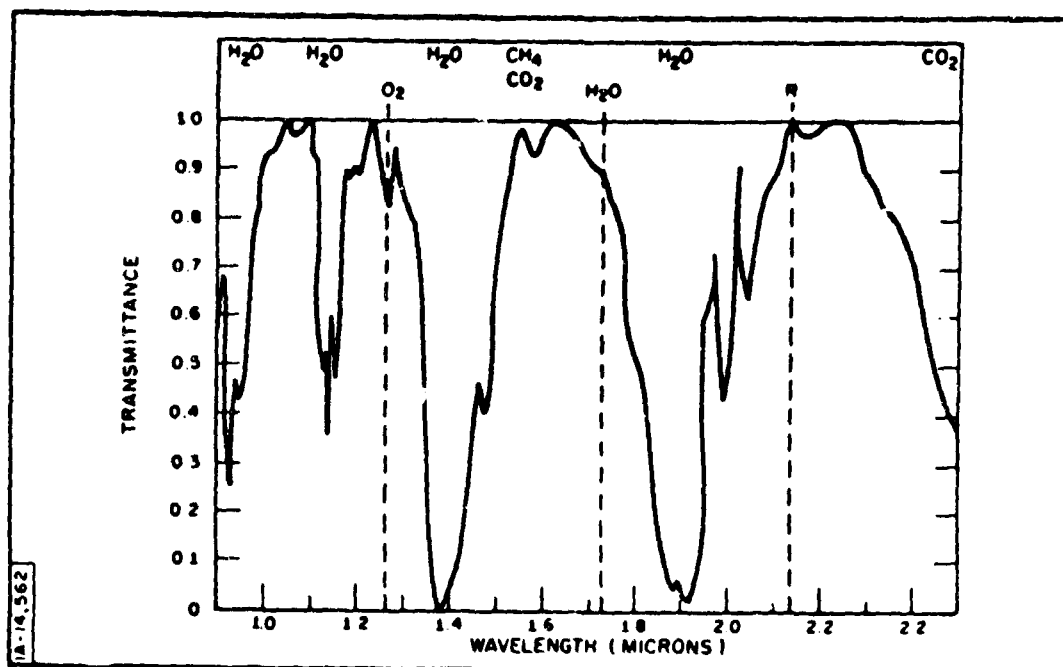


Figure 1. The Near-Infrared Solar Absorption Spectrum (The absorbing atmospheric constituents are identified at the top of the chart above the different absorption bands, the refractometer filter bands by the three dashed abscissas.)

solar absorption spectrum, normalized to peak transmission, presented by Gates^[2] and shown in Figure 1. The abscissa range indicated defines the wavelength region of peak sensitivity of uncooled lead sulfide cells (Kruse, McGlauchlin and McQuistan^[3]).

The spectrum shown in Figure 1 is characterized by four strong water vapor absorption bands, four "window" regions, a weak oxygen and a weak carbon dioxide band. Radiation on any of the window regions could be monitored to supply the reference signal, that in any of the water vapor absorption bands to effect the measurement of water vapor content, and that in the oxygen or the carbon dioxide band to determine the dry-air constituent content.

Three narrow wavelength bands satisfying the requirements of an absorption refractometer are thus specified as indicated, centered at wavelengths of $2.12\ \mu$, $1.73\ \mu$ and $1.256\ \mu$ for the reference, water vapor and oxygen or dry-air density sampling bands, respectively. The water-vapor sampling band is displaced from the center to the wing of the strong $1.86\ \mu$ absorption band for two reasons. First, over any sort of range at all, virtually all the $1.86\ \mu$ radiation would be absorbed from an infrared beam, leaving no signal to effect the desired water vapor measurement. Second, energy in the oxygen band suffers some water vapor absorption by the wing of the $1.37\ \mu$ water vapor absorption band. Water vapor absorption at $1.73\ \mu$ is equal to that in the oxygen band. Hence, by referencing the band energy of the latter to that of the former, unwanted water vapor absorptions at $1.256\ \mu$ can be negated. The $1.73\ \mu$ water vapor sampling band itself is referenced to the window band.

Receiver Optics

An optical system for simultaneously monitoring a beam of infrared radiation at the three wavelengths just specified through a single aperture is shown schematically in Figure 2. A mechanically chopped, collimated beam of energy from a remote, broadband, tungsten filament source of high thermal inertia is directed at the receiver. The Cassegrain collecting optics focus the incoming beam onto a field-stop aperture. The divergent beam then passes through a series of mirror beam splitters, the first of which has a transmission-to-reflection ratio of about 2:1, the second a ratio of 1:1. The beam-splitter series thus serves to split the collected beam into three components, directing approximately one-third of the collected energy onto one of the three indicated narrow bandpass, germanium interference filters. Each arm of the split and filtered beam then impinges on a mixer cone which serves to distribute the filtered energy evenly over the surface of a lead sulfide cell infrared detector.

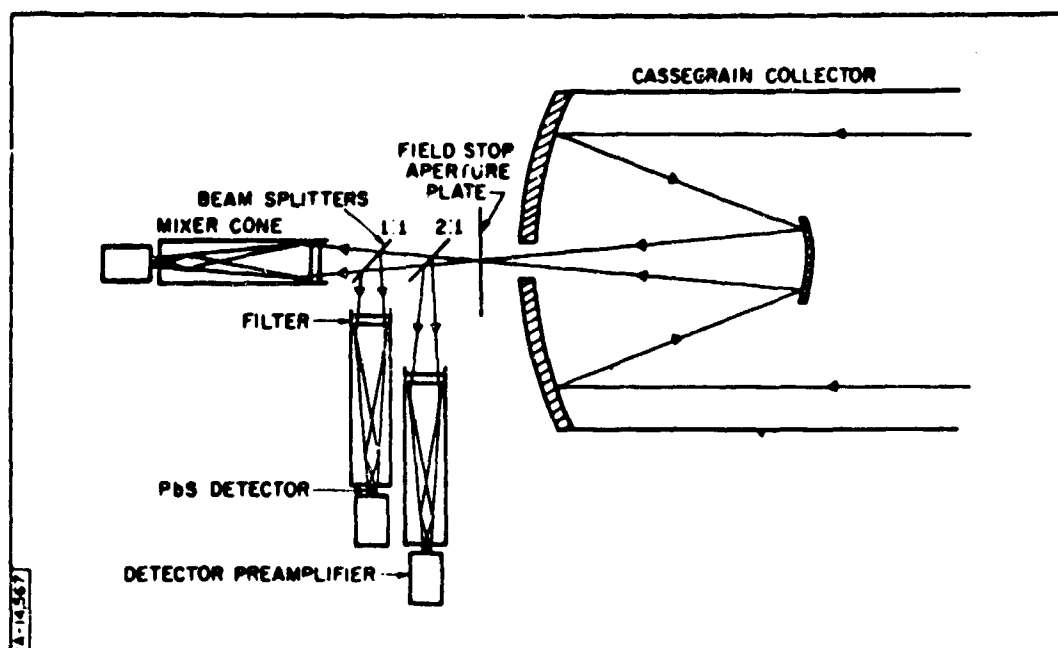


Figure 2. Schematic Diagram of the Refractometer Receiver Bead Optics

This even distribution eliminates shot noise effects that could be caused by inequalities in sensitivity at various spots on the detector surfaces. The interior reflecting surfaces of the mixer cones are gold-plated for the greatest degree of reflection efficiency. Source-to-receiver alignment is accomplished with the aid of 20X spotting telescopes mounted on both the beam and field collimating optics. The entire receiver head is attached to a standard 3-1/2- x 8-inch thread transit head mount for utilization on a standard surveyor's transit tripod.

The Read-out System

The desired comparison between reference and sensing band energies is their ratio, because such a comparison reflects only disproportionate, and not proportionate, energy changes. That is, system response would not re-

reflect a change in the general level of sensed energy caused by the presence of haze or fog in the light beam. The desired ratio is obtained as follows.

Located in the receiver head, directly coupled to the lead sulfide cell detectors, are high input, low output impedance detector preamplifiers (Figure 2). The amplified, essentially alternating-current (as a result of the source chopping) detector signals are then fed into alternating-current, capacitor-coupled (to eliminate the high direct-current cell bias) logarithmic converters. These converters rectify the alternating-current signals and give direct-current outputs proportional to the logarithm of the root mean square value of the input signals. The converter outputs are then combined in a differentiating network to yield a recorded signal proportional to the difference between the logarithms, and hence to the ratio, of the detector input signals. Schematically, the read-out system is shown in Figure 3.

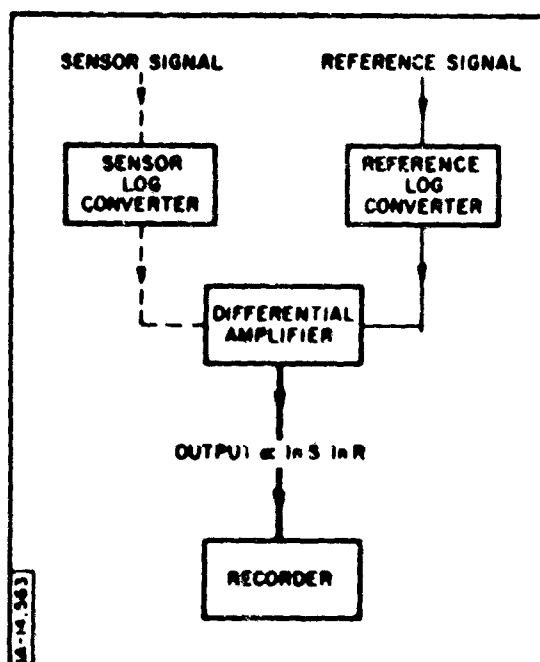


Figure 3. Theoretical Refractometer Readout System

ANTICIPATED OPERATIONAL CHARACTERISTICS

The instrument just described is still in the development stage. But experience with an infrared absorption hygrometer previously developed and applied (Tank and Wergin^[4]), and operating according to the philosophy and methods of the proposed refractometer, permits the following refractometer performance characteristic estimates.

Range Capabilities

An estimate of the range capability of the proposed refractometer boils down, essentially, to the answer to the following question: how far can the source be backed off from the receiver such that the radiant energy collected is still sufficient to generate a signal-to-noise ratio significantly greater than unity? The power received from a remote source emitting a directed beam of energy in the wavelength interval $\Delta\lambda$ is

$$W_{\lambda} = I_{\lambda} \cdot \frac{A^2}{L^2} \cdot \frac{W_1}{W_2} \cdot \frac{\Delta\lambda}{2\pi} \cdot \tau_0 \cdot \tau_A, \quad (3)$$

where

- I_{λ} = intrinsic spectral radiant emittance of the source, watts cm^{-2} micron⁻¹
- A = the area of the collecting optics aperture;
- Δ_{λ} = bandwidth of the wavelength isolation filters, microns
- τ_0 = transmittance of the optics;
- τ_A = transmittance of the atmosphere; and
- L = propagation path length.

The solid angles W_1 and W_2 are defined by the source collimating optics. Specifically, W_1 is the solid angle subtended by the collimating optics aperture at the source, W_2 the solid angle subtended by the source at the aperture. The

four leading terms on the right side of Equation (4) are thus simply system parameters. Both the beam and field collimators used in the refractometer consist of 8-inch aperture, 128-inch (folded) focal length Cassegrainian reflectors. The filter bandwidths are 0.025 micron. For a half-inch source diameter, then, Equation (3) can be written, utilizing the numerical values of the system parameters and taking as a pessimistic estimate of τ_0 a value of 0.05, as

$$W_{\lambda} = \left(1.5 \times 10^{-7}\right) \frac{I_{\lambda}}{L^2} \cdot \tau_A \text{ watts} , \quad (4)$$

where L is expressed in kilometers.

When the source emittance, I_{λ} , is expressed as defined in Equation (3), the power received, W_{λ} , is given in watts. That incident radiation on an uncooled lead sulfide cell which produces a signal-to-noise ratio of unity is, in the wavelength region of interest, of the order 10^{-11} watts (Kruse, McGlauchlin and McQuistan^[3]). Therefore, for workable signals the following inequality must hold:

$$\left(1.5 \times 10^{-7}\right) I_{\lambda} \frac{\tau_A}{L^2} > 10^{-11} \quad (5)$$

The emittance of a $1,400^{\circ}\text{C}$ blackbody (peak emission at about 1.7μ) will be of the order of $10 \text{ watts cm}^{-2} \text{ micron}^{-1}$. Utilizing this value for the source emittance, inequality (6) may be expressed as

$$L < \left(1.2 \times 10^2\right) \tau_A^{1/2} \quad (6)$$

The range at which the refractometer can be worked, then, depends on the atmospheric transmittance. For ranges on the order of tens of kilometers,

the transmittance may (pessimistically) be expected to be on the order of 10^{-2} . This estimate considers both absorption and scattering losses in the propagated beam. Hence, the workable range of the system, too, will be on the order of tens of kilometers.

Expected Calibration

It is expected that the calibration of the refractometer will prove to be quite predictable. Gates^[2] has shown that throughout the spectral region 0.87μ to 2.54μ both the random line (water vapor) and regular line (oxygen) absorption band transmissions vary as the square root of the total amounts of absorbing material in the propagation path according to

$$\ln T = C m^{1/2} \quad (7)$$

In the above Equation (valid for transmissions ranging between 20 and 80 percent), T represents transmittance, C a transmission coefficient, and m the total amount of absorbing constituent. For water vapor, this latter quantity is usually expressed as precipitable centimeters, w , of water and for oxygen as atmo-km, l , of oxygen. The recorded signals from the refractometer may thus be expected to vary linearly with $m^{1/2}$, as past work with the infrared hygrometer indeed verifies (Tank and Wergin^[4]). Over the range of w and l values to be expected, and for propagation paths ranging in length from 5 to 50 kilometers, the l and w calibration curves for the refractometer are as shown in Figure 4. The curves are calculated as dictated by Equation (3) and by the response characteristics of the previously calibrated infrared hygrometer. The dry-air and water vapor densities can be recovered from the measured parameters according to the following relationship:

$$\rho_d = 6.16 \left(\frac{1}{l} \right) \left(\frac{K_g}{m^3} \right), \quad \text{and} \quad (8)$$

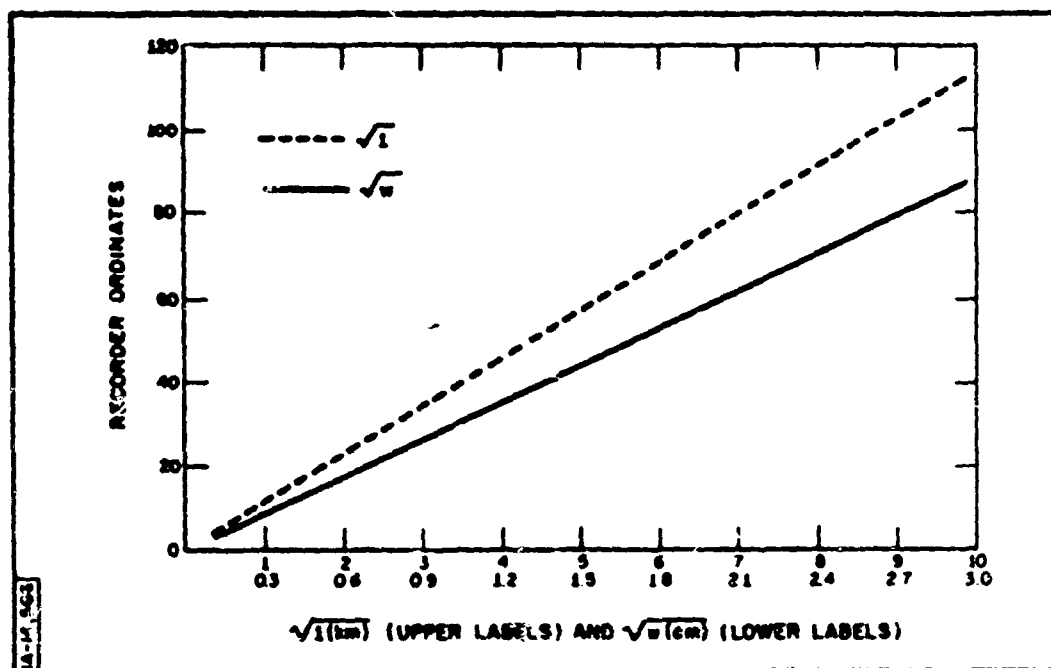


Figure 4. Theoretical Refractometer Calibration Curves

$$\rho_w = 10.0 \left(\frac{w}{L} \right) \left(\frac{2.25}{m^3} \right), \quad (9)$$

where ρ_d and ρ_w denote the dry-air and water vapor densities, respectively, in the units shown. When both L and w are given in kilometers and centimeters, respectively, the propagation path length, L , must be given in kilometers.

Expected Accuracy

In estimating the accuracy of dry-air and water vapor measurement achievable with the refractometer, the following factors must be considered: electronic noise effects, ambient temperature and pressure effects on absorption, differential scattering attenuation effects, and the variability of atmospheric carbon dioxide content. The manner in which these factors act

to limit system accuracy, and the expected magnitude of the effect, can be presented as follows.

Electronic Noise Level Limits

Amplifier and recorder noise combine to give a system noise level of something less than 10 microvolts. Based on the expected system responsivity as indicated in Figure 4, such a signal level is equivalent to optical depths of oxygen and water vapor of about 10^{-7} kilometers and 10^{-6} centimeters, respectively. For ranges of orders of kilometers, such magnitudes imply electronic noise errors in oxygen and water vapor densities of orders one part per hundred million and one part per billion, respectively. In other words, the effect is negligible.

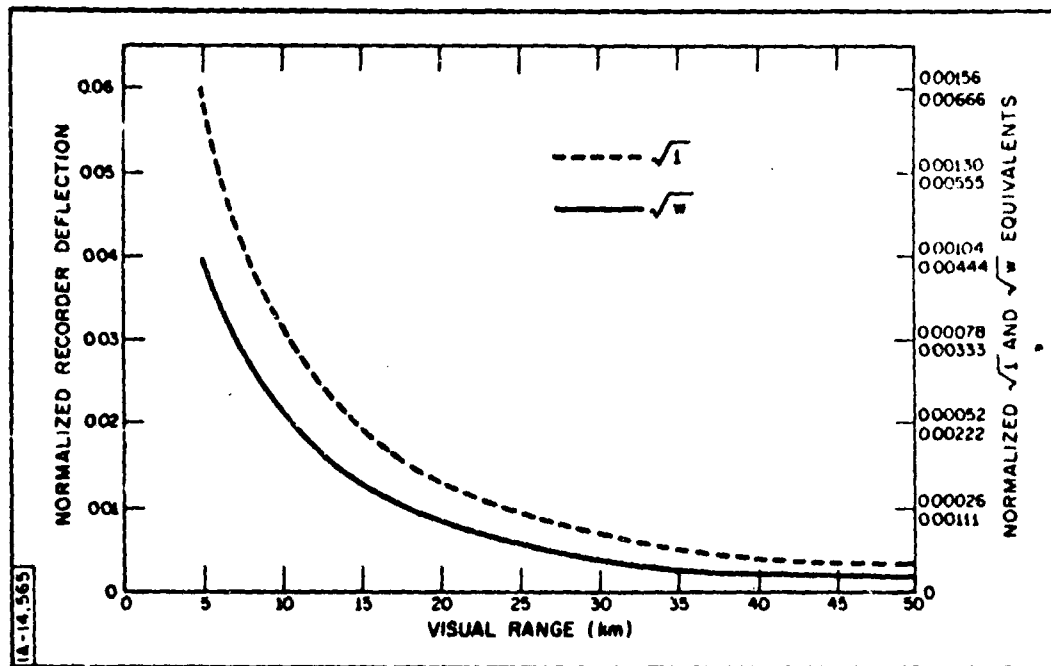
Ambient Temperature and Pressure Effects

The absorption of energy within a certain wavelength band is dependent to some extent on both atmospheric temperature and pressure. Although such effects become appreciable for drastic changes in ambient temperature and pressure, calibration curves established at given pressure-altitudes should remain insensitive to those changes associated with the normal progression of "weather." This statement is substantiated by past work with the infrared hygrometer (Tank and Wergin^[47]).

Differential Scattering Attenuation Effects

Scattering of near infrared energy by atmospheric haze particles is wavelength-dependent. Specifically, the scattering theory predicts that, for given particle size distributions, the shorter the wavelength the more efficient the scatterer. Consequently, the radiation intensity perceived at 1.73μ will be disproportionately less than that perceived at 2.12μ , and that at 1.256μ will be less than that at 1.73μ . Based on data on light transmission through haze

presented by Gibbons,^[5] the magnitude of the effect of the refractometer output signals is as shown in Figure 5. Both sets of ordinate labels are normalized



Ordinate labels are normalized to propagation path length in kilometers. The upper set of right-hand ordinate labels refers to atmo-kms of oxygen; the lower set to precipitable cms of water.

Figure 5. Calculated Error Signals, Caused by Differential Scattering Effects in Atmospheric Haze, as Functions of Visual Range

to the propagation path length, L , in kilometers. The corrections implied are negative corrections, insofar as the equivalent optical depth values express apparent excesses of oxygen and water vapor contents attributable to differential scattering effects. But again the effect is negligible, because for path lengths of the order of 10 kilometers the scattering noise signals are comparable to those associated with electronic noise.

The Variability of Atmospheric CO₂ Content

Dalton's Law relating total pressure to partial pressure can be expressed in terms of density as

$$\rho_T = (\rho_1 + \rho_2 + \dots + \rho_n). \quad (10)$$

That is, total dry-air density can be considered the sum of the individual atmospheric constituent densities. Individual constituent densities can be expressed as

$$\rho_i = M R_i \rho_T, \quad (11)$$

where $M R_i$ denotes the i^{th} constituents mixing ratio, i. e., its percent by weight of the total dry-air mass per unit volume. At this point, the philosophy of the refractometer is that all dry-air constituents exhibit constant mixing ratios. Though generally true for the so-called permanent atmospheric gases (nitrogen, oxygen, argon, plus helium and hydrogen and the noble gases), the atmospheric carbon dioxide content does show considerable variation. This variation is due to a variety of reasons, chief of which are the release of CO₂ to the atmosphere by combustion processes and the exchange via biological processes of CO₂ with soil and vegetation. At any rate, the CO₂ mixing ratio is more properly expressed as

$$M R_{CO_2} = \overline{M R}_{CO_2} + \Delta M R_{CO_2}, \quad (12)$$

where the overbar denotes a constant "average" mixing ratio and the Δ a variable component brought about by the processes must mentioned.

Utilizing Equations (11) and (12) in accordance with Equation (10), then

$$\rho_T = \rho_T \sum_{i=1}^m M R_i + \Delta M R_{CO_2} \rho_T. \quad (13)$$

The summation in Equation (12) is equal to unity, and the remaining term on the right side is thus interpreted as an error in the inferred density, as measured by the refractometer, ascribable to a variable atmospheric CO_2 content. The variation in CO_2 mixing ratio can attain a value of 600 parts per million. Hence, refractometer measured densities will be correct to this same ratio. This, then, is the fundamental limit to the accuracy of density measurements attainable with the refractometer.

It should be remarked that the above limit does not apply to the water vapor density measurement, insofar as this latter quantity is measured directly. System sensitivity will permit water vapor densities to be determined with accuracies of the order of one part per million.

CONCLUSIONS

The claims made regarding the performance of the infrared absorption refractometer just described remain to be proved, insofar as the first prototype unit is still to be tested in the field. But in light of past experience with an absorption hygrometer, the claim as to the ability through use of the refractometer to measure dry-air and water vapor densities to within six parts per ten thousand and a few parts per million, respectively, is not considered unreasonable. Such accuracies imply that the atmospheric refractive index may be specified to seven significant figures. And what is just as important relative to use of the refractometer in conjunction with electromagnetic ranging devices is that the refractive index so specified will represent a space averaged value determined as a truly integral function of path length.

REFERENCES

1. F. E. Fowle, "The Spectroscopic Determination of Aqueous Vapor," Astrophys. J. 35, 149-162, 1912.
2. D. M. Gates, "Near Infrared Atmospheric Transmission to Solar Radiation," J. Opt. Soc. Am., 50, 1299-1304, 1960.
3. P. W. Kruse, L. D. McGlauchlin and R. B. McQuistan, Elements of Infrared Technology: Generation, Transmission, and Detection, New York, John Wiley and Sons, Inc.,
4. W. G. Tank, and E. J. Wergin, "A Long-Path Infrared Hygrometer," in Humidity and Moisture, Vol. I. A. Wexler, ed., New York, Reinhold Publishing Co., 1964.
5. M. G. Gibbons, "Wavelength Dependence of the Scattering Coefficient for Infrared Radiation in Natural Haze," J. Opt. Soc. Am., 48, 172-176, 1958.

UNCLASSIFIED

Security Classification

| DOCUMENT CONTROL DATA - R&D | | |
|---|---|--|
| (Security classification of title, body of abstract and indexing annotation must be entered when the overall report is classified) | | |
| 1. ORIGINATING ACTIVITY (Corporate author) Boeing Company Seattle Washington | | 2a. REPORT SECURITY CLASSIFICATION Unclassified |
| | | 2b. GROUP NA |
| 3. REPORT TITLE Improved Sampling Techniques | | |
| 4. DESCRIPTIVE NOTES (Type of report and inclusive dates) Final Report | | |
| 5. AUTHOR(S) (Last name, first name, initial) Tank, William G. Palmer, Thomas Y. Kreiss, William T. Rowley, James J. | | |
| 6. REPORT DATE August 1966 | 7a. TOTAL NO. OF PAGES 188 | 7b. NO. OF REFS 66 |
| 8a. CONTRACT OR GRANT NO. AF30(602)-3715 | 8b. ORIGINATOR'S REPORT NUMBER(S) | |
| 8c. PROJECT NO. 5579 | | |
| 8d. OTHER REPORT NO(S) (Any other numbers that may be assigned this report) 557902 | RADC-TR-66-407 | |
| 10. AVAILABILITY/LIMITATION NOTICES This document is subject to special export controls and each transmittal to foreign governments or foreign nationals may be made only with prior approval of RADC(EMLI) GAFB, N.Y. 13440 | | |
| 11. SUPPLEMENTARY NOTES | 12. SPONSORING MILITARY ACTIVITY Space Surveillance & Instru. Branch Rome Air Development Center Griffiss AFB New York 13440 | |
| 13. ABSTRACT Line-integrated refractivity is isolated as the basic atmospheric parameter to be determined for corrections to radar ranging data. A basis for the determination of integrated refractivity from measurements of the absorption of infrared and microwave radiation by atmospheric oxygen and water vapor is then established. Three absorption-measuring systems are next described, and engineering-model design specifications are presented. Each of the specifications offers particular advantages to particular ranging operations. It is estimated that incorporation of such devices into ranging systems will permit real-time measurements of slant-range and elevation angle to accuracies five to ten times those currently achieved. | | |

DD FORM 1473

FORM
1 JAN 64

Unclassified

Security Classification

Unclassified

Security Classification

| KEY WORDS | LINK A | | LINK B | | LINK C | |
|---|--------|----|--------|----|--------|----|
| | ROLE | WT | ROLE | WT | ROLE | WT |
| Tropospheric Refraction Refraction Correction Techniques | | | | | | |

INSTRUCTIONS

1. **ORIGINATING ACTIVITY:** Enter the name and address of the contractor, subcontractor, grantee, Department of Defense activity or other organization (corporate author) issuing the report.
- 2a. **REPORT SECURITY CLASSIFICATION:** Enter the overall security classification of the report. Indicate whether "Restricted Data" is included. Marking is to be in accordance with appropriate security regulations.
- 2b. **GROUP:** Automatic downgrading is specified in DoD Directive 5200.10 and Armed Forces Industrial Manual. Enter the group number. Also, when applicable, show that optional markings have been used for Group 3 and Group 4 as authorized.
3. **REPORT TITLE:** Enter the complete report title in all capital letters. Titles in all cases should be unclassified. If a meaningful title cannot be selected without classification, show title classification in all capitals in parentheses immediately following the title.
4. **DESCRIPTIVE NOTES:** If appropriate, enter the type of report, e.g., interim, progress, summary, annual, or final. Give the inclusive dates when a specific reporting period is covered.
5. **AUTHOR(S):** Enter the name(s) of author(s) as shown on or in the report. Enter last name, first name, middle initial. If military, show rank and branch of service. The name of the principal author is an absolute minimum requirement.
6. **REPORT DATE:** Enter the date of the report as day, month, year, or month, year. If more than one date appears on the report, use date of publication.
- 7a. **TOTAL NUMBER OF PAGES:** The total page count should follow normal pagination procedures, i.e., enter the number of pages containing information.
- 7b. **NUMBER OF REFERENCES:** Enter the total number of references cited in the report.
- 8a. **CONTRACT OR GRANT NUMBER:** If appropriate, enter the applicable number of the contract or grant under which the report was written.
- 8b, 8c, & 8d. **PROJECT NUMBER:** Enter the appropriate military department identification, such as project number, subproject number, system numbers, task number, etc.
- 9a. **ORIGINATOR'S REPORT NUMBER(S):** Enter the official report number by which the document will be identified and controlled by the originating activity. This number must be unique to this report.
- 9b. **OTHER REPORT NUMBER(S):** If the report has been assigned any other report numbers (either by the originator or by the sponsor), also enter this number(s).
10. **AVAILABILITY/LIMITATION NOTICES:** Enter any limitations on further dissemination of the report, other than those

imposed by security classification, using standard statements such as:

- (1) "Qualified requesters may obtain copies of this report from DDC."
- (2) "Foreign announcement and dissemination of this report by DDC is not authorized."
- (3) "U. S. Government agencies may obtain copies of this report directly from DDC. Other qualified DDC users shall request through _____."
- (4) "U. S. military agencies may obtain copies of this report directly from DDC. Other qualified users shall request through _____."
- (5) "All distribution of this report is controlled. Qualified DDC users shall request through _____."

If the report has been furnished to the Office of Technical Services, Department of Commerce, for sale to the public, indicate this fact and enter the price, if known.

11. **SUPPLEMENTARY NOTES:** Use for additional explanatory notes.

12. **SPONSORING MILITARY ACTIVITY:** Enter the name of the departmental project office or laboratory sponsoring (paying for) the research and development. Include address.

13. **ABSTRACT:** Enter an abstract giving a brief and factual summary of the document indicative of the report, even though it may also appear elsewhere in the body of the technical report. If additional space is required, a continuation sheet shall be attached.

It is highly desirable that the abstract of classified reports be unclassified. Each paragraph of the abstract shall end with an indication of the military security classification of the information in the paragraph, represented as (TS), (S), (C), or (U).

There is no limitation on the length of the abstract. However, the suggested length is from 150 to 225 words.

14. **KEY WORDS:** Key words are technically meaningful terms or short phrases that characterize a report and may be used as index entries for cataloging the report. Key words must be selected so that no security classification is required. Identifiers, such as equipment model designation, trade name, military project code name, geographic location, may be used as key words but will be followed by an indication of technical content. The assignment of links, rules, and weights is optional.

Unclassified

Security Classification